Study on Supercapacitor and Third-order Optical Nonlinearity of Graphene-based Materials

KANG Luhao

February 2021

Study on Supercapacitor and Third-order Optical Nonlinearity of Graphene-based Materials

KANG Luhao

Doctoral Program in Materials Science and Engineering

Submitted to the Graduate School of

Pure and Applied Sciences

in Partial Fulfillment of the Requirements

for the Degree of Doctor of Philosophy in

Engineering

at the

University of Tsukuba

Abstract

Graphene, a single sheet honeycomb structure possessing sp^2 hybridizations, has attracted great attention from the global scientific communities since its discovery in 2004 because of its distinctive physicochemical properties. In past decades, graphene-based substances have been investigated enormously and applied across various regions including energy storage, micro-nano, as well as photonic devices, and they have become a well-known star in the world. Regarding the preparation methods of graphene, it could be separated in rough to different categories. One type aims to preparing monolayer/multilayer graphene from graphite flakes, which is defined as top-down methods such as mechanical exfoliated and chemical exfoliated graphene. The other is the method of assembling graphene from small molecular carbon sources, which is called bottom-up methods such as chemical vapor deposition (CVD) along with epitaxial growths from SiC. Among various fabrication methods, the operational procedures in chemical exfoliation are simple, low cost, and easily scalable. Thus, chemical exfoliated graphene has promising applications in supercapacitors, photonic devices, sensors, and membranes, owing to its large specific surface areas, excellent optical properties, chemical stabilities, and electrical conductivities. Amid these applications, energy storage and information technologies are core fundament for the future development of society. Supercapacitors are a crucial energy storage device, while photonic devices are essential components of information technologies. Therefore, we studied supercapacitor and optical properties of graphene-based materials.

For supercapacitors, efficient transport of ions and electrons is essential aiming at enhancing the electrochemical properties. However, aggregations in two-dimensional graphene nanosheets occurred easily in the process of fabrication, which is an obstacle to decrease the flow speed of electrons and ions in the electrode. Thus, we intend to construct a network structure by preparing graphene-based composite materials aiming to increase the effective active areas between electrolyte and electrode materials. For photonic devices, it is extremely important to identify the third-order nonlinear optical property for graphene-based materials over broad wavelength regions as well as their carrier dynamics in a femtosecond. However, the dispersion of third-order nonlinearities of graphene oxide/reduced graphene oxide over that broad wavelength region is still unknown. Therefore, our objective is to evaluate third-order optical nonlinearities for graphene-based materials over a broadband region and femtosecond regime.

Here, in this thesis, we firstly prepared a graphene-based composite material in a facile method. Then we investigated the electrochemical performance for graphene-based composites applied in lithium-ion capacitors as an anode. Secondly, we fabricated two-dimensional thin films by dispersing graphene oxide (GO) or reduced

graphene oxide (rGO) into the polyvinyl alcohol (PVA) matrix. Then we systematically investigated the optical nonlinearities for graphene-based material. Particularly, we experimentally determined the dispersion of third-order nonlinearities for GO and rGO in visible regions (450 – 750 nm), which propels their applications in optoelectronic and nanophotonic devices over broad wavelength region.

Reduced Graphene Oxide Decorated with Crystallized Cobalt Borate Nanoparticles as an Anode in Lithium-ion Capacitors

Lithium-ion capacitors (LICs) are chosen to be good solution aiming at integrating merits of lithium-ion batteries (LIBs) possessing large energy densities along with electric double-layer capacitors (EDLCs) possessing large power densities. One of the challenges faced by LICs is to improve the lithium storage properties of anode material. To address this challenge, rGO compositing with crystallized cobalt borate nanoparticles (Co-B/rGO) were prepared being a negative electrode in LICs using facile in-situ grow method. X-ray diffraction (XRD), X-ray photoelectron spectroscopy (XPS) confirmed these crystallized cobalt borate nanoparticles were successfully introduced to rGO nanosheet structures. Transmission electron microscopy (TEM) revealed that cobalt borate nanoparticles anchored at surfaces in rGO nanosheet uniformly. First of all, that introduction of cobalt borate nanoparticles can alleviate the aggregation of rGO nanosheets. Besides, it also provides more active sites for lithium storage with cobalt borate nanoparticles being introduced to surfaces for rGO nanosheets. Then reversible capacities of Co-B/rGO composites retain 600 mAh g^{-1} after 600 cycling numbers under 1000 mA g^{-1} with a good rate performance (310 mAh g^{-1} under 5000 mA g^{-1}) when it was measured in LIBs half-cell as an anode. Furthermore, the LIC full cell was fabricated based on the Co-B/rGO composite as an anode, which provided steady cycle conditions exhibiting capacitance possession of 75% completing 2000 cycling numbers under 2000 mA g^{-1}, as well as large energy densities in 128.6 Wh kg^{-1} under power densities in 107.5 W kg^{-1}. These results indicate that the Co-B/rGO composite possesses an efficiently mixed conducting structure, which implies prospective applications as anode in LICs.

Experimental dispersion of third-order susceptibility of graphene oxide

To mitigate the damage of wide-spectrum laser beams to photonic devices and human eyes, optical limiting (OL) devices are extremely necessary to be developed. In this case, graphene oxide (GO) has become a promising material for OL devices due to its broadband nonlinear optical response in the visible region. However, until now there is no report about the third-order optical susceptibility $\chi^{(3)}$ dispersion of GO, which is a complex quantity that directly corresponds to nonlinear refraction and absorption and is a crucial parameter for the manipulation and application of its OL properties. In the present work, we successfully fabricated graphene oxide thin film by dispersing it into a PVA matrix. Then this part experimentally obtained

determination in the dispersions for $\chi^{(3)}$ in GO in the visible region (450 - 750 nm) by combining spectroscopic ellipsometry with ultrafast pump-probe spectroscopies in femtosecond regime. Here, we identified that the linear optical response of GO shows a flat dispersion over visible regions. In contrast, its nonlinear optical response exhibits saturable absorption (SA) within short wavelengths and reverse saturable absorption (RSA) at long wavelength. These results propel the application of GO in the broadband OL devices based on RSA behavior. In addition, by controlling the fraction of sp^2 and sp^3 hybridizations, it also provides opportunities to tailor the nonlinear optical properties as well as OL behaviors for GO.

Broadband and Comparative Third-order Nonlinearities in Reduced Graphene Oxide with CVD Graphene

Herein, we successfully fabricated two-dimensional thin film by dispersing reduced graphene oxide into the PVA matrix and experimentally determined the third-order nonlinearity in reduced graphene oxide over visible regions with the spectrum (450 to 750 nm) by the combination of spectroscopic ellipsometry with femtosecond pump-probe spectroscopy. With recent development in optoelectronic and nanophotonic devices, it is highly desirable to investigate materials to efficiently manipulate light at the nanoscale. Therefore, the utilization of chemical vapor deposition (CVD) graphene increases in nanophotonics technologies owing to the high tunability superior to noble metals. However, their scalable application is limited due to high-temperature, high-cost fabrication techniques, and complicated transfer procedures. In this work, reduced graphene oxide is proposed to be prospective nominee being employed in future nanophotonic instruments, with relatively simple and low-cost fabrication techniques. Our results demonstrated that reduced graphene oxide possesses comparable nonlinearity similar to that of CVD graphene. Furthermore, we identified that identical tunability that π conjugation electronic transitions dominates their nonlinear response for reduced graphene oxide as well as CVD graphene. These results demonstrated that reduced graphene oxide is a viable alternative. Besides, the third-order susceptibility of reduced graphene oxide in the visible region reveals their substantial behavior to wavelength and pulse width of light in the nonlinear state, which propels the movement of manipulating light at the nanoscale over broad wavelength.

In summary, Co-B/rGO composite has been proved to exhibit outstanding supercapacitor behaviors when utilized being anode materials for the lithium-ion capacitor. In addition, obtained nonlinear optical properties of graphene-based materials including graphene oxide and reduced graphene oxide were investigated over a visible range of 450 - 750 nm and show a remarkable nonlinear optical response, which propels the movement of manipulating light at the nanoscale over broad wavelength.

Content

Chapter 1

Introduction

1.1 Graphene-based Materials

1.1.1 Historical Background

Carbon, known as a kind of abundant chemical elements in nature, has been playing an extremely pivotal role during the development process in our world [1]. It locates in the group fourteenth in the periodic table, which has the atomic number of six [2, 3]. In the valence state of the carbon atom, four electrons are free to constitute covalent chemical bonding, which makes it nonmetallic and tetravalent [4]. In consequence, carbon can form a vast number of compounds through co-existing with other elements in three hybridizations of sp, $sp^{2,}$ and sp^3 [5]. This feature makes carbon the most diverse element on the earth and designated as the king of elements [6]. It serves as a fundamental composing for the whole existing life comprising the human body and is considered as the basis for life on the earth [7]. As shown in Figure 1-1, there are various allotropes composed of carbon with diverse bonding structures, including graphite, diamond, fullerene, as well as carbon nanotube [8]. These allotropic materials possess distinct structures, as well as different physicochemical features. Graphite known as the most common and stable allotrope of carbon has a layered structure with AB-type stackings or ABC alignment [9]. In graphite, covalent and metallic bonding exists within the layer with atomic arrangement in hexagonal features [10]. Additionally, each layer in graphite is linked weekly through a van der Walls interaction. In contrast to graphite, diamond has a covalent network structure bonded through sp^3 hybridizations, which has the highest hardness with extremely different properties from graphite [11]. The arrangement of carbon atoms in the diamond is extremely rigid. In addition to graphite and diamond, the discovery of spherical fullerene in 1985 has greatly expanded the explorations of allotropes of carbon [12]. Fullerene became the subject of intense research in materials science, electronics, and nanotechnology once

discovered by scientists [13]. Spherical fullerene has various potential applications in chemistry and technological fields, in particular, the superconductivity in low temperature has drawn much attention in recent years [14]. Then one-dimensional carbon nanotubes with only 1-nm diameter were discovered in 1993 [15]. Carbon nanotubes have a wide variety of interesting properties in electrical, thermal, and mechanical aspects [16]. With the rapid development of carbonaceous materials, more and more allotropic materials of carbon appeared in our vision. Their applications were also expanded in a larger scope, such as catalytic, hydrogen storage, field emission devices, energy conversion and storage, photonics, and optoelectronic fields [17-20].

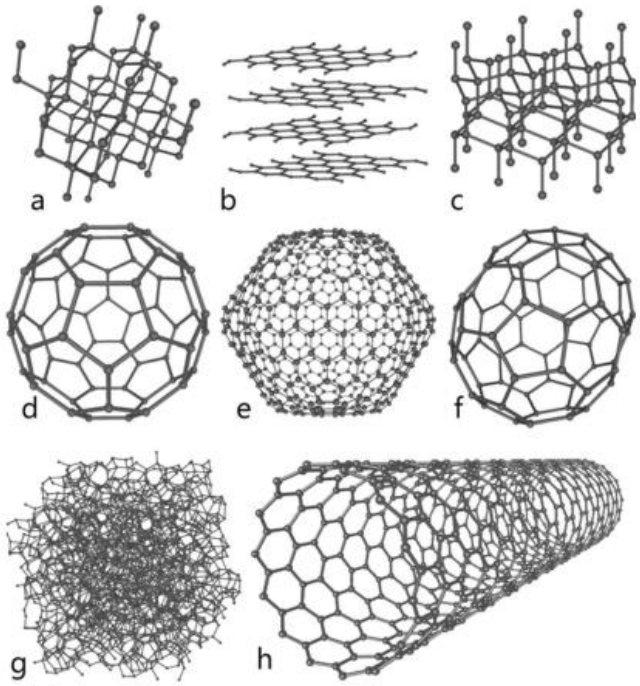

Figure 1-1 Typical allotropic carbonaceous materials: (a) diamonds, (b) graphite, (c) lonsdaleite, (d - f) fullerene, (g) amorphous carbons, (h) carbon nanotubes [21].

With the discovery of carbon nanotube in one-dimension and fullerene in zero-dimension, a single sheet named graphene in two-dimension composed of sp^2 carbon hybridizations appeared on the scientific horizon again [22]. In fact, graphene has been an extensive interest of many theoretical studies as early as in the 1940s [23]. In the next decades, many efforts have been devoted to synthesizing graphene through different kinds of methods. In 1975, B. Lang investigated the formation and texture of the graphitic layer through depositing carbon onto various platinum crystal surfaces [24]. In 1998, graphite multilayers of good crystalline quality were obtained through epitaxial growth on the top of silicon carbide at a high temperature [25]. Until 2004, monolayer graphene was firstly experimentally isolated through mechanical exfoliation by Geim and

Novoselov at Manchester University, using graphite as raw materials [26, 27]. They were resultantly awarded the Nobel Prize for physics because of their great achievement in the highlighted graphene with two-dimension. This Nobel Prize-level discovery immediately showed attractive features for the academic researchers and became a focus in the field of nanotechnology. In the past decades, graphene has truly captured the imagination of scientists and resulted in wide applications in various fields of energy storage devices, transparent conductive electrodes, micro-nano devices, composite materials, optoelectronic and nanophotonic devices [28-30]. Graphene has become a well-known star in the world unquestionably. The reason why it has attracted so much attention is mainly that graphene possesses many unique and exclusive properties, which are endowed by the special single atomic layer structure.

1.1.1 Structural Characteristics of Graphene

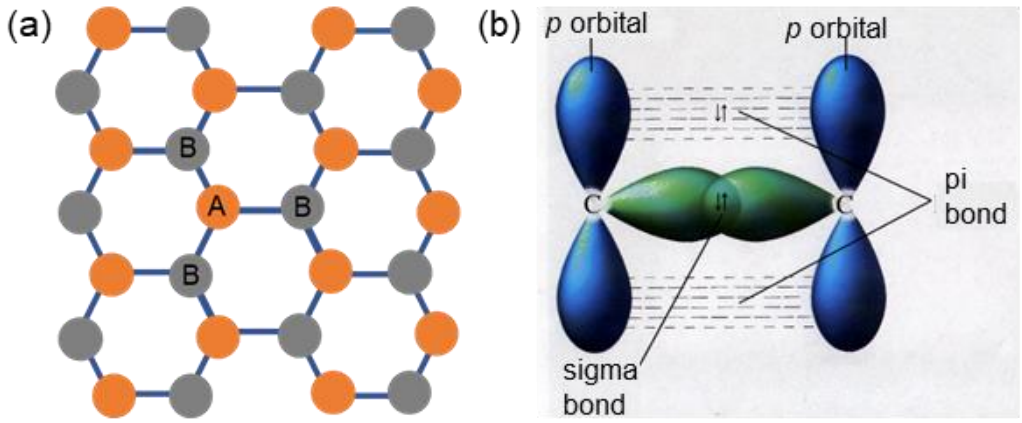

Figure 1-2 (a) Triangular sublattices schematic of graphene. (b) The σ bond, π bond constituted by sp^2 hybridizations [31].

As for crystal structures in graphene, a two-dimensional sheet was constructed with honeycomb structures through each carbon atom bonding with other neighboring atoms covalently [32-34]. There is a hexagonal lattice in the two-dimensional sheet of graphene that presented in Figure 1-2(a). Because four valence electrons in carbon atoms have the orbital configuration of $2s^22p^2$. In the formation process of chemical bonding in graphene, three sp^2 hybrid orbitals were formed with a combination of three valent electrons in orbitals s, p_x, and p_y, respectively [35]. Then each carbon atom covalently connects with three neighbors through a σ bond with a lattice parameter of 1.42 Å as shown in Figure 1-2(b). In addition, the π bond was constructed along the vertical direction to the basic plane by the remaining out-shell valent electron occupying a p_z orbital. Two bands were formed through hybridizing together of these orbitals in partially filled situation with free electrons. The

majority of excellent electronic characterizations in graphene could be explained by the structure of bonging π and anti-bonding π* [36].

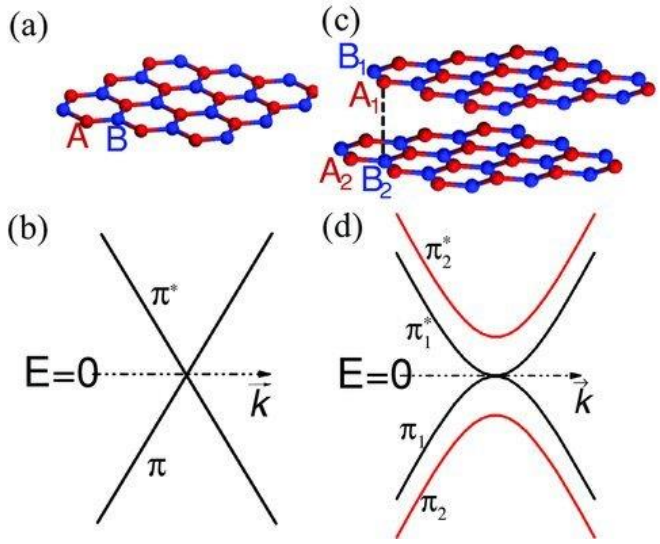

Figure 1-3 Crystal lattice of (a) graphene in one layer, and (b) graphene in multilayers with AB-type stacking. (c) The linear dispersive electronic band structure for graphene in one layer. (d) Parabolic electronic bands for graphene in multilayers [37].

Because of the special crystal configuration, graphene possesses unique electronic band structures. It can be seen from Figure 1-3(a), A and B can be regarded as equivalent positions in unit structures for graphene. As a result, π along with π* orbitals have a cross point at Dirac point in the case of nearest-neighbor hopping only [38]. Thus, the electronic band structure at the Dirac energy E_D shows a linear dispersion characteristic as shown in Figure 1-3(b) [39]. It was known that the carrier with negligible mass in quantization has been observed for graphene nanosheet, which brings on a high Fermi velocity of 10^6 m/s [40]. Consequently, graphene exhibits remarkable electrical transport performance due to this extremely high mobility [41]. In addition, the stacking structure of graphene also influences its electronic behavior. Taking the bilayer graphene with AB-type stackings as an example, the atomic positions in the component structure were named as A_1, B_1, A_2, B_2, respectively as presented in Figure 1-3(c). The interlayer coupling effect results in different electronic features for bilayer graphene which was presented in Figure 1-3(d) [42].

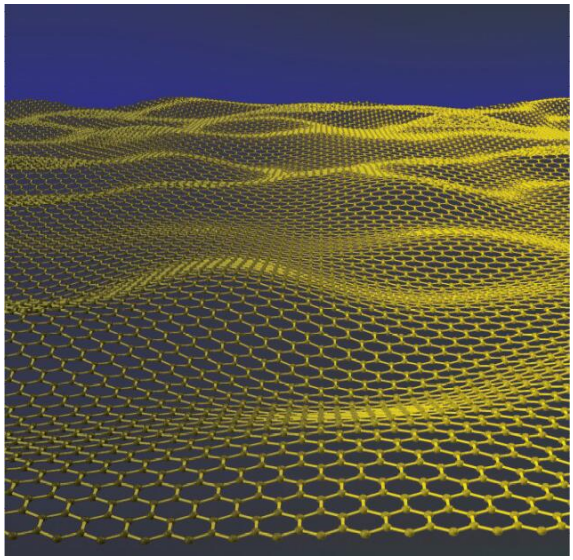

Figure 1-4 Sectional image of graphene nanosheet with ripples in the structure [43].

In the geometrical structure of graphene, the two-dimensional nanosheet could be the basic building block for many other carbonaceous allotropes, for instance, graphite in three-dimension, carbon nanotube in one-dimension, as well as fullerene in zero-dimension [44]. Thus, the experimental isolation of graphene has greatly enriched the system of carbonaceous materials. In the end, a carbonaceous family was systematically constructed with different dimensionalities. In practice, the sheet structure of graphene has many ripples with an amplitude of several nanometers rather than a perfectly flat plane as shown in Figure 1-4. These ripples could be explained as the motion of carbons away from the nanosheet to balance thermal fluctuations in the graphene [45]. These ripples were also demonstrated to have an influence on the electronic performance for graphene [46]. In addition, structural defects may be introduced into graphene in the fabrication process such as point and line defects [47]. And these defects have powerful effects to the charge distribution as well as band structure in graphene [48]. Beneficial from the above unique crystal, electronic and geometrical structures, graphene exhibits outstanding properties in many aspects.

1.1.2 Fundamental Properties of Graphene

Graphene has caused such a sensation in the scientific community since its discovery, mainly due to its distinct properties from bulk materials. These properties make graphene play an important role in basic research and provide perspective application values in many fields. First of all, single-layer graphene is regarded as the thinnest material in nature with a thickness of only 0.35 nm [49]. However, graphene possesses a very high mechanical strength due to the stable structure of sp^2 bonding in the hexagonal lattice. The intrinsic

breaking strength of graphene was evaluated with a value around 40 N m^{-1} by using atomic force microscopy (AFM) [50]. Secondly, graphene was investigated by theoretical studies to have an excellent thermal characteristic [51]. Its thermal conductivity was later experimentally determined to be over 3000 W/mK in a large-area suspended layer [52]. Besides, the specific surface area of monolayer graphene has been calculated theoretically with a value of 2630 m^2 g^{-1}. This value is obviously much higher substantially compared with graphite, commercial activated carbon (AC), as well as carbon nanotube (CNT) [53]. The specific surface area of graphene oxide was reported to vary from 2 to 1000 m^2 g^{-1}, which has relationship with the amount of oxygen functional groups in the basal plane [54]. Graphene was also demonstrated in previous research to have distinctive flexibility due to its unique atomic structure [55]. Furthermore, graphene possesses remarkable electrical conductivities along with chemical stabilities. These features make graphene widely used as substrates in network structure which can enhance the electrochemical properties of composite material [56].

In addition, graphene possesses high optical conductivity as shown in Figure 1-5 [57]. It is established that graphene exhibits a linear dispersion bandgap characteristic in the neighboring position of the K, K' points [58, 59]. Owing to its linear band dispersion, graphene with one layer exhibits a linear optical absorbance of approximately 2.3% constantly over the visible spectrum [60]. Hence, graphene is regarded as one of kinds prospective optical materials. Moreover, the nonlinear optical properties of graphene are another fascinating point, stem from its large effective absorption coefficient and relatively strong light-matter interactions [61, 62]. These nonlinear optical responses and corresponding applications enabled important prospects in passive mode-locking, pulse compression, and ultrafast all-optical switches. In the end, as a consequence of distinct electronic features as well as excellent optical characteristics, graphene benefit greatly to the development of electrochemical, optoelectronic, and photonic devices.

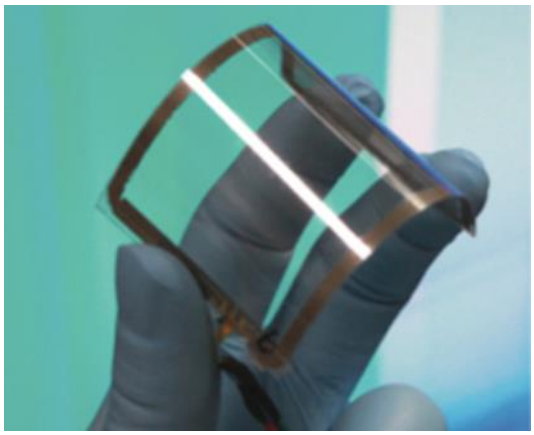

Figure 1-5 Optical transparency in graphene film.

1.2 The Categories of Graphene

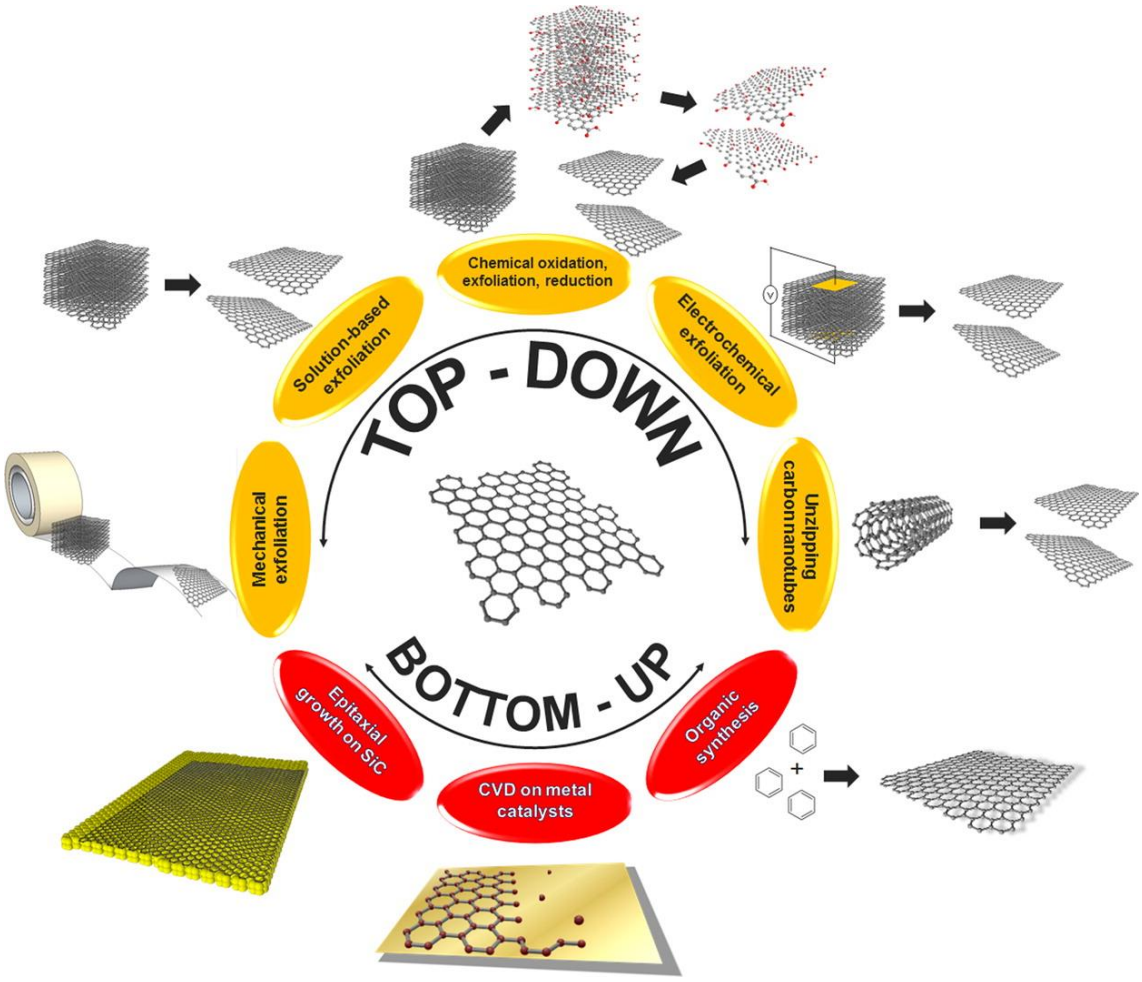

Figure 1-6 Illustrating images of various fabrication techniques for graphene-based materials [63].

Graphene could be viewed in different categories according to the different fabrication methods that were used to prepare graphene. Regarding the preparation methods of graphene, it has been roughly assigned into two categories which can be shown in Figure 1-6. One type is to prepare single-layer or few-layer graphene from graphite flakes, which is defined as the top-down method [64]. Such as graphene made by mechanical exfoliation from graphite as well as chemically exfoliated graphene from graphite. The other is the method of assembling graphene from small molecular carbon sources, which is called the bottom-up method, such as chemical vapor deposition (CVD) along with epitaxial growth on silicon carbide (SiC) [65]. Graphene fabricated through various methods possess different performances in structures, morphologies, and properties.

1.2.1 Chemical Vapor Deposition Graphene

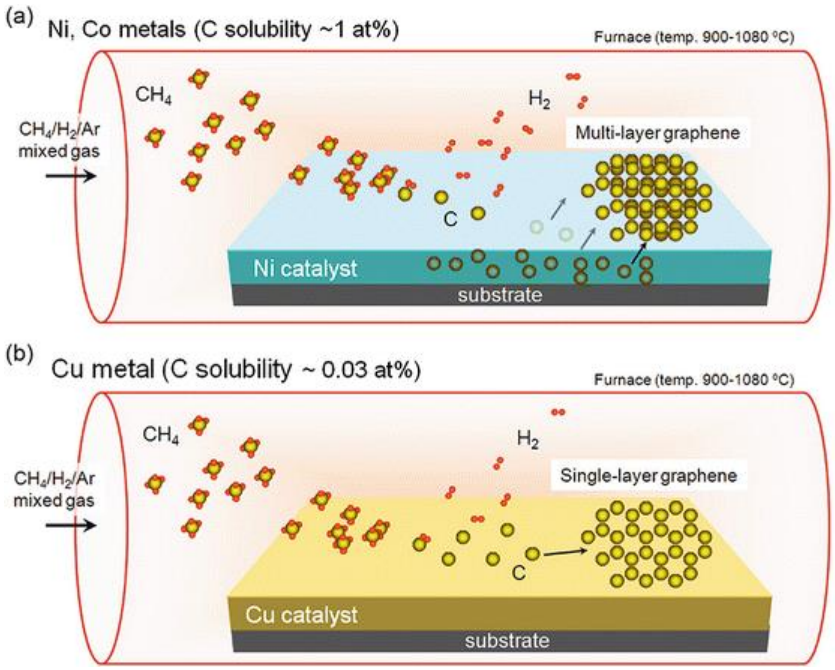

Figure 1-7 Illustrating images for CVD growth in single-crystalline graphene [66].

In the fabricating process of chemical vapor deposition (CVD), two or more gaseous raw materials are introduced into a reaction chamber under a certain temperature and pressure to undergo a chemical reaction to form a new material depositing on the substrate [67]. CVD method is currently regarded as an effective method for synthesizing high-quality graphene [68]. Polycrystalline nickel film was utilized as a substrate to investigate the preparation of graphene sheet through the CVD method in the previous report [69]. Several groups have reported using methane and hydrogen as raw materials to grow high-quality graphene on nickel substrate presented in Figure 1-7. Usually, the growth procedure of graphene in CVD methods involves a high-temperature decomposition step of a carbon source on the substrate [70]. Besides, the transfer process of graphene away from the substrate is complicated and will cause some damages to the quality of graphene [71].

1.2.2 SiC Epitaxial-growth Graphene

The epitaxial growth method is another typical bottom-up method, where silicon carbide (SiC) is usually used as the raw materials to fabricate graphene [72]. The specific principle of epitaxial growth method is that silicon atoms are evaporated and removed in silicon carbide through processing by ultra-high temperature along with extremely vacuum conditions [73]. Consequently, graphene can be obtained after the rearrangement

of remaining carbon atoms on the substrate. With the enhancement for epitaxial growth methods during past years, the control of layer numbers for graphene can be achieved through using different specific parameters [74]. However, the shortcomings of epitaxial growth method are still prominent, such as high cost, harsh reaction conditions with ultra-high vacuum, and difficult procedures to transfer graphene from the substrate.

1.2.3 Mechanically Exfoliated Graphene

The mechanical exfoliation method refers to a method of separating graphene from graphite flakes by mechanical external force [75]. In 2004, Geim et al. fixed the highly oriented cracked graphite on the silicon wafer by the tape peeling method, and then repeatedly posted and peeled it with tape, monolayer graphene was obtained in the end [76]. Despite the graphene crystal structure fabricated through mechanical exfoliation exhibits a very high quality. However, mechanical exfoliation takes a long time, and the yield is very low. In addition, the obtained size of graphene is also extremely difficult to control. Thus, the mechanical exfoliation method is only suitable for laboratory research and cannot be produced on a massive scale.

1.2.4 Chemically Exfoliated Graphene

In the chemical exfoliation method, graphite flakes are usually used as a raw material to prepare graphene [77]. To be specific, the graphite flakes are firstly oxidized with an oxidant agent to introduce oxygen-containing groups to the planar structure of graphite flakes as shown in Figure 1-8. These oxygen-containing functional groups can increase the interlayer distance between atomic layers in graphite flakes. Meanwhile it can also endow it have a certain amount of hydrophilicity, which produced graphite oxide [78]. Then these graphite oxide layers were peeled off in the aqueous or organic solution by an external force to form graphene oxide. Graphene oxide has a nanosheet structure like graphene with one layer or multi-layers. Finally, graphene is obtained via chemically reducing graphene oxide. The remove of many oxygen-containing groups of graphene oxide was achieved after reducing, and the covalent bond structure is restored to a certain extent. The existence of small amount of oxygen functional groups still remain in reduced graphene oxide and certain defects in their conjugated structure. The operational procedures in the chemical exfoliation method are simple, low cost, and easily scalable. Therefore, chemical exfoliated graphene has many advantages to be applied in composite materials, electrochemical and photonic devices. In addition to these advantages, graphene oxide as the precursor material in the fabrication process of graphene also has unique physicochemical properties because of the heterogeneous nanosheet structures in two-dimension and special functional groups in the basal

plane [80].

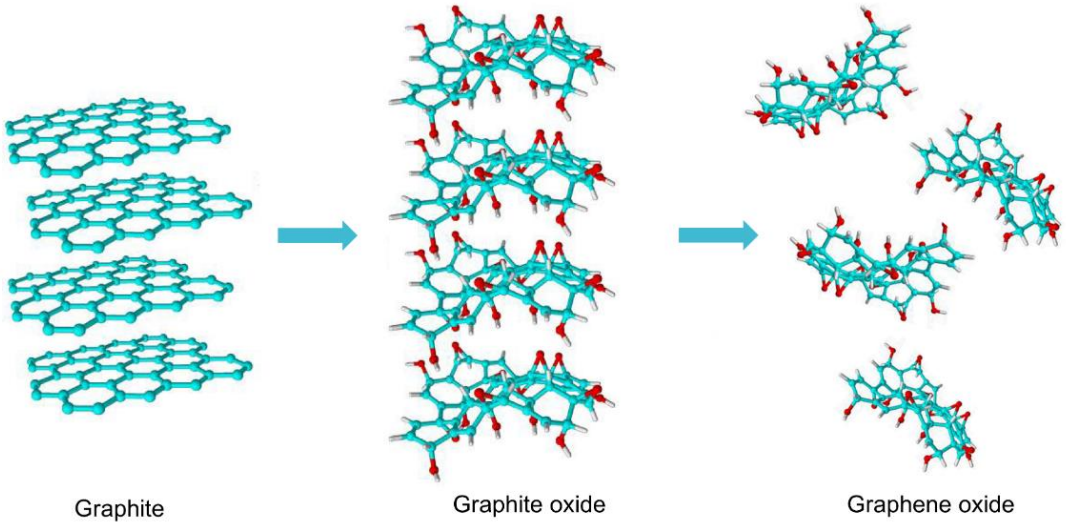

Figure 1-8 Illustration of chemical exfoliation method to prepare graphene [79].

1.3 Applications of Graphene-based Materials

1.3.1 General Background

Energy storage and information communication are two essential aspects of the development of our modern society. It is now necessary that economical, efficient, as well as environment friendly energy storage devices could be developed, aiming at fulfilling the necessities of the increasing important ecologic environment concerning. Supercapacitors have been regarded as a kind of the efficient energy storage instruments, which has a unique energy storage mechanism with simple charge-layers which formed at interface between electrode materials and electrolyte. Therefore, supercapacitor could be utilized to keep and release electrochemical energies at a relatively high rate compared with lithium-ion batteries. Graphene-based materials are regarded as promising conducting material to play important roles in electronic devices especially supercapacitors because of many advantageous features, including low resistance, large specific surface area, as well as good thermal stabilities. Another fascinating application of graphene-based materials should be mentioned that it could be used as a promising optical candidate material in photonic applications owing to remarkable transparent optical characteristics and strong interaction between light and matter. Photonic devices are ubiquitous in our society with extreme importance. Their existence could be found in every area including

daily life and scientific fields. Light detection, telecommunications, information processing, photonic computing are important foundations to the information communication techniques, which is a core competence for the development of trivial future society. Therefore, it has been a subject of interest to investigate the prospects of graphene-based materials employed as electrode materials for supercapacitors as well as photonic instruments.

1.3.2 Applications in Supercapacitors

In recent years, aiming at fulfilling the requirements for ecological, economical, along with efficient devices to store energy, graphene has been considered to be potential material due to its intriguing properties such as large surface area theoretically, good electrical conductivities. Moreover, chemically exfoliated graphene provides us opportunities to achieve physical and chemical modifications because of existence of the oxygen-containing groups around the edges in graphene nanosheets, which are introduced in chemical oxidation process. Among these various energy storage devices, supercapacitors based on graphene materials have been considered as a prospective choice due to the larger power density compared to lithium-ion battery along with higher energy density compared to dielectric capacitor. Graphene as an electrode material that can be used in supercapacitors, has large importance to enhance the electrochemical performance of these devices. The current electrode materials commercially used in supercapacitor are activated carbon. It has many advantageous features including low cost and large surface area. While the pore structures in activated carbon cannot be utilized effectively in the charge/discharge in supercapacitors. Besides, functionality also has some influence on the electrochemical properties of supercapacitors. Consequently, the electrochemical properties for activated carbon are far from the expectation in the supercapacitors. Therefore, many effortful investigations have been conducted on electrodes in supercapacitors.

It was demonstrated in previous research that capacitance of electrodes has close relationship with the amount of active areas and defects. Thus, graphene should have a high capacitance because it has high specific surface area as much as 2630 $m^2 g^{-1}$ in theory. In comparison, the active area in graphene is much larger than that of other carbonaceous materials that are usually used in supercapacitors. In addition, graphene-based materials possess high electrical conductivity compared with commercial activated carbon. These remarkable advantages endow graphene with its promising electrode materials in supercapacitors. Graphene with various structures could be used as the electrode material in supercapacitors, such as zero-dimensional free-standing graphene with dots or powders, one-dimensional graphene fibers, two-dimensional films, along with three-

dimensional network structures. Stoller and cooperationists prepared chemically modified graphene with one atomic thickness and measured the electrochemical performance in supercapacitor cells [53]. The specific capacitances were demonstrated to be over 100 F g^{-1} when measured in different electrolytes. In addition, their experimental results demonstrated that the graphene-based electrode materials working in supercapacitor cells could exhibit excellent behavior in a wide working voltage range.

Besides, graphene has also been employed to be anode in hybrid capacitors. For single-layer graphene, Dane et al. proposed in 1995 that the combination of lithium ions and graphene can occur on the upper and lower sides of the graphene plane, so its capacity can reach twice that of graphite. Furthermore, proposed that the covalent point of the benzene ring in graphene may also provide a site to react with lithium ions, so the specific capacity can be further improved as 1164 mAh/g. However, these lithium storage models were questioned after graphene was successfully peeled off mechanically. Wu al. reported in the literature with modellings that the solid electrolyte interface (SEI) films will produce part for the irreversible capacities. The edge defects, vacancies, and nano-holes in graphene can also be used as active sites for storing lithium ions. Also, the nano-space between graphene layers can be used to store lithium ions. Compared to graphite, graphene has more structural defects. In addition to higher capacity compared to graphite, there are also many disadvantages: large SEI was formed in the reaction process, which not only consumed the lithium source but also result in low Columbic efficiency in the first cycle. The above shortcomings can be improved through structural control and surface modification in graphene.

1.3.3 Applications in Photonic Devices

Graphene-based material was likewise regarded as prospective choice for photonic devices. It has drawn enormous interest in next-generation communication techniques due to its numerous intriguing optical properties [81]. One of the important reasons is that the optical response in graphene can be effective in a broad wavelength ranges including visible and mid-infrared regions [82]. Besides, the optical absorption has good tunability in that broadband [83]. This could be ascribed to the linear and zero-bandgap electronic band structure. As a result, graphene-based materials can be prospective components to developing broadband saturable absorbers for ultrafast lasers. Goossens S. et al. fabricated an image sensor array using the integration of graphene-based materials, which could work in a broadband region [84]. In addition to the intriguing optical response, graphene has ultrahigh charge carrier mobility with a value of 200,000 cm^2/Vs [85]. This feature renders its auspicious application in modulators and photodetectors. Ultrafast transistor-based photodetectors

were prepared by using graphene-based materials by Xia and coworkers [86]. These devices were demonstrated to show high bandwidth light detection and a wide working wavelength range. Moreover, photonic devices based on graphene materials could be applied in the biochemical sensors due to their huge adsorption capacity. The utilizations in optical sensing can greatly lower the limit of detection and increase the specificity of label-free biochemical sensing [87]. In consequence, graphene-based materials engage outstanding platforms to develop prospective photonic devices for future information and communication technology [88].

1.4 Principle of Supercapacitors

In general, supercapacitors are constructed with several parts, including electrodes, electrolyte, separator, current collector, and package [89]. Supercapacitors can be categorized into three kinds according to the types of electrode materials and their energy-storage mechanisms [90]. The principles of three types of supercapacitors are going to be introduced detailedly below.

1.4.1 Electric Double-layer Capacitors (EDLCs)

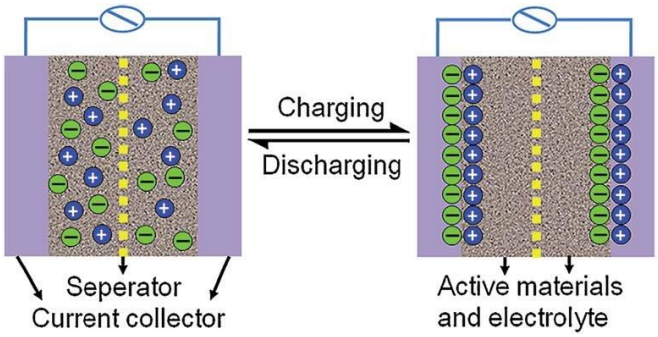

Figure 1-9 Construction diagrams of charging and discharging process in EDLCs [91].

EDLC is a kind of electrochemical capacitor that stores energy through accumulating charge via electric double layers. Corresponding construction diagrams of the charging and discharging process in EDLCs were presented in Figure 1-9. In general, an EDLC device is constructed with two symmetric electrodes, which were isolated by a separator that can prevent a short circuit in the system [92]. Besides, the EDLC cell was filled with an electrolyte. In the charging process of EDLCs, the ions of electrolyte form absorption onto the active materials in the electrode, then electric charges accumulated [93]. As for the discharging process in EDLC, the desorption of ions occurs between electrodes and electrolytes. In this way, EDLCs store and deliver energy within short time and reversible method. Thus, EDLCs have the advantages of high-power density along with

good cycling life. Nevertheless, it suffers from deficient energy density in practical applications. The charge storage mainly comes from the surface area of electrodes. Thus, it is highly desirable for electrode materials in EDLCs to possess suitable pore structure and surface properties. The common utilization of activated carbon is adopted in EDLCs as electrode material currently [94].

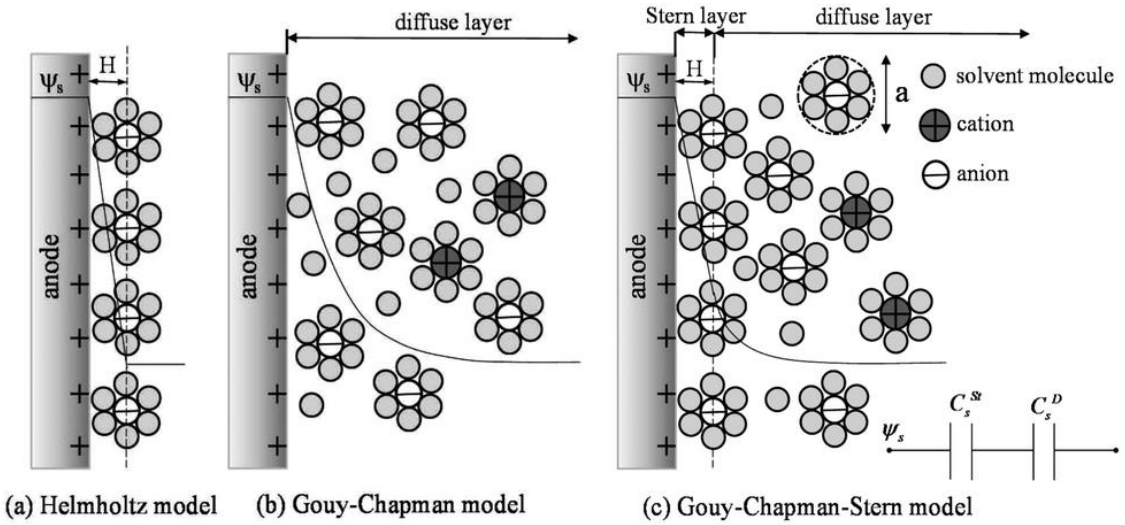

Figure 1-10 Illustrating images of EDLCs structure describing using (a) Helmholtz models, (b) Gouy–Chapman models, as well as (c) Gouy–Chapman–Stern models. H represents distance in charge layers reported in Helmholtz models [98].

The schematic models of a positively charged electrode in EDLC structures were presented in Figure 1-10. The model structure of EDLCs was firstly proposed by Helmholtz shown in Figure 1-10(a). In the interface between electrodes and electrolytes, charges were accumulated with opposite signs in cathode and anode, respectively. This phenomenon can also be observed in conventional dielectric capacitor [95]. In the early period of the 1910s, modifications of Helmholtz models were made by scientists, respectively. They proposed that the ions are mobile in the electrolyte as shown in Figure 1-10(b). In their model, ions were distributed in a region near the electrode surface rather than parallel layers [96]. Until 1924, Gouy–Chapman–Stern models was proposed through efforts of Stern, with a combination of Helmholtz models and Gouy–Chapman models as shown in figure 1-10(c) [97]. In this model, Stern and diffuse layers were formed in the charging process of EDLCs, which has been adopted in academic filed.

Discussing about the electrolyte used in EDLCs, they can be divided into several kinds, such as aqueous solution, organic electrolytes, and ionic liquids [99]. Some advantages could be identified in the aqueous electrolyte solution. The most two important advantages are its intriguing equivalent series resistance with low values along with excellent permittivity [100]. Despite these advantages, the application of aqueous

electrolytes is limited by its low working voltage range of less than 1 V [101]. Consequently, the energy density of EDLCs used aqueous electrolytes is limited significantly by the low operating voltage range. In contrast, the working voltage of EDLCs could be increased to around 2.7 V when electrolytes were used in the organic solvent [102]. In this way, the electrocapacitive performance can be greatly improved. However, acetonitrile (AN) or propylene carbonate (PC) solvents have been adopted widely in most organic electrolytes, which causes large concern on safe status because of the flammable and toxic features. Recently, ionic liquid is regarded to be a promising electrolyte in EDLCs because of its wider working voltage range and relatively low toxicity compared to organic solvents [103]. However, the power density of EDLCs remains a large obstacle in practical applications.

1.4.2 Pseudocapacitors

Distinct from the energy storage mechanism in EDLCs, pseudocapacitors are another type of supercapacitors. In the charging and discharging process of pseudocapacitors, faradic reactions occur between electrode materials and electrolytes [104]. Enormous redox substance has been developed to be electrodes in pseudocapacitors, for instance, metal oxides and conducting polymers [105]. Metal oxides have been applied in pseudocapacitors because of its high conductivity. One of the typical metal oxides used in pseudocapacitors is RuO_2 [106]. Despite RuO_2 pseudocapacitor was demonstrated to exhibit high specific capacitance, it suffers from the high cost in practical applications [107]. Especially, metal oxides, including RuO_2 electrodes have short term stability due to the cracking problems caused in the cycling process [108]. As for conducting polymers, polypyrrole, polyaniline, and polythiophene are widely adopted as the electrode in pseudocapacitors [109]. Conducting polymers show many advantageous properties of flexibility and high conductivities, which are beneficial to improve the capacitance of pseudocapacitors compared to EDLCs [110]. However, the low cycle stability is also a prominent obstacle in their development. Besides, swelling in the volume of polymer electrodes have large side-effects to the behaviors of the capacitor devices [111]. In a word, pseudocapacitors have higher energy density than EDLCs due to redox reactions in the charge transfer process. However, the application of pseudocapacitors is still limited by poor cycling stability and low power density.

1.4.3 Hybrid Capacitors

Hybrid capacitors have been proposed as an innovative type of supercapacitor to deliver large energy density via expanding operating voltage limitation and capacitance of devices [112]. Compared to EDLCs,

different mechanism exists in the electrodes in hybrid capacitors [113]. In general, a hybrid capacitor is combined by batteries-type electrode along with capacitors-type electrode as shown in Figure 1-11. The concept of hybrid capacitors was firstly proposed by Amatucci's group in 2001 [114]. They fabricated the hybrid device through employing AC to be a capacitive electrode, as well as $Li_4Ti_5O_{12}$ as the batteries-type electrode. Nonaqueous electrolyte was utilized in the devices. In the material of cathode, non-faradaic reactions occur on the interface of the AC materials and electrolyte. In the meantime, a reversible faradaic process occurs in the anode materials. Therefore, a large energy density could be obtained in hybrid capacitors due to the large specific capacity from faradaic reactions in a batteries-type electrode. In addition, the rapid charging and discharging rate in capacitor-type electrode guarantee the high-power density as well as cycling stability in hybrid capacitors [115]. Furthermore, the organic electrolyte can provide a larger working voltage range compared to an aqueous system [116]. In the end, hybrid capacitor can be explored to be a good solution and is viewed as a kind of prospective supercapacitors in practical applications.

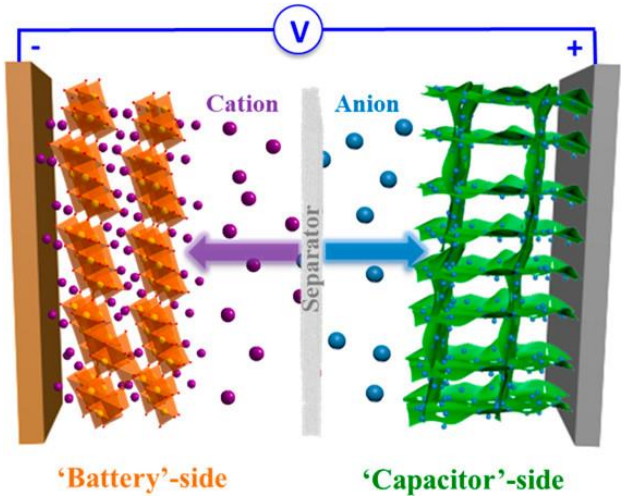

Figure 1-11 Schematic representations of hybrid supercapacitors [117].

One of the main issues needed to be addressed in hybrid capacitors is to balance the kinetics between the anode materials and cathode materials [118]. Because the non-faradic adsorption/desorption proceed much quickly in the cathode materials than the anode materials where the faradaic reactions occur. Recently, a series of hybrid capacitors were investigated on the basis of various electrode materials. Activated carbon have been adopted commonly as cathode material in hybrid capacitors [119]. As for anode, various redox materials have been investigated such as graphite and metal oxides. More recently, graphene emerges as a promising candidate in electrochemical applications because of considerable specific surface area as well as excellent electronic performance. Aphirakaramwong reported a hybrid capacitor device using a composite structure with graphene

and carbon nanotubes [120]. The device was demonstrated to display good electrochemical performance. Similarly, graphene hybrid capacitors were assembled by using graphene aerogel as a negative electrode, which also has a maximum output energy density and a high-power density [121].

1.5 Third-order Nonlinearity

In the past decades, optoelectronic and photonic devices have been playing critical roles in many scientific and technological fields such as industry, agriculture, and medicine. Photonic devices need to study the nonlinear optical properties, which is a crucial point aiming at understanding interactions between intense light and materials [122]. The main research topic of nonlinear optics is the various nonlinear optical phenomena and laws generated by the interaction between laser and medium [123]. The history of nonlinear optics can be traced back to the Pockels effect which was first discovered by German scientists in 1893 [124]. With the development and maturity of laser technologies, nonlinear optics has become an independent and important subject in academic fields. In the past few decades, many kinds of nanomaterials were demonstrated exhibiting excellent optical nonlinearities. Consequently, a large number of nanophotonic devices were designed and fabricated based on materials with optical nonlinearities. In this case, graphene-based substance has produced much interesting exploration in nonlinear optical research.

1.5.1 Background of Third-order Nonlinearity

Electrical polarization was generated on the condition that the materials were applied in the electromagnetic field of laser beams. Therefore, the polarization effect could be utilized in the description of nonlinear optical response in materials. Here, the relationship between the microscopic polarization intensity P that induced in the bulk media and the external electric field E obeys the expression in following equation 1-1,

$$P = \varepsilon_0\left[1 + \chi^{(1)} + \chi^{(2)}E + \chi^{(3)}E^2 + \cdots\right]E \qquad (1\text{-}1)$$

in which ε_0 represents the permittivity of vacuum, $\chi^{(1)}$, $\chi^{(2)}$, $\chi^{(3)}$ represent linear, second-order, and third-order susceptibilities [125]. In isotropic substances, even-orders susceptibilities vanish due to the centrosymmetric properties in the atomic arrangement, such as graphene-based materials [126]. Because the massless Dirac fermions in graphene-based materials constitute a centrosymmetric medium for in-plane excitations, their second-order nonlinear optical response is thus negligible if the effects of spatial dispersion

are not considered. Therefore, third-order nonlinearity is the most important parameter to describe the optical nonlinearities for graphene-based material.

1.5.2 Characterizations of Third-order Nonlinearity

Z-scan is one of the common techniques currently to measure the nonlinear optical properties [127]. It has advantages including simple operation using a single beam and powerful functionalities. The nonlinear absorption, scattering, as well as refraction can be characterized by using Z-scan measurement [128]. The schematic diagram of the Z-scan technique was presented in Figure 1-12. To be specific, a convex lens was employed to focus laser beams. In consequence, an intensity-spatially-varied optical field was established. The transmission of targeted materials could be recorded by using an aperture. In the measurement, the information of transmission changes could be evaluated with the sample position changes around the focal point between negative z and positive z. In the end, the parameters in nonlinear state of materials could be evaluated through open and closed apertures in Z-scan measurement. However, the evaluation was often conducted in single or discrete wavelengths. Therefore, the nonlinear optical properties of materials cannot be characterized at continuous wavelength by using Z-scan measurement.

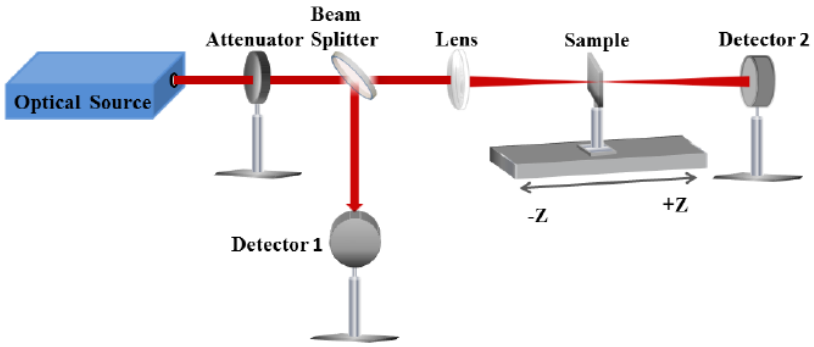

Figure 1-12 Schematic of the Z-scan experimental setup [129].

1.5.3 Applications of Third-order Nonlinearity

With continuous research, nonlinear optics has gradually entered the stage of practical applications from theoretical research. Materials with nonlinear optical properties could be used in optoelectronic and photonic fields such as communication technology and laser techniques. For example, materials with nonlinear saturable absorption effects could be used to applied in passive mode-locking due to saturable absorption and passive Q-switching of laser pulses [130]. Materials with nonlinear reverse saturable absorption effects can be used as

optical limiting materials for laser protection devices [131]. Note that materials with reverse saturable absorption effects are of very high sensitiveness responding to intensities and wavelengths. The transmission rate is high when intensities of incident light is weak. In this case, most of the light can pass through the materials, which guarantees the bright enough in the field of view. At the same wavelength, the transmission decreases at the condition of the strong incident light, which could decrease the intensity of light reaching the photoelectric sensors, other precision instruments, and the human eyes. As a result, the damages induced by intense laser could be avoided.

1.6 Motivation and Objective

Graphene-based materials are endowed full of attention in supercapacitors and photonic applications due to their unique two-dimensional structure, superior physicochemical properties specially such as remarkable electrical conductivities, optical transparent features, as well as nonlinear optical characteristics. As for supercapacitors, graphene especially chemically exfoliated graphene has been demonstrated to be promising electrode materials in hybrid capacitor. The specific capacities of graphene electrode are much larger than commercial activated carbon. However, aggregations of the two-dimensional graphene nanosheets occur easily in the process of fabrication, which is an obstacle to decrease the flow speed of electrons and ions in the electrode. The effective surface area, electron, and ion transport decrease sharply as the consequence of the aggregation of graphene nanosheets. Therefore, we intend to construct a network structure by preparing graphene-based composite materials aiming to increase the effective active areas between electrolyte and electrode materials.

As for the applications in photonic devices, it is important to identify the third-order optical nonlinearities for graphene-based materials, which is an essential parameter aiming at understanding the interactions between intense light and matters. In spite of many efforts to study the nonlinearities of graphene-based materials during the past decades, a lot more still remains that is necessary to be identified for graphene oxide as well as reduced graphene oxide. Furthermore, their corresponding third-order nonlinearities have been investigated at a single wavelength only. However, experimental evaluation of the dispersion of third-order nonlinearity of graphene-based materials over a broad wavelength range is necessary to comprehend the manipulation of light in a nanoscale. Based on the above motivations, this thesis mainly focuses on two aspects. Firstly, we intend to get the preparation of graphene-based composites and fabricate supercapacitors using them as an electrode, which aims to improve the performance of electrochemical capacities. Secondly, this thesis will investigate the third-order nonlinearities of graphene-based materials including GO as well as rGO, which aims to understand the

interaction between intense light and matters. To end, studies on the supercapacitor and third-order nonlinearities of graphene-based materials will propel its prospective application along with the development for energy storage systems and photonic devices in the future.

References

[1] T. Henning, F. Salama, Carbon in the universe, Science, 282 (1998) 2204-2210.

[2] G. Frenking, R. Tonner, S. Klein, N. Takagi, T. Shimizu, A. Krapp, K.K. Pandey, P. Parameswaran, New bonding modes of carbon and heavier group 14 atoms Si-Pb, Chem Soc Rev, 43 (2014) 5106-5139.

[3] A. Mujica, C.J. Pickard, R.J. Needs, Low-energy tetrahedral polymorphs of carbon, silicon, and germanium, Physical Review B, 91 (2015) 214104.

[4] J.C. Ashley, J.J. Cowan, R.H. Ritchie, V.E. Anderson, J. Hoelzl, Straggling and Plasmon Excitation in the Energy-Loss Spectra of Electrons Transmitted through Carbon, Thin Solid Films, 60 (1979) 361-370.

[5] J.F. Yu, H.P. Feng, L. Tang, Y. Pang, G.M. Zeng, Y. Lu, H.R. Dong, J.J. Wang, Y.N. Liu, C.Y. Feng, J.J. Wang, B. Peng, S.J. Ye, Metal-free carbon materials for persulfate-based advanced oxidation process: Microstructure, property and tailoring, Prog Mater Sci, 111 (2020) 100654.

[6] A. Demming, King of the elements?, Nanotechnology, 21 (2010) 300201.

[7] A. Hirsch, The era of carbon allotropes, Nat Mater, 9 (2010) 868-871.

[8] S.K. Tiwari, V. Kumar, A. Huczko, R. Oraon, A. De Adhikari, G.C. Nayak, Magical Allotropes of Carbon: Prospects and Applications, Crit Rev Solid State, 41 (2016) 257-317.

[9] D. Gray, A. McCaughan, B. Mookerji, Crystal structure of graphite, graphene and silicon, Physics for Solid State Applications, 6 (2009).

[10] K. Yoshizawa, T. Kato, T. Yamabe, Interlayer interactions in two-dimensional systems: Second-order effects causing ABAB stacking of layers in graphite, The Journal of Chemical Physics, 105 (1996) 2099-2105.

[11] D.W. Bullett, Chemical pseudopotential approach to covalent bonding. II. Bond lengths and bond energies in diamond, silicon and graphite, Journal of Physics C: Solid State Physics, 8 (1975) 2707-2714.

[12] M. Buhl, A. Hirsch, Spherical aromaticity of fullerenes, Chemical Reviews, 101 (2001) 1153-1183.

[13] A. Belkin, A. Hubler, A. Bezryadin, Self-assembled wiggling nano-structures and the principle of maximum entropy production, Sci Rep, 5 (2015) 8323.

[14] V. Georgakilas, J.A. Perman, J. Tucek, R. Zboril, Broad family of carbon nanoallotropes: classification, chemistry, and applications of fullerenes, carbon dots, nanotubes, graphene, nanodiamonds, and combined superstructures, Chem Rev, 115 (2015) 4744-4822.

[15] S. Iijima, T. Ichihashi, Single-shell carbon nanotubes of 1-nm diameter, Nature, 363 (1993) 603-605.

[16] M.S. Dresselhaus, G. Dresselhaus, J.C. Charlier, E. Hernandez, Electronic, thermal and mechanical properties of carbon nanotubes, Philos Trans A Math Phys Eng Sci, 362 (2004) 2065-2098.

[17] A. Bagreev, T.J. Bandosz, On the mechanism of hydrogen sulfide removal from moist air on catalytic carbonaceous adsorbents, Ind Eng Chem Res, 44 (2005) 530-538.

[18] T. Kiyobayashi, H.T. Takeshita, H. Tanaka, N. Takeichi, A. Züttel, L. Schlapbach, N. Kuriyama, Hydrogen adsorption in carbonaceous materials–How to determine the storage capacity accurately, Journal of Alloys and Compounds, 330-332 (2002) 666-669.

[19] A.F. Bobkov, E.V. Davydov, S.V. Zaitsev, A.V. Karpov, M.A. Kozodaev, I.N. Nikolaeva, M.O. Popov, E.N. Skorokhodov, A.L. Suvorov, Y.N. Cheblukov, The use of carbonaceous materials as field-emission cathodes, Tech Phys+, 46 (2001) 736-742.

[20] Y. Zhang, B.C. Wang, A.M. Nie, C.P. Mu, J.Y. Xiang, F.S. Wen, Z.Y. Liu, Carbonaceous photonic crystals prepared by high-temperature/hydrothermal carbonization as high-performance microwave absorbers, J Mater Sci, 54 (2019) 14343-14353.

[21] F. Qin, C. Brosseau, A review and analysis of microwave absorption in polymer composites filled with carbonaceous particles, J Appl Phys, 111 (2012) 4.

[22] M.J. Allen, V.C. Tung, R.B. Kaner, Honeycomb carbon: a review of graphene, Chem Rev, 110 (2010) 132-145.

[23] P.R. Wallace, The Band Theory of Graphite, Physical Review, 71 (1947) 622-634.

[24] B. Lang, A LEED study of the deposition of carbon on platinum crystal surfaces, Surface Science, 53 (1975) 317-329.

[25] I. Forbeaux, J.M. Themlin, J.M. Debever, Heteroepitaxial graphite on 6H−SiC(0001): Interface formation through conduction-band electronic structure, Physical Review B, 58 (1998) 16396-16406.

[26] K.S. Novoselov, A.K. Geim, S.V. Morozov, D. Jiang, Y. Zhang, S.V. Dubonos, I.V. Grigorieva, A.A. Firsov, Electric field effect in atomically thin carbon films, science, 306 (2004) 666-669.

[27] A.K. Geim, K.S. Novoselov, The rise of graphene, Nanoscience and technology: a collection of reviews from nature journals, (2010) 11-19.

[28] H. Gwon, H.S. Kim, K.U. Lee, D.H. Seo, Y.C. Park, Y.S. Lee, B.T. Ahn, K. Kang, Flexible energy storage devices based on graphene paper, Energ Environ Sci, 4 (2011) 1277-1283.

[29] M. Zhang, X.X. Wang, W.Q. Cao, J. Yuan, M.S. Cao, Electromagnetic Functions of Patterned 2D Materials for Micro–Nano Devices Covering GHz, THz, and Optical Frequency, Advanced Optical Materials, 7 (2019) 1900689.

[30] S. Jang, E. Hwang, Y. Lee, S. Lee, J.H. Cho, Multifunctional graphene optoelectronic devices capable of detecting and storing photonic signals, Nano Lett, 15 (2015) 2542-2547.

[31] G. Yang, L. Li, W.B. Lee, M.C. Ng, Structure of graphene and its disorders: a review, Sci Technol Adv Mater, 19 (2018) 613-648.

[32] P.R. Wallace, The band theory of graphite, Physical review, 71 (1947) 622.

[33] J. McClure, Diamagnetism of graphite, Physical Review, 104 (1956) 666.

[34] J. Slonczewski, P. Weiss, Band structure of graphite, Physical review, 109 (1958) 272.

[35] M. Khantha, N.A. Cordero, L.M. Molina, J.A. Alonso, L.A. Girifalco, Interaction of lithium with graphene: An ab initio study, Physical Review B, 70 (2004) 125422.

[36] Z. Zhen, H. Zhu, Structure and properties of graphene, Graphene, (2018) 1-12.

[37] D. Zhan, J. Yan, L. Lai, Z. Ni, L. Liu, Z. Shen, Engineering the electronic structure of graphene, Adv Mater, 24 (2012) 4055-4069.

[38] H.Q. Lin, J.E. Hirsch, Two-dimensional Hubbard model with nearest- and next-nearest-neighbor hopping, Phys Rev B Condens Matter, 35 (1987) 3359-3368.

[39] A. Bostwick, T. Ohta, T. Seyller, K. Horn, E. Rotenberg, Quasiparticle dynamics in graphene, Nat Phys, 3 (2007) 36-40.

[40] D.L. Miller, K.D. Kubista, G.M. Rutter, M. Ruan, W.A. de Heer, P.N. First, J.A. Stroscio, Observing the quantization of zero mass carriers in graphene, Science, 324 (2009) 924-927.

[41] Y. Zhang, Y.W. Tan, H.L. Stormer, P. Kim, Experimental observation of the quantum Hall effect and Berry's phase in graphene, Nature, 438 (2005) 201-204.

[42] E. McCann, V.I. Fal'ko, Landau-level degeneracy and quantum Hall effect in a graphite bilayer, Phys Rev Lett, 96 (2006) 086805.

[43] R.L. Whitby, Chemical control of graphene architecture: tailoring shape and properties, ACS Nano, 8 (2014) 9733-9754.

[44] Y. Wang, Z. Li, J. Wang, J. Li, Y. Lin, Graphene and graphene oxide: biofunctionalization and applications in biotechnology, Trends Biotechnol, 29 (2011) 205-212.

[45] J.M. Carlsson, Graphene: buckle or break, Nat Mater, 6 (2007) 801-802.

[46] F. Schedin, A.K. Geim, S.V. Morozov, E.W. Hill, P. Blake, M.I. Katsnelson, K.S. Novoselov, Detection of individual gas molecules adsorbed on graphene, Nat Mater, 6 (2007) 652-655.

[47] F. Banhart, J. Kotakoski, A.V. Krasheninnikov, Structural defects in graphene, ACS Nano, 5 (2011) 26-41.

[48] A. Hashimoto, K. Suenaga, A. Gloter, K. Urita, S. Iijima, Direct evidence for atomic defects in graphene layers, Nature, 430 (2004) 870-873.

[49] A.N. Sidorov, M.M. Yazdanpanah, R. Jalilian, P.J. Ouseph, R.W. Cohn, G.U. Sumanasekera, Electrostatic deposition of graphene, Nanotechnology, 18 (2007) 135301.

[50] C. Lee, X. Wei, J.W. Kysar, J. Hone, Measurement of the elastic properties and intrinsic strength of monolayer graphene, Science, 321 (2008) 385-388.

[51] A.A. Balandin, Thermal properties of graphene and nanostructured carbon materials, Nat Mater, 10 (2011) 569-581.

[52] A.A. Balandin, S. Ghosh, W. Bao, I. Calizo, D. Teweldebrhan, F. Miao, C.N. Lau, Superior thermal conductivity of single-layer graphene, Nano Lett, 8 (2008) 902-907.

[53] M.D. Stoller, S. Park, Y. Zhu, J. An, R.S. Ruoff, Graphene-based ultracapacitors, Nano Lett, 8 (2008) 3498-3502.

[54] S.D. Zhang, H.H. Wang, J.P. Liu, C.L. Bao, Measuring the specific surface area of monolayer graphene oxide in water, Mater Lett, 261 (2020) 127098.

[55] N. Wei, L. Xu, H.Q. Wang, J.C. Zheng, Strain engineering of thermal conductivity in graphene sheets and nanoribbons: a demonstration of magic flexibility, Nanotechnology, 22 (2011) 105705.

[56] Y. Lu, F. Yang, G.G.X. Wang, T.Y. Zhang, P. Wang, Recent Development of Graphene-Based Materials for Cathode Application in Lithium Batteries: A Review and Outlook, Int J Electrochem Sc, 14 (2019) 5961-5971.

[57] K.F. Mak, M.Y. Sfeir, Y. Wu, C.H. Lui, J.A. Misewich, T.F. Heinz, Measurement of the optical conductivity of graphene, Phys Rev Lett, 101 (2008) 196405.

[58] Q. Bao, K.P. Loh, Graphene photonics, plasmonics, and broadband optoelectronic devices, ACS Nano, 6 (2012) 3677-3694.

[59] Q.L. Bao, H. Zhang, B. Wang, Z.H. Ni, C.H.Y.X. Lim, Y. Wang, D.Y. Tang, K.P. Loh, Broadband graphene polarizer, Nat Photonics, 5 (2011) 411-415.

[60] S. Song, Q. Chen, L. Jin, F. Sun, Great light absorption enhancement in a graphene photodetector integrated with a metamaterial perfect absorber, Nanoscale, 5 (2013) 9615-9619.

[61] X. Gan, K.F. Mak, Y. Gao, Y. You, F. Hatami, J. Hone, T.F. Heinz, D. Englund, Strong enhancement of light-matter interaction in graphene coupled to a photonic crystal nanocavity, Nano Lett, 12 (2012) 5626-5631.

[62] X. Zhu, L. Shi, M.S. Schmidt, A. Boisen, O. Hansen, J. Zi, S. Xiao, N.A. Mortensen, Enhanced light-matter interactions in graphene-covered gold nanovoid arrays, Nano Lett, 13 (2013) 4690-4696.

[63] A. Ambrosi, C.K. Chua, A. Bonanni, M. Pumera, Electrochemistry of graphene and related materials, Chem Rev, 114 (2014) 7150-7188.

[64] Z.Y. Sun, S. Poller, X. Huang, D. Guschin, C. Taetz, P. Ebbinghaus, J. Masa, A. Erbe, A. Kilzer, W. Schuhmann, M. Muhler, High-yield exfoliation of graphite in acrylate polymers: A stable few-layer graphene nanofluid with enhanced thermal conductivity, Carbon, 64 (2013) 288-294.

[65] Z.Z. Sun, D.K. James, J.M. Tour, Graphene Chemistry: Synthesis and Manipulation, J Phys Chem Lett, 2 (2011) 2425-2432.

[66] H. Ago, CVD growth of high-quality single-layer graphene, Frontiers of Graphene and Carbon Nanotubes, (2015) 3-20.

[67] C. Oncel, Y. Yurum, Carbon nanotube synthesis via the catalytic CVD method: A review on the effect of reaction parameters, Fuller Nanotub Car N, 14 (2006) 17-37.

[68] X. Zhang, J. Ning, X. Li, B. Wang, L. Hao, M. Liang, M. Jin, L. Zhi, Hydrogen-induced effects on the CVD growth of high-quality graphene structures, Nanoscale, 5 (2013) 8363-8366.

[69] Y. Zhang, L. Gomez, F.N. Ishikawa, A. Madaria, K. Ryu, C.A. Wang, A. Badmaev, C.W. Zhou, Comparison of Graphene Growth on Single-Crystalline and Polycrystalline Ni by Chemical Vapor Deposition, J Phys Chem Lett, 1 (2010) 3101-3107.

[70] M. Yudasaka, R. Kikuchi, T. Matsui, Y. Ohki, S. Yoshimura, E. Ota, Specific Conditions for Ni Catalyzed Carbon Nanotube Growth by Chemical-Vapor-Deposition, Applied Physics Letters, 67 (1995) 2477-2479.

[71] B. Wang, M. Huang, L. Tao, S.H. Lee, A.R. Jang, B.W. Li, H.S. Shin, D. Akinwande, R.S. Ruoff, Support-Free Transfer of Ultrasmooth Graphene Films Facilitated by Self-Assembled Monolayers for Electronic Devices and Patterns, ACS Nano, 10 (2016) 1404-1410.

[72] H. Huang, S. Chen, A. Wee, W. Chen, Epitaxial growth of graphene on silicon carbide (SiC), Graphene, (2014) 3-26.

[73] N. Mishra, J. Boeckl, N. Motta, F. Iacopi, Graphene growth on silicon carbide: A review, Phys Status Solidi A, 213 (2016) 2277-2289.

[74] W. Strupinski, K. Grodecki, A. Wysmolek, R. Stepniewski, T. Szkopek, P.E. Gaskell, A. Gruneis, D. Haberer, R. Bozek, J. Krupka, J.M. Baranowski, Graphene epitaxy by chemical vapor deposition on SiC, Nano Lett, 11 (2011) 1786-1791.

[75] J.F. Chen, M. Duan, G.H. Chen, Continuous mechanical exfoliation of graphene sheets via three-roll mill, J Mater Chem, 22 (2012) 19625-19628.

[76] K.S. Novoselov, A.K. Geim, S.V. Morozov, D. Jiang, Y. Zhang, S.V. Dubonos, I.V. Grigorieva, A.A. Firsov, Electric field effect in atomically thin carbon films, Science, 306 (2004) 666-669.

[77] J. Zhao, S. Pei, W. Ren, L. Gao, H.M. Cheng, Efficient preparation of large-area graphene oxide sheets

for transparent conductive films, ACS Nano, 4 (2010) 5245-5252.

[78] S.N. Alam, N. Sharma, L. Kumar, Synthesis of Graphene Oxide (GO) by Modified Hummers Method and Its Thermal Reduction to Obtain Reduced Graphene Oxide (rGO), Graphene, 06 (2017) 1-18.

[79] R. Muzyka, S. Drewniak, T. Pustelny, M. Chrubasik, G. Gryglewicz, Characterization of Graphite Oxide and Reduced Graphene Oxide Obtained from Different Graphite Precursors and Oxidized by Different Methods Using Raman Spectroscopy, Materials, 11 (2018) 1050.

[80] D. Chen, H. Feng, J. Li, Graphene oxide: preparation, functionalization, and electrochemical applications, Chem Rev, 112 (2012) 6027-6053.

[81] M. Romagnoli, V. Sorianello, M. Midrio, F.H.L. Koppens, C. Huyghebaert, D. Neumaier, P. Galli, W. Templ, A. D'Errico, A.C. Ferrari, Graphene-based integrated photonics for next-generation datacom and telecom, Nat Rev Mater, 3 (2018) 392-414.

[82] Q. Bao, H. Zhang, Y. Wang, Z. Ni, Y. Yan, Z.X. Shen, K.P. Loh, D.Y. Tang, Atomic-Layer Graphene as a Saturable Absorber for Ultrafast Pulsed Lasers, Advanced Functional Materials, 19 (2009) 3077-3083.

[83] T. Hasan, Z. Sun, F. Wang, F. Bonaccorso, P.H. Tan, A.G. Rozhin, A.C. Ferrari, Nanotube–Polymer Composites for Ultrafast Photonics, Advanced Materials, 21 (2009) 3874-3899.

[84] S. Goossens, G. Navickaite, C. Monasterio, S. Gupta, J.J. Piqueras, R. Pérez, G. Burwell, I. Nikitskiy, T. Lasanta, T. Galán, E. Puma, A. Centeno, A. Pesquera, A. Zurutuza, G. Konstantatos, F. Koppens, Broadband image sensor array based on graphene–CMOS integration, Nat Photonics, 11 (2017) 366-371.

[85] M.S. Kim, M. Kim, S. Son, S.Y. Cho, S. Lee, D.K. Won, J. Ryu, I. Bae, H.M. Kim, K.B. Kim, Sheet Resistance Analysis of Interface-Engineered Multilayer Graphene: Mobility Versus Sheet Carrier Concentration, ACS Appl Mater Interfaces, 12 (2020) 30932-30940.

[86] F. Xia, T. Mueller, Y.M. Lin, A. Valdes-Garcia, P. Avouris, Ultrafast graphene photodetector, Nat Nanotechnol, 4 (2009) 839-843.

[87] B.N. Shivananju, W. Yu, Y. Liu, Y. Zhang, B. Lin, S. Li, Q. Bao, The Roadmap of Graphene-Based Optical Biochemical Sensors, Advanced Functional Materials, 27 (2017) 1603918.

[88] J.Q. Wang, Z.K. Xing, X. Chen, Z.Z. Cheng, X.J. Li, T.G. Liu, Recent Progress in Waveguide-Integrated Graphene Photonic Devices for Sensing and Communication Applications, Front Phys-Lausanne, 8 (2020) 37.

[89] P. Kossyrev, Carbon black supercapacitors employing thin electrodes, J Power Sources, 201 (2012) 347-352.

[90] Y. Wang, Y. Song, Y. Xia, Electrochemical capacitors: mechanism, materials, systems, characterization and applications, Chem Soc Rev, 45 (2016) 5925-5950.

[91] X. Zhang, H.T. Zhang, C. Li, K. Wang, X.Z. Sun, Y.W. Ma, Recent advances in porous graphene materials for supercapacitor applications, Rsc Advances, 4 (2014) 45862-45884.

[92] Z. Wu, L. Li, J.M. Yan, X.B. Zhang, Materials Design and System Construction for Conventional and New-Concept Supercapacitors, Adv Sci, 4 (2017) 1600382.

[93] C.W. Liew, S. Ramesh, A.K. Arof, Good prospect of ionic liquid based-poly(vinyl alcohol) polymer electrolytes for supercapacitors with excellent electrical, electrochemical and thermal properties, Int J Hydrogen Energ, 39 (2014) 2953-2963.

[94] S. Zhao, C.Y. Wang, M.M. Chen, J. Wang, Z.Q. Shi, Potato starch-based activated carbon spheres as electrode material for electrochemical capacitor, J Phys Chem Solids, 70 (2009) 1256-1260.

[95] W. Hsieh, T.L.A. Horng, H.C. Huang, H.S. Teng, Facile simulation of carbon with wide pore size distribution for electric double-layer capacitance based on Helmholtz models, J Mater Chem A, 3 (2015) 16535-16543.

[96] J.P. Valleau, G.M. Torrie, The electrical double layer. III. Modified Gouy−Chapman theory with unequal ion sizes, The Journal of Chemical Physics, 76 (1982) 4623-4630.

[97] F. Beguin, V. Presser, A. Balducci, E. Frackowiak, Carbons and Electrolytes for Advanced Supercapacitors, Advanced Materials, 26 (2014) 2219-2251.

[98] H.N. Wang, L. Pilon, Accurate Simulations of Electric Double Layer Capacitance of Ultramicroelectrodes, J Phys Chem C, 115 (2011) 16711-16719.

[99] A. Brandt, A. Balducci, Theoretical and practical energy limitations of organic and ionic liquid-based electrolytes for high voltage electrochemical double layer capacitors, J Power Sources, 250 (2014) 343-351.

[100] Q. Abbas, F. Beguin, Sustainable Carbon/Carbon Supercapacitors Operating Down to -40 degrees C in Aqueous Electrolyte Made with Cholinium Salt, ChemSusChem, 11 (2018) 975-984.

[101] A. Lewandowski, A. Olejniczak, M. Galinski, I. Stepniak, Performance of carbon–carbon supercapacitors based on organic, aqueous and ionic liquid electrolytes, J Power Sources, 195 (2010) 5814-5819.

[102] H.V. Nguyen, A. Bin Faheem, K. Kwak, K.K. Lee, Propionitrile as a single organic solvent for high voltage electric double-layer capacitors, J Power Sources, 463 (2020) 228134.

[103] K.L. Van Aken, M. Beidaghi, Y. Gogotsi, Formulation of Ionic-Liquid Electrolyte To Expand the Voltage Window of Supercapacitors, Angewandte Chemie, 127 (2015) 4888-4891.

[104] K.F. Chen, Y.Y. Yang, K.Y. Li, Z.S. Ma, Y.C. Zhou, D.F. Xue, $CoCl_2$ Designed as Excellent Pseudocapacitor Electrode Materials, Acs Sustain Chem Eng, 2 (2014) 440-444.

[105] L.P. Yu, G.Z. Chen, Redox electrode materials for supercapatteries, J Power Sources, 326 (2016) 604-612.

[106] Q. Jiang, N. Kurra, M. Alhabeb, Y. Gogotsi, H.N. Alshareef, All Pseudocapacitive MXene-RuO_2 Asymmetric Supercapacitors, Advanced Energy Materials, 8 (2018) 1703043.

[107] C. Xia, W. Chen, X. Wang, M.N. Hedhili, N. Wei, H.N. Alshareef, Highly Stable Supercapacitors with Conducting Polymer Core-Shell Electrodes for Energy Storage Applications, Advanced Energy Materials, 5 (2015) 1401805.

[108] B. Shen, X. Zhang, R. Guo, J. Lang, J. Chen, X. Yan, Carbon encapsulated RuO_2 nano-dots anchoring on graphene as an electrode for asymmetric supercapacitors with ultralong cycle life in an ionic liquid electrolyte, J Mater Chem A, 4 (2016) 8180-8189.

[109] G.A. Snook, P. Kao, A.S. Best, Conducting-polymer-based supercapacitor devices and electrodes, J Power Sources, 196 (2011) 1-12.

[110] Q.F. Meng, K.F. Cai, Y.X. Chen, L.D. Chen, Research progress on conducting polymer based supercapacitor electrode materials, Nano Energy, 36 (2017) 268-285.

[111] S.R. Sivakkumar, D.R. MacFarlane, M. Forsyth, D.W. Kim, Ionic liquid-based rechargeable lithium metal-polymer cells assembled with Polyaniline/Carbon nanotube composite cathode, Journal of the Electrochemical Society, 154 (2007) A834-A838.

[112] C. Han, H. Li, R. Shi, L. Xu, J. Li, F. Kang, B. Li, Nanostructured Anode Materials for Non-aqueous Lithium Ion Hybrid Capacitors, Energy Environ Mater, 1 (2018) 75-87.

[113] D.P. Dubal, O. Ayyad, V. Ruiz, P. Gomez-Romero, Hybrid energy storage: the merging of battery and supercapacitor chemistries, Chem Soc Rev, 44 (2015) 1777-1790.

[114] G.G. Amatucci, F. Badway, A. Du Pasquier, T. Zheng, An asymmetric hybrid nonaqueous energy storage cell, Journal of the Electrochemical Society, 148 (2001) A930-A939.

[115] R. Thangavel, B. Moorthy, D.K. Kim, Y.S. Lee, Pushing the Energy Output and Cyclability of Sodium Hybrid Capacitors at High Power to New Limits, Advanced Energy Materials, 7 (2017) 1602654.

[116] S.M. Li, S.Y. Yang, Y.S. Wang, H.P. Tsai, H.W. Tien, S.T. Hsiao, W.H. Liao, C.L. Chang, C.C.M. Ma, C.C. Hu, N-doped structures and surface functional groups of reduced graphene oxide and their effect on the electrochemical performance of supercapacitor with organic electrolyte, J Power Sources, 278 (2015) 218-229.

[117] J. Ding, W. Hu, E. Paek, D. Mitlin, Review of Hybrid Ion Capacitors: From Aqueous to Lithium to Sodium, Chem Rev, 118 (2018) 6457-6498.

[118] S.H. Lee, G. Yoo, J. Cho, S. Ryu, Y.S. Kim, J. Yoo, Expanded graphite/copper oxide composite electrodes

for cell kinetic balancing of lithium-ion capacitor, Journal of Alloys and Compounds, 829 (2020) 154566.
[119] S. Zhang, C. Li, X. Zhang, X. Sun, K. Wang, Y. Ma, High Performance Lithium-Ion Hybrid Capacitors Employing Fe_3O_4-Graphene Composite Anode and Activated Carbon Cathode, ACS Appl Mater Interfaces, 9 (2017) 17136-17144.
[120] C. Aphirakaramwong, N. Phattharasupakun, J. Wutthiprom, J. Limtrakul, M. Sawangphruk, A novel high-performance lithium-ion hybrid capacitor using three-dimensional nanostructure of N-doped graphene aerogel and carbon nanotube composite, Ecs Transactions, 85 (2018) 449-468.
[121] H. Gao, F. Xiao, C.B. Ching, H. Duan, High-performance asymmetric supercapacitor based on graphene hydrogel and nanostructured MnO_2, ACS Appl Mater Interfaces, 4 (2012) 2801-2810.
[122] Z. Sun, A. Martinez, F.J.N.P. Wang, Optical modulators with 2D layered materials, 10 (2016) 227-238.
[123] A.E. Minovich, A.E. Miroshnichenko, A.Y. Bykov, T.V. Murzina, D.N. Neshev, Y.S. Kivshar, Functional and nonlinear optical metasurfaces, Laser Photonics Rev, 9 (2015) 195-213.
[124] P.D. Dragic, J. Ballato, 120 Years of Optical Glass Science, Optics and Photonics News, 25 (2014) 44-51.
[125] H.S. Nalwa, Organic materials for third-order nonlinear optics, Advanced Materials, 5 (1993) 341-358.
[126] L. Pedesseau, C. Katan, J. Even, On the entanglement of electrostriction and non-linear piezoelectricity in non-centrosymmetric materials, Applied Physics Letters, 100 (2012) 031903.
[127] M.M. Ara, E. Koushki, S. Salmani, S. Mousavi, χ (3) measurement in "5-oxo-4, 5-dihydroindeno [1, 2-b] pyrans" using the z-scan and the moiré deflectometry techniques, Optics communications, 278 (2007) 418-422.
[128] N. Venkatram, D.N. Rao, M. Akundi, Nonlinear absorption, scattering and optical limiting studies of CdS nanoparticles, Optics express, 13 (2005) 867-872.
[129] S. Chen, C. Zhao, Y. Li, H. Huang, S. Lu, H. Zhang, S. Wen, Broadband optical and microwave nonlinear response in topological insulator, Optical Materials Express, 4 (2014) 587-596.
[130] Y. Chen, G. Jiang, S. Chen, Z. Guo, X. Yu, C. Zhao, H. Zhang, Q. Bao, S. Wen, D. Tang, Mechanically exfoliated black phosphorus as a new saturable absorber for both Q-switching and mode-locking laser operation, Optics express, 23 (2015) 12823-12833.
[131] L.W. Tutt, T.F. Boggess, A review of optical limiting mechanisms and devices using organics, fullerenes, semiconductors and other materials, Prog Quant Electron, 17 (1993) 299-338.

Chapter 2

Experimental Technique

In this chapter, essential background knowledge on experimental techniques was provided. These methods and techniques were used in this dissertation and will be referred in other chapters subsequently.

2.1 Electrochemical Methods

2.1.1 Cyclic Voltammetry

Cyclic voltammetry (CV) has been known as kind of common techniques aiming at investigating electrochemical properties for various materials, such as organic materials, metal oxides, and carbonaceous materials [1]. CV method is also extensively used to assess the electrochemical performance of energy-storage devices including lithium-ion batteries along with supercapacitors arising from its facile operation and multi-functional characteristics. It could provide us qualitative information about the electrochemical properties, as well as quantitative assessment [2]. In a CV measurement, a cycling potential in a specified range was applied to the working electrode with under certain sweep rate (mV/s). Meanwhile, resulting current of that working electrode was monitored as an output variable quantity. Note that the scan rate of voltage can be designed for different reaction systems and research purposes.

Figure 2-1 presented typical schematic representations of cyclic voltammogram for electric double-layer capacitor (EDLC), pseudo-capacitors, along with lithium-ion battery, respectively [3]. For EDLCs as shown in Figure 2-1(a), non-faradaic processes occurred in the electrodes. Rectangular cyclic voltammogram curves could be observed in an ideal device because of the instantaneous reversion of current flow with the changes of working potential. Nevertheless, resistive losses exist unavoidably in a practical EDLCs device. Thus, the shape of CV curves for practical EDLCs has some extent distortions. As for pseudo-capacitors and lithium-ion

batteries, a faradaic reaction process occurred in the working electrode. Their corresponding cyclic voltammograms given at Figure 2-1(b), (c) could reveal much information, such as the potential position of oxidation and reduction reactions in the electrode, the stable working voltage range, and the degree of reversibility in the redox process. Figure 2-1(c) shows oxidation processes proceed with voltages increase in the upper half curve, while the reduction reaction occurs in the lower half with the potential decrease.

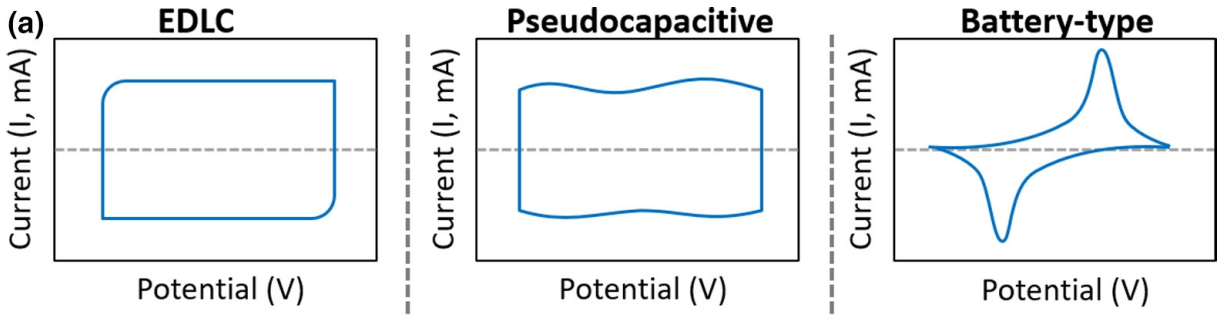

Figure 2-1 Typical schematic representations of cyclic voltammogram curves for (a) EDLCs, (b) pseudo-capacitors, and (c) battery-type devices [4].

2.1.1 Galvanostatic Current Charge and Discharge

Galvanostatic current charging and discharging has been known as another common measurement in electrochemistry to study the behaviors for lithium-ion batteries and supercapacitors. In measurements, the voltage was used as the corresponding signal, and the current was used as the control signal. The charge and discharge process of energy-storage devices were monitored under an invariable current density. The curves in voltage over time was obtained in the end, which could be used to study the behaviors in these devices and the electrochemical properties for electrode materials. Among various purposes, galvanostatic current charge and discharge are often utilized to evaluating the capacitances for the electrodes or device. If being theoretical capacitors, the operating potential changes in linear relations to that proceedings for charges or discharges, and the charge/discharge curves should be symmetrical with a constant slope, seen as Figure 2-2(a). Then these capacitances of the cell (F) can be calculated easily according to an equation 2-1 as below,

$$C = I\frac{\Delta t}{\Delta V} \qquad (2\text{-}1)$$

I represents discharging currents (A) in measurement process, ΔV represents corresponding working potential windows (V), Δt represents the discharging time (s) [5]. However, perfect linearity does not occur often in a nonideal capacitor due to the existence of ohmic resistance in the system. The resistance was induced

by electrodes, electrolyte, and other contact resistance. An instantaneous voltage drops, which was known as IR drop, happens in the capacitor once switching from charging to discharging as shown in Figure 2-2(b). It is highly desired for a capacitor to possess a small IR drop to achieve excellent electrochemical performance, especially at high current densities.

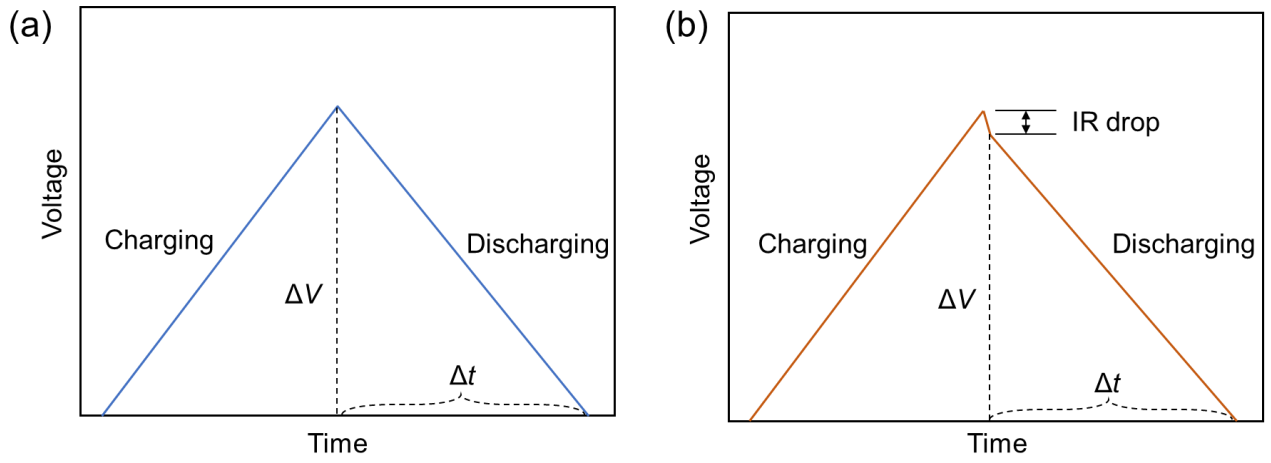

Figure 2-2 Galvanostatic charging/discharging patterns for (a) Theoretical capacitors, (b) Nonideal capacitors possessing an IR potential drop in the discharging process.

2.1.1 Electrochemical Impedance Spectroscopy

Electrochemical impedance spectroscopy (EIS), called likewise to be alternating current (AC) impedance, has been widely used to test the frequency response of supercapacitors or lithium-ion batteries. In the measurement, an alternating current voltage with a small amplitude was applied to the working electrode in different frequencies under the study. As a result, the potential of the electrode will be perturbed near the equilibrium point. The current signal was output with a corresponding amplitude under the action of perturbation. Then the impedance spectrum could be obtained through recording the changes of disturbance signal to time and the response signal to time. The impedance spectrum is also known as the Nyquist plot, which represents the impedance behavior as a function of frequencies [6]. There are many advantages to the electrochemical impedance spectroscopy measurement. This method can measure the materials without destroying the electrode system. Besides, the currents/voltages signals are alternately utilized on equilibrium potential, so these electrodes could be tested for a long time without the accumulation of polarization.

A typical Nyquist plot is composed of two components in a complex-plane as shown in Figure 2-3(a), including imaginary part Z_{im} and real component Z_{re} [7]. A semicircle was observed at high frequencies, which

represents that the process is limited by electron transfer. Note that the semicircle has two intercepts with the Z_{re} axis, where Rs at higher frequencies corresponds to the solution resistance as shown in the equivalent circuit model in Figure 2-3(b). In addition to Rs, R_{CT} that corresponds to the charge-transfer resistance could be evaluated according to another intercept $Rs + R_{CT}$ with Z_{re} axis at lower frequencies. The linear part at low frequencies corresponds to the diffusion-limited process. C_{DL} represents the double-layer capacitances. Meanwhile, Z_w represents Warburg impedances as shown in Figure 2-3(b). C_{DL} can be evaluated from the frequency at the maximum of the semicircle, while the Warburg impedance can be determined by extrapolating the linear part to the real axis.

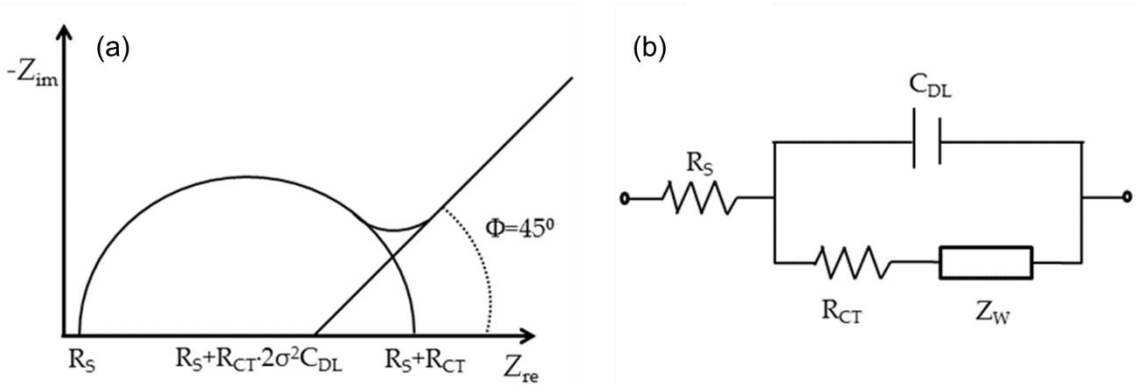

Figure 2-3 (a) Typical Nyquist plot in different frequencies response, and (b) the corresponding equivalent circuit model [7].

2.2 Test Cell Configuration

The electrochemical properties for substances synthesized in this work were characterized using 2032 - type coin cells. The structural configurations of coin cell for lithium-ion batteries half-cell and lithium-ion capacitor full cell used in this thesis were illustrated in Figure 2-4, respectively. A typical lithium-ion battery half-cell shown in Figure 2-4(a) is constructed with a working electrode coating with active materials and lithium metals being counter along with reference electrodes. Then working electrode and lithium metal can be separated instead of electrical connection using the polymer separators. Figure 2-4(b) presents the schematic of a typical lithium-ion capacitor full cell. The devices are constituted using cathode and anode (after pre-lithiation processing). In coin cells, metal foil works as a current collector to conduct the electric current from electrodes efficiently. Note that the electrodes and separator should be fully impregnated by the electrolyte in the coin cell in the assembly process. It is important and beneficial for the ionic current to flow freely between two electrodes.

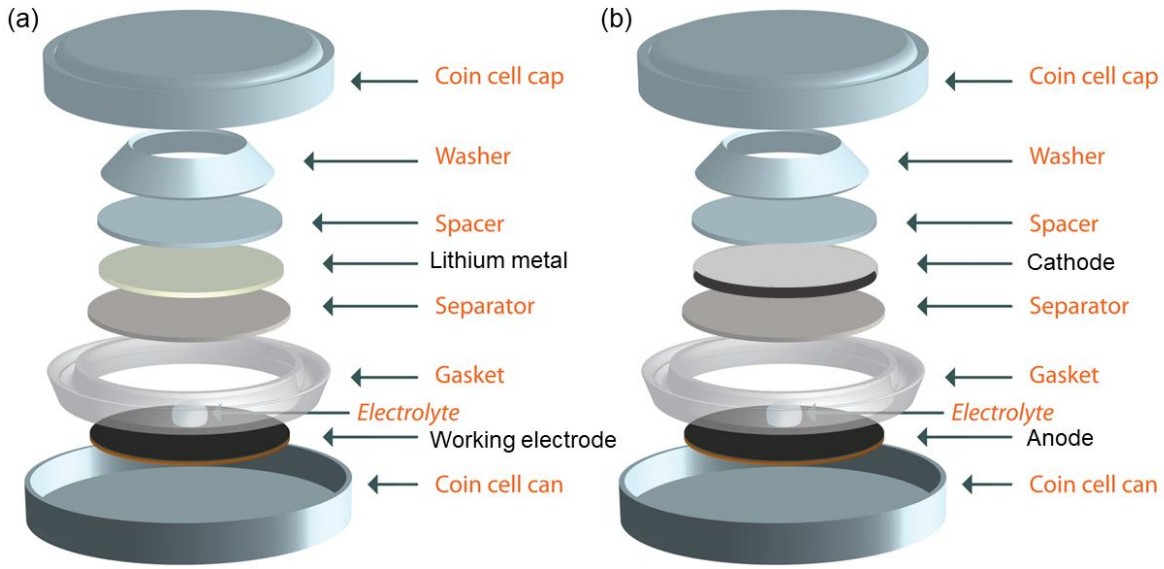

Figure 2-4 Illustrations for (a) lithium-ion batteries half-cell, (b) lithium-ion capacitor full cell.

2.3 Electrochemical Measurement Procedures

The electrochemical performance of a supercapacitor and electrode materials should be assessed from various aspects, including the specific capacitance, cycling stabilities, as well as energy-power densities. Note that evaluated specific capacitance C_{sp} (F/g) for target electrode materials individually could be obtained by using the capacitance C (F) for devices according to following equation 2-2,

$$C_{sp} = 4 \times \frac{C}{m} \qquad (2\text{-}2)$$

where m represents whole mass including negative and positive electrode materials. Note that the specific capacitance of the electrode material is 4 magnifications higher compared to that for the device.

The specific energy densities E_{sp} for supercapacitors are dominated on specific capacitance along with operating potential range according to equation 2-3, with a unit of Wh/kg [8].

$$E_{sp} = C_{cell} \times \frac{V^2}{2} \qquad (2\text{-}3)$$

Note that C_{cell} is the specific capacitance of the device, V is voltage after IR drops.

As for specific power densities for a supercapacitor, it could be estimated following equation 2-4 as below,

$$P_{sp} = \frac{E_{sp}}{\Delta t} \qquad (2\text{-}4)$$

where E_{sp} represents obtained specific energy densities while Δt represents time in discharge process.

2.4 Optical Measurements

2.4.1 UV-VIS

UV-VIS spectrophotometry is a quantitative method that is widely employed aiming at investigating the transmission as well as absorption for materials with a mathematical relation to light wavelength. Typically, as the resonant photon energy gets absorbed by the sample, electrons in the ground energy level move to the upper excited level. The absorption intensity is dependent on the energy states' density of the equivalent transition. As a result, the transmission and absorbance spectra could be obtained through monitoring the absorption versus photon wavelength or energy [57]. Figure 2-5 presents the UV-VIS spectrophotometer used in this thesis. In V-670 double-beam spectrophotometers, distinct and single monochromators set-ups were adopted to be effective in large wavelength range of 190 to 2700 nm (3200 nm option).

Figure 2-5 UV-VIS spectrophotometer.

2.4.2 Spectroscopic Ellipsometry

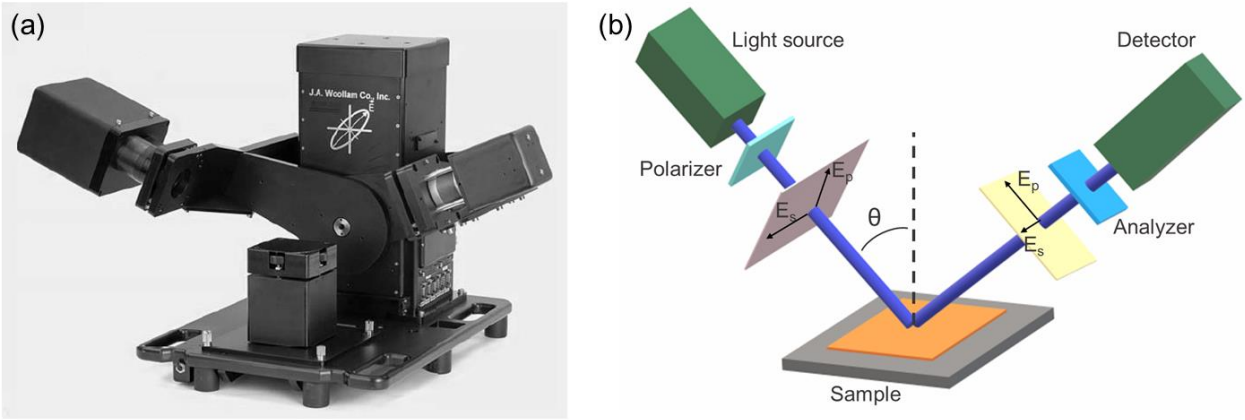

Figure 2-6 (a) Spectroscopic Ellipsometer in the experiments. (b) Schematic representation of the ellipsometry measurement set-up.

Spectroscopic ellipsometry (SE) is one of the prominent techniques to characterize the thickness, permittivity, and linear optical properties of materials through measuring the light reflection from thin films [9]. SE method is very powerful and widely used in optical research due to its sensitivity, flexibility, and self-referenced nature. Spectroscopic Ellipsometer was used in this thesis with a light source of Halogen light and Deuterium light as shown in Figure 2-6(a). In the measurement, the incidence angle of light could be operated from 45 to 90 degrees. The working spectral range could change from 250 to 1000 nm in broadband. To explain the working mechanisms of a spectroscopic ellipsometer, an illustrating image for experimental set-ups was presented as Figure 2-6(b). To be specific, the light source was first converted to an arbitrary polarization state by using a variable polarizer. Then the beam was applied on the sample as an incident light with angle θ. The polarization status for these reflected beams changed when completing interaction with measured thin films. Two perpendicular states in the polarized condition for reflected beams could be detected when completing transmission across the analyzer, which is measured as the complex s and p reflection coefficients. The properties of materials could be determined according to the reflected changes of polarized light at certain angles. The changes in polarization of light after reflection are measured as the ratio of r_p to r_s, which is reflection coefficient for s along with p polarized lights, respectively. Ellipsometry measurements are very sensitive to these surface and concentration of thin films. In the SE measurement, two key parameters were obtained, which are the amplitude ratio Ψ, phase varieties Δ within p to s waves in polarization. Ψ, Δ can be

calculated according to the formula 2-5 [10]:

$$\tan\Psi \exp(i\Delta) = \frac{r_p}{r_s} \qquad (2\text{-}5)$$

In the thin films, interference patterns occurred because of the interaction between reflections from the second surface and top surface. Thus, the thickness, refractive index, and dielectric function could be evaluated by analyzing the interference patterns measured in SE. However, these properties cannot be translated directly from the Ψ and Δ data. The calculation should be established based on the optical model that fitted the samples well. In the fitting process, a variety of oscillators are often utilized such as Cauchy, Drude, Lorentz, and B-spline. In the end, mean squared error (MSE) is a type parameter to estimate the fitting quality, which compared the model-generated data with the measured Ψ and Δ data. MSE should be less than 10 for a reasonable fitting. In addition to small MSE, the fitting result should also have reasonable physical meanings instead of just a mathematic solution.

2.4.3 Pump and Probe Spectroscopy

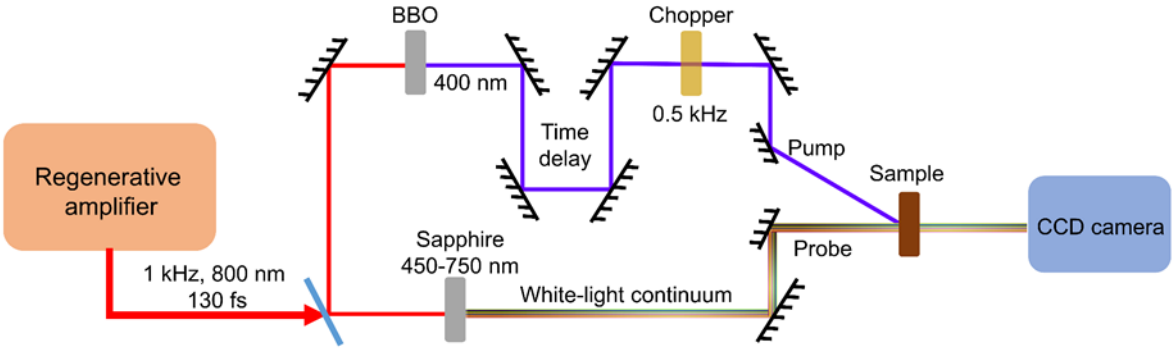

Figure 2-7 The schematic for the pump and probe spectroscopy measurement.

The nonlinear optical property could be investigated through customized pump-probe spectroscopies. Compared to Z-scan, this technique can provide nonlinear optical information in a wide and continuous wavelength range. The schematic drawing of the pump and probe measurement was presented in Figure 2-7. In the measurement, the fundamental laser source was supplied using regenerative amplifiers (Spectra-Physics, Spitfire) with Ti: sapphires (Mai Tai, Spectra-physics) along with Nd: YLF (Empower, Spectra-physics). The laser source has output pulses around 130 fs in wavelength of 800 nm along with 1 kHz repetitions. Then

fundamental laser beams were separated to different portions: pump and probe beams. Obtained wavelength of pump beams possesses 400 nm, which was converted by a BBO crystal through second harmonic generation. In addition, the repetition of the pump beam was converted to 0.5 kHz using optical choppers. Obtained probe laser is white-light continuums with a wavelength ranging from 450 to 750 nm, which was generated using a sapphire crystal.

A strong chip effect exists in the probe white-light continuum because of the group velocity dispersion through the nonlinear crystal. The nonlinearity of $LiNbO_3$ was measured to evaluate the group velocity dispersion as shown in Figure 2-8. All the raw data in the experiment was corrected by group velocity dispersion.

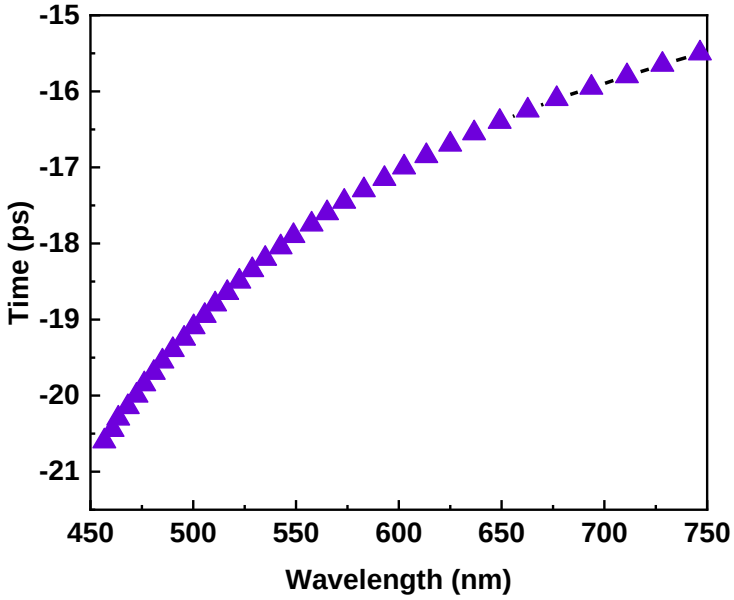

Figure 2-8 Group velocities corrections evaluated through conducting optical nonlinearities using $LiNbO_3$.

References

[1] Y. Denis, C. Fietzek, W. Weydanz, K. Donoue, T. Inoue, H. Kurokawa, S. Fujitani, Study of $LiFePO_4$ by cyclic voltammetry, Journal of the electrochemical society, 154 (2007) A253.

[2] A. Cadena, A.C. Texier, I. Gonzalez, F.J. Cervantes, J. Gomez, Qualitative and quantitative determination of a humic model compound in microbial cultures by cyclic voltammetry, Environ Technol, 28 (2007) 1035-1044.

[3] Y.Q. Jiang, J.P. Liu, Definitions of Pseudocapacitive Materials: A Brief Review, Energy Environ Mater, 2 (2019) 30-37.

[4] J.C. Danilewicz, Review of Oxidative Processes in Wine and Value of Reduction Potentials in Enology, Am J Enol Viticult, 63 (2012) 1-10.

[5] D. Lee, J.Y. Jung, M.J. Jung, Y.S. Lee, Hierarchical porous carbon fibers prepared using a SiO_2 template for high-performance EDLCs, Chem Eng J, 263 (2015) 62-70.

[6] R. Ruffo, S.S. Hong, C.K. Chan, R.A. Huggins, Y. Cui, Impedance Analysis of Silicon Nanowire Lithium Ion Battery Anodes, J Phys Chem C, 113 (2009) 11390-11398.

[7] D.V. Ribeiro, J.C.C. Abrantes, Application of electrochemical impedance spectroscopy (EIS) to monitor the corrosion of reinforced concrete: A new approach, Constr Build Mater, 111 (2016) 98-104.

[8] B. Kim, H. Chung, W. Kim, High-performance supercapacitors based on vertically aligned carbon nanotubes and nonaqueous electrolytes, Nanotechnology, 23 (2012) 155401.

[9] J.W. Weber, V.E. Calado, M.C.M. van de Sanden, Optical constants of graphene measured by spectroscopic ellipsometry, Applied Physics Letters, 97 (2010) 091904.

[10] R. Secondo, D. Fomra, N. Izyumskaya, V. Avrutin, J.N. Hilfiker, A. Martin, O. Ozgur, N. Kinsey, Reliable modeling of ultrathin alternative plasmonic materials using spectroscopic ellipsometry, Optical Materials Express, 9 (2019) 760-770

Chapter 3

Reduced Graphene Oxide Decorated with Crystallized Cobalt Borate Nanoparticles as an Anode in Lithium-ion Capacitors

3.1 Introduction

As a result of the rapidly increasing demands for portable electronic devices, electric vehicles, along with other renewable energy products, advanced energy-storage devices that can provide good cycling stabilities, and high energy and power density are highly desired [1, 2]. In the past decades, substantial efforts have been devoted to the investigation on electrochemical energy storage and deliver devices. Among this research, lithium-ion batteries (LIBs) as well as electric double-layer capacitors (EDLCs) have drawn enhanced attractive notice [3-5]. However, LIBs and EDLCs are unable to satisfy the demands on aspects of high energy and power densities simultaneously, ascribed to the own electrochemical mechanism. As for the applications of LIBs, there are some obstacles such as limited power density and cycle life, though they possess the merits such as high capacities and energy densities [6]. The reason contributing to above effects is Faradaic reactions occur on the electrode in LIBs, which leads to low power densities as well as a short cycling life arising from slow kinetics in charging and discharging processes. From other point of view, applications of EDLCs have been hindered by the relatively low energy density though they show the advantageous property of high-power densities along with good cycling stabilities [7]. Because of EDLC stores energies through reversible ions adsorption/desorption or redox reactions on surface in short time. Hence, it would be urgently needed to explore a new kind of cell to connect gaps from LIBs to EDLCs. To meet this social need, lithium-ion capacitors (LICs) are viewed to be a solution that can balance gaps between LIBs and EDLCs [8].

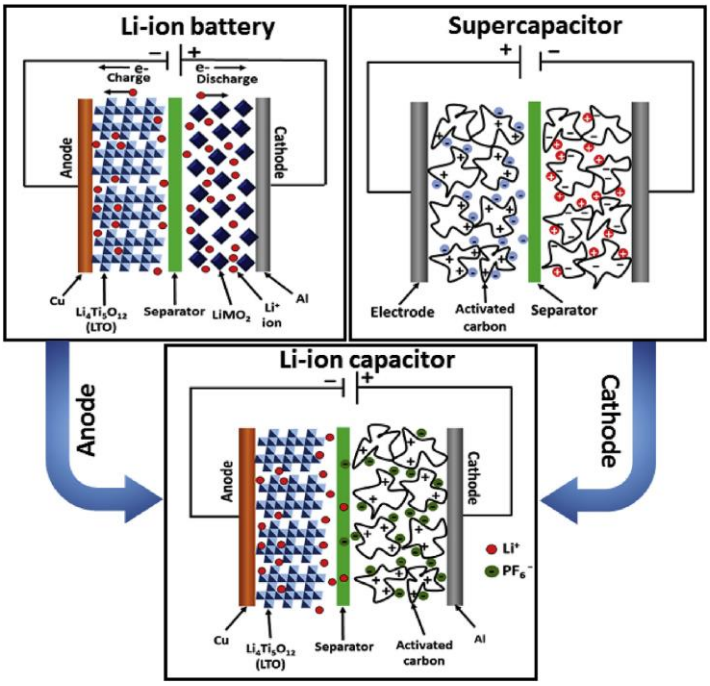

Figure 3-1 The schematic construction of the lithium-ion capacitor [9].

LICs known as an innovative type of hybrid supercapacitors have been considered as a solution to integrate the merits of LIBs and EDLCs. Generally, LICs are constructed with an EDLC-type electrode as the cathode and LIB-type electrodes as anode with $LiPF_6$-based electrolytes as illustrated in Figure 3-1 [10]. As a result of this configuration, LICs can store energy via simultaneously utilizing reversible adsorption/desorption of ions as well as faradaic reactions in the cathode and anode, respectively [11]. As for cathode, many carbonaceous materials were adopted, such as activated carbon and graphene. As for anode, it was usually processed by pre-lithiation with lithium ions (Li^+) to decrease the working potential using lithium metal as the counter electrode before assembling LICs [12]. As known for capacitors, the capacitance could be calculated according to Equation 3-1:

$$\frac{1}{C} = \frac{1}{C_{cathode}} + \frac{1}{C_{anode}} \qquad (3\text{-}1)$$

Since the capacities for anodes equal the value for cathodes in electric double-layer capacitors, then capacitance for the EDLCs device could be calculated as $C_{EDLCs} = \frac{C_{cathode}}{2}$. In contrast, because redox reactions happen in the anode for LICs, resulting in that capacities of anode electrode is much larger compared to positive electrode, so the capacitance of LIC could be increased than EDLC. Besides, as presented in Figure 3-2, the working potential of the anode in LICs decreased after the pre-lithiation compared to EDLCs. The

energy density of capacitors could be calculated according to equation 3-2.

$$E = \frac{1}{2}CV^2 \qquad (3\text{-}2)$$

Therefore, LICs can store more energy with a higher capacitance as well as a higher working voltage range. In addition, adsorption/desorption of ions proceeds fast in the cathode of LICs as in EDLCs. Hence the high-power density of EDLCs can be retained efficiently in LICs [13].

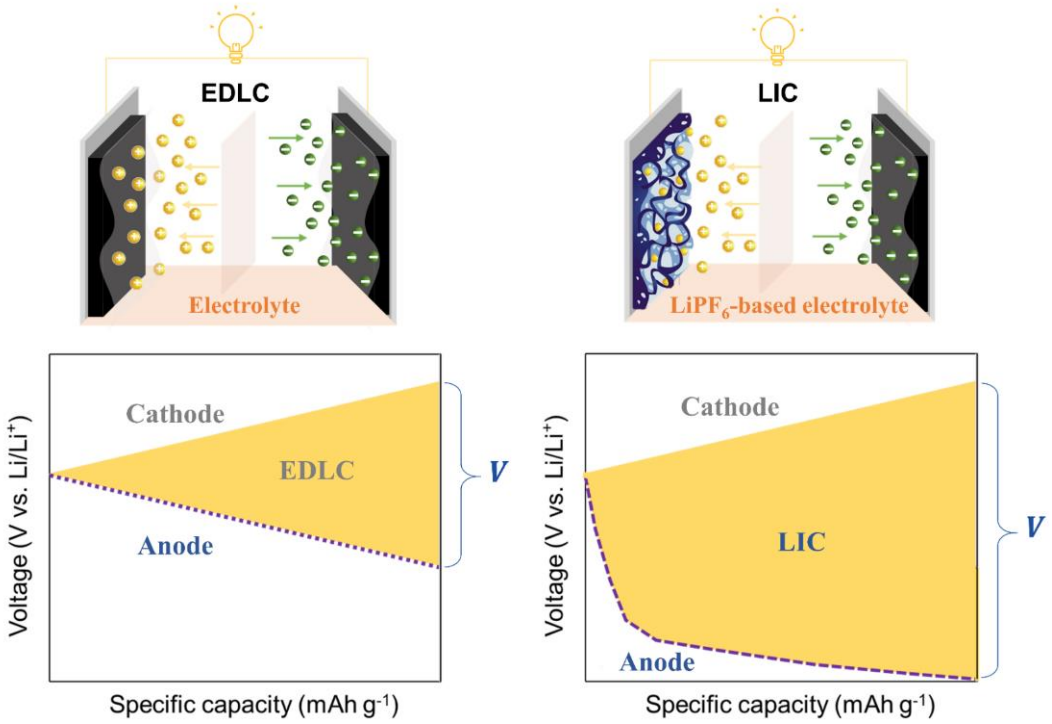

Figure 3-2 Schematic illustration of mechanism and potential profiles in EDLC and LIC.

Although graphite materials have been enormously used working in negative electrode in LICs, graphite suffers from low specific capacities [14]. Therefore, various alternative has also been explored to be negative electrode in LICs, for instance, MnO [15], TiO2 [16], VN [17], and Sn-based materials [18-20]. Unfortunately, their applications are limited by the sluggish diffusion and redox reaction kinetics of Li^+ [21]. Furthermore, on the basis of capacities equation (3-1) for LICs [22], the anode must achieve high capacity so that the capacitance of the cathode can be utilized efficiently. To this end, it's desired to explore prospective choice that can provide high specific capacities, good rate performance, as well as cycling stability.

Reduced graphene oxide (rGO) emerges to be prospective anode materials in LICs, arising from high theoretical surface areas, porous structure, excellent electrical conductivity, and high chemical stability [23].

Besides, the raw material in the fabrication is graphite, so it has great potential to achieve mass production. Therefore, rGO is considered as a kind of competitive choices in the anodes of the lithium-ion capacitor. However, the large irreversible specific capacity and low initial columbic efficiency of rGO affect its utilization unfavorably [24]. Furthermore, the low electron transfer speed in the cross-plane direction impedes its redox kinetics, which is another obstacle when employed as an anode in LICs. Significant amounts of efforts have been devoted to addressing these above hurdles of rGO. For instance, the Fe_2O_3/rGO composite was prepared as an anode [25, 26]. A sandwich-like hierarchical structure was constructed in the manganese oxide/rGO composite, aiming to improve the electrochemical properties [27, 28]. Our group also synthesized the carbon nanotube and rGO composite in previous work, which exhibited improved electrochemical performance [29, 30]. These previous reports illustrate that the construction of a hybrid structure is a viable strategy to modulate the electrochemical properties of rGO by coupling with other materials as spacers [31, 32].

Cobalt borate particles with tens of microns in diameter were reported as anode material for LIBs, which was prepared by rheological phase treatment and ball-milling [33]. More recently, amorphous cobalt borate particles grown on graphene were also explored as anode for LIBs, which indicated that cobalt borate has a great potential to bond with Li^+ [34]. Previous studies about cobalt borate grown on rGO nanosheets have been focused on the large amorphous cobalt borate particles [35]. However, it's acceptable that lithium storage properties for anode electrodes are dependent on significantly the crystallinity and particle size [36]. Motivated by the above considerations, it is of great interest to decorate rGO with the crystallized cobalt borate nanoparticles, which is expected to exhibit an enhancement of the lithium storage properties as an anode in LICs. Herewith we introduce a facile method to grow in-situ crystallized cobalt borate nanoparticles on rGO (Co-B/rGO). The introduction of cobalt borate nanoparticles can alleviate the aggregation of rGO nanosheets. Besides, it also provides more active sites for lithium storage when cobalt borate nanoparticles are anchored on the surface of rGO [37]. Our experimental results and analysis show that the Co-B/rGO composite improves the electrochemical performance of LICs when employed as the anode material. It indicates that rGO decorated with crystallized cobalt borate nanoparticles can be kind of prospective negative electrode material in LICs, propelling realizations of energy-storage systems with high-performance.

3.2 Experimental

3.2.1 Synthesis of Co-B/rGO Composite Materials

Graphene oxide (GO) materials were prepared using the modified Hummers methods introduced in previous literature and graphite flake as the raw material [38]. To be specific, 0.5 g graphite powders (with size 6 - 10 μm, Sigma-Aldrich) along with 0.25 g $NaNO_3$ (Alfa Aesar) were mixed firstly in a 500 mL beaker under stirrings. Then the beaker was filled with 50 mL H_2SO_4 (Nacalai Tesque, 98%) in an ice-water bath under stirrings. Above solution were then processed at room temperature over 24 hours at the back of adding 1.5 g $KMnO_4$ (Chameleon Reagent). A yellow suspension was obtained after dropping 100 mL deionized (DI) followed by 30 mL H_2O_2 (Santoku Chemical Industries Co., LTD) until reactions were completed. In the end, the suspension was washed through centrifugation using HCl and water respectively until the PH reached 7.

In a typical synthesis process of the Co-B/rGO composite, homogenous GO aqueous dispersion (0.5 mg/ml) was obtained by fully dispersing GO in de-ionized (DI) with ultra-sonication. $Co(NO_3)_2 \cdot 6H_2O$ aqueous mixtures were dropped to the prepared GO mixture (100 ml) slowly under vigorous stirring for 2 hours at room temperature. After Co^{2+} ions were anchored at surface of GO nanosheet, 400 mg sodium borohydride ($NaBH_4$) was added into the above solution subsequently and maintained for 6 hours at 80 ℃ under continuous stirring. As a reference, blank rGO was prepared via the same procedure without adding $Co(NO_3)_2 \cdot 6H_2O$. Blank cobalt borate (Co-B) was synthesized without the addition of GO. All products are finally obtained by filtration, washing using DI, followed by drying under 40 ℃ under vacuum over 24 hours.

3.2.2 Fabrication of Anode and Cathode Electrodes

For fabrication of anode electrodes, the slurries were made firstly via dispersing Co-B/rGO composites (80%), polyvinylidene fluoride (PVDF) (10%), along with carbon black powders (10%) within organic solvent N-methyl-2-pyrrolidone (NMP). As-prepared homogenous slurries were obtained after stirring the mixture for 6 hours at room temperature. Then a uniform layer of the as-prepared mixture on a copper current collector was fabricated by coating with a doctor blade. The resultant film was processed under vacuum at 90 ℃ overnight to remove the solvent and cut into disks to be anode electrodes.

Talking about positive electrodes, then slurries were prepared firstly by dispersing rGO (80%), polyvinylidene fluoride (PVDF) (10%), conductive carbon black (10%) within organic solvent N-methyl-2-

pyrrolidone (NMP). As-prepared homogenous slurries were obtained after stirring the mixture for 6 hours at room temperature. Then a uniform layer of the as-prepared mixture on an aluminum current collector was fabricated by coating with a doctor blade. The resultant film was processed under vacuum at 60 ℃ for overnight to remove the solvent and cut into disks as the cathode electrode.

3.2.3 Pre-lithiation of the Anode Electrode

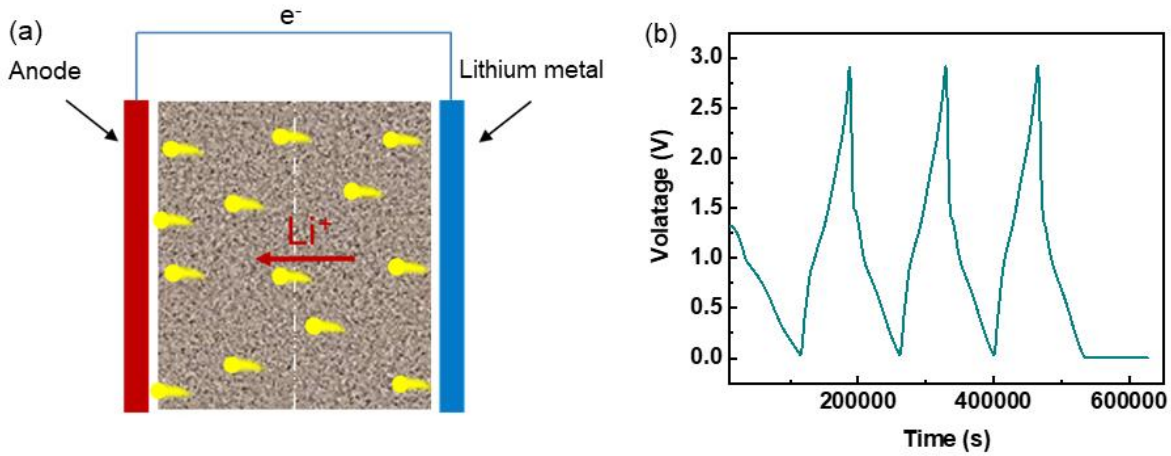

Figure 3-3 (a) The illustrating image for pre-lithiation of anode electrode. (b) Charging/discharging profiles of Co-B/rGO composite electrode in the pre-lithiation process at current density about 50 mA g^{-1}.

As introduced, pre-lithiation processes for anode electrode is important for the electrochemical behaviors of lithium-ion capacitors full cells. In pre-lithiation process, lithium-ion batteries half-cell was used with the Co-B/rGO composite being working electrodes along with lithium metals being counter electrodes, as well as $LiPF_6$-based electrolytes. As shown in Figure 3-3(a), lithium ions transfer from lithium metal to target pre-lithiated electrode during the first step. Consequently, the voltage for above target pre-lithiated electrode decreased from substantial open-circuit voltage (OCV) to 0.005 V through discharging with the current densities set as 50 mA g^{-1}. In this discharging process, lithium intercalation occurred in the Co-B/rGO composite electrode, which leads in accumulation phenomena with the solid electrolyte interface (SEI) at surface of pre-lithiated working electrodes. Typical charging/discharging curves of the Co-B/rGO // lithium half-cell were displayed in Figure 3-3(b). The pre-lithiation was completed when charging/discharging was cycled three times. The curves almost did not change from the second scan, indicating good reversibility and stable behavior. The potential of the pre-lithiated Co-B/rGO electrode was kept at 0.005 V at the end of the third cycle, which was used to assemble a lithium-ion capacitor full cell. Compared with external short circuits

and directly meet lithium metal, the electrochemical circuit method controlled by the electrochemical working station is easy to control the pre-lithiation degree and speed.

3.2.4 Microstructural Characterizations

The microstructural morphologies were investigated on the field emission scanning electron microscopy (SEM) (JEOL JSM-6500) and transmission electron microscopy (TEM) (JEOL JEM-2100 F1). The phase compositions of obtained samples were examined on a powder X-ray diffraction (XRD). The XRD patterns were collected using Rigaku Mini Flex equipped in Cu-Kα radiation (wavelength around 0.154 nm) at 15 - 60° and Cr-Kα radiation (wavelength around 0.229 nm) at 18 - 140°, respectively. Raman spectroscopy was obtained under 532 nm excitations with laser powered in 10 mW. The information about chemical bonding and composition was examined using X-ray photoelectron spectroscopy (XPS, PHI Quantira SXM, ULVAC-PHI). The specific surface area was evaluated according to nitrogen adsorption/desorption isotherms, as well as pore size distributions. Thermogravimetric analysis (TGA) characterization is performed using the STA449F3 Jupiter (NETZSCH) and carried out in a nitrogen atmosphere ranging in 30 - 800 ℃ using the heat speed under 10 ℃/min.

3.2.5 Electrochemical Measurements

In the assembling process of LIBs half-cells (CR 2032-type coin cell), the lithium metal disks served to be counter electrode, with a separator of polypropylene and the electrolyte of $LiPF_6$ (1 M solution that was mixed in EC and DMC solvent with the ratio under 1: 1 in volume). To be compared, electrodes of blank rGO and blank Co-B were also prepared and assembled in a coin cell.

LIC full cells were fabricated using pre-lithiated Co-B/rGO as an anode and rGO as a cathode with a $LiPF_6$ electrolyte using the same CR 2032-type coin cells. The electrolyte in the LIC full cell was $LiPF_6$ (1 M solution that was mixed in EC and DMC solvent under the ratio 1: 1 in volume). Above entire assembly procedures of coin cells were operated under the protection of argon in the glove box. Galvanostatic charge-discharge measurements of the Co-B/rGO LIBs half-cell were carried out in the range of 50 - 5000 mA g^{-1} under room temperature (Land Battery Testing System, 0.005 - 3 V). In contrast, the working voltage of LICs ranges from 0 to 4.3 V. The VMP3 Electrochemical Workstation (Bio-logic Inc.) can be employed to measure the cyclic voltammetry (CV), the electrochemical impedance spectroscopy (EIS).

3.3 Results and Discussion

3.3.1 Structural Characterizations of Co-B/rGO

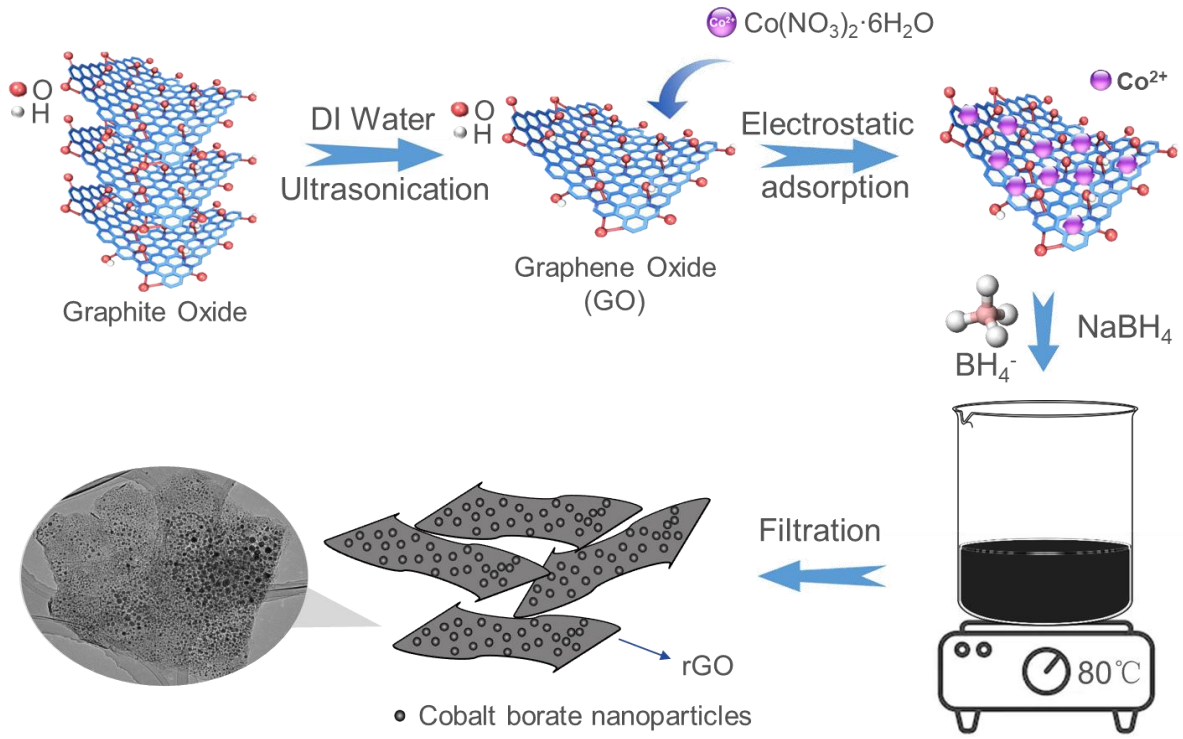

Figure 3-4 The schematics for the preparation procedures about Co-B/rGO composites.

In the synthesis process, the rGO plane worked as the substance that can provide enormous amount of active locations for growths of cobalt borate nanoparticles, as illustrated in Figure 3-4. It was demonstrated in previous literature that graphene oxide exhibits negative zeta potential signs because of the introduction with electronegative functional groups during oxidation processes [39]. Arising from electrostatic interactions within GO nanosheets in negative charging GO and cobalt ions (Co^{2+}) in positive charging, many Co^{2+} ions were adsorbed on the surface of GO nanosheets after a few hours. An excessive amount of $NaBH_4$ was added to the above solution which worked as the source of boron reacting with Co^{2+} to form cobalt borate nanoparticles, simultaneously as the reduction reagent to reduce GO. The brown solution turned black after the reaction. The resultant material named Co-B/rGO was collected through filtration and washing.

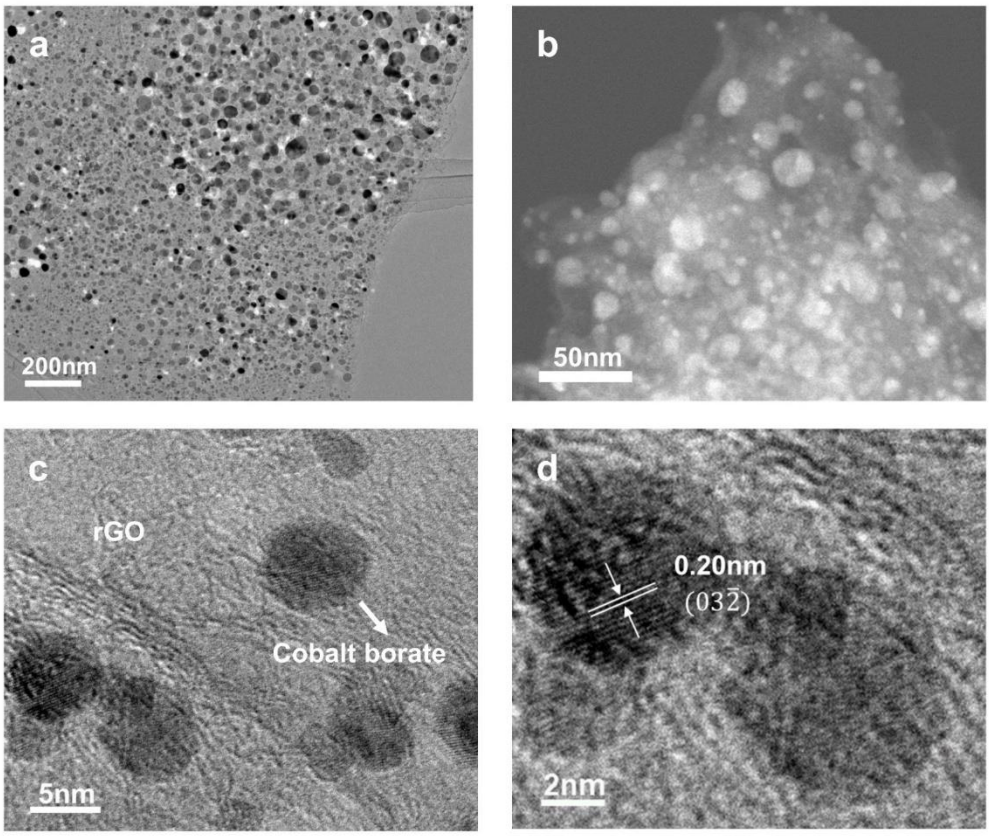

Figure 3-5 (a) TEM image, (b) STEM image, (c, d) HRTEM of the Co-B/rGO composite.

Figure 3-5 presented the TEM images of the Co-B/rGO composite. It reveals that the size of nanoparticles is around 5 to 20 nm in diameter, which distribute on the surface of rGO nanosheets uniformly as shown in Figure 3-5(a). The morphological features of these particles in the composite were probed using scanning transmission electron microscopy (STEM). From observations presented as Figure 3-5(b), synthesized particles display nanospheres morphologies with size in agreement with the HRTEM images shown in Figure 3-5(c). Besides, the close examination of nanoparticles in composite was operated by high-resolution TEM (HRTEM) presented as Figure 3-5(d), besides, the crystal structure possessing d-spacing around 0.20 nm corresponds with lattice planes labeled $(03\bar{2})$ of $Co_2(B_2O_5)$ reasonably. The co-existence of boron (B), cobalt (Co), carbon (C), and oxygen (O) in the Co-B/rGO composite were identified using STEM elemental mapping as shown in Figure 3-6.

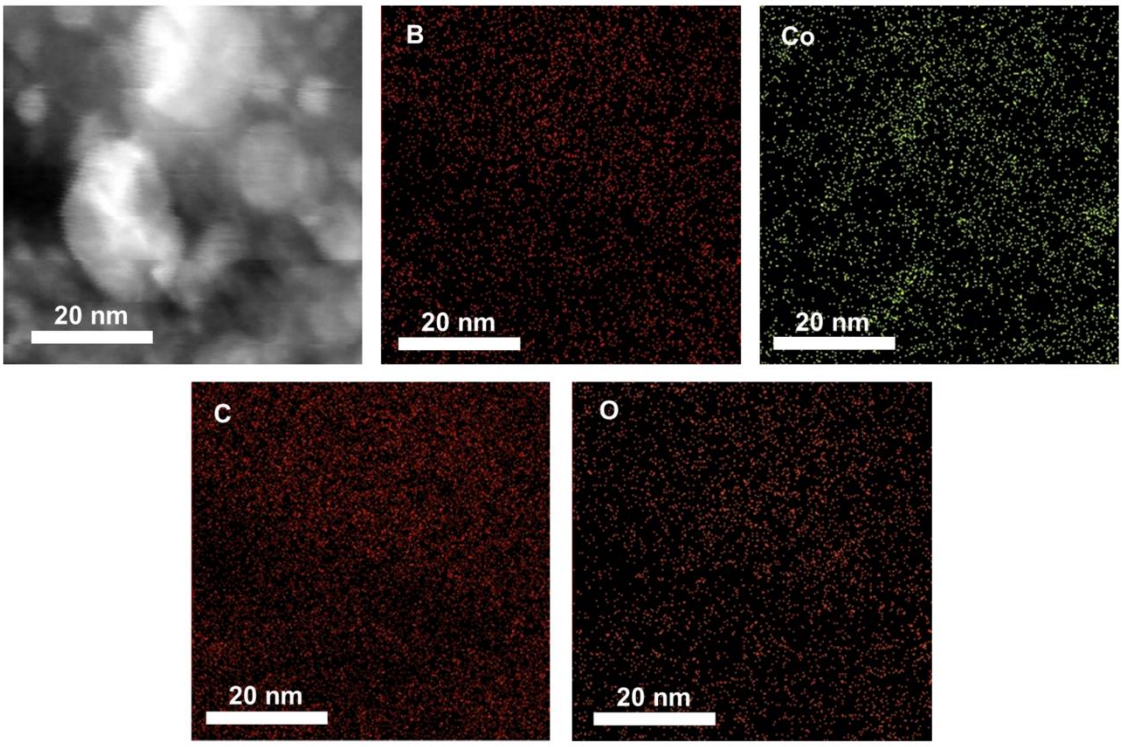

Figure 3-6 STEM images along with accompanying EDS elemental mappings for boron (B), cobalt (Co), carbon (C), and oxygen (O) in high-resolution, scale bar is 20 nm.

In addition, the morphologies of the Co-B/rGO composite were explored using SEM measurements seen at Figure 3-7. rGO sheets can be observed to be very thin without obvious aggregation, due to the influence of cobalt borate nanoparticles served as spacers.

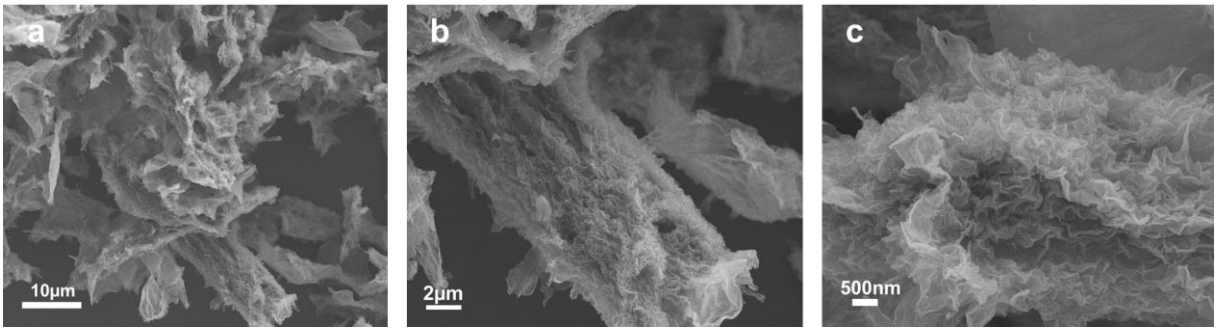

Figure 3-7 (a, b) Low-resolution, (c) high-resolution SEM morphologies for Co-B/G products when reacting mass ratio of Co^{2+}/GO is 3/1.

Note that reacting adding ratio for Co^{2+}/GO would exhibit impact on obtained morphologies of Co-B/rGO composite as illustrated in Figure 3-8. When the amount of Co^{2+} was low, few particles were produced on the surface of rGO that is not enough to support the nanosheets without aggregation. As a result, bulk rGO was

still easy to be formed. When the mass ratio of Co^{2+}/GO increased, a cobalt borate nanoparticle layer was developed between rGO nanosheets, forming a sandwich-like structure. When the mass ratio between Co^{2+} and GO rises to 4 and more, bulk Co-B was formed in the composite. The optimized mass ratio in the Co-B/rGO composite is Co^{2+}/GO = 3/1.

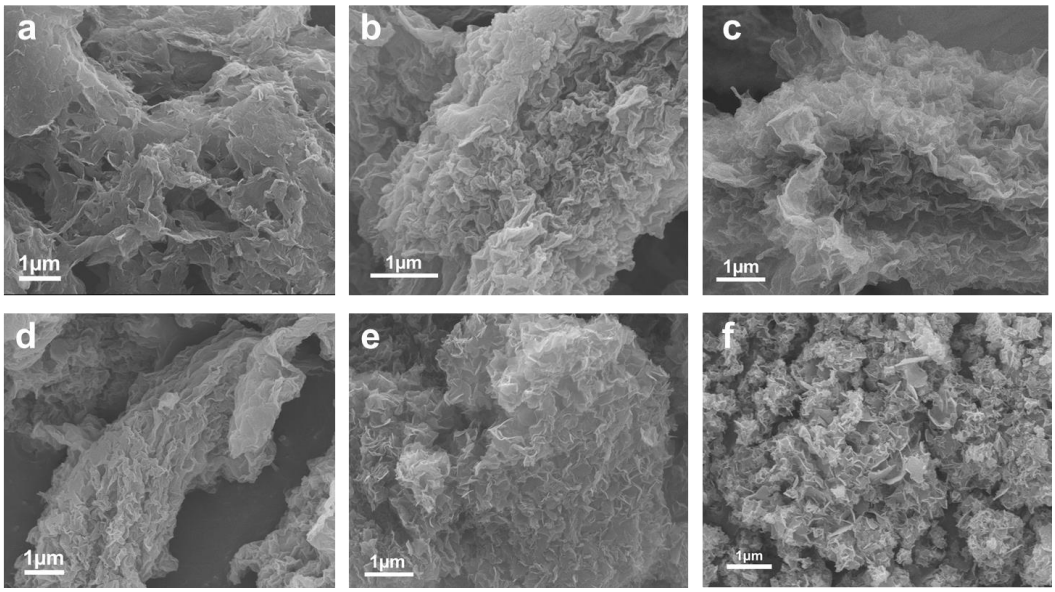

Figure 3-8 SEM images of Co-B/rGO composites with different Co^{2+}/GO mass ratio: (a) blank rGO, (b) Co^{2+}/GO =2/1, (c) Co^{2+}/GO=3/1, (d) Co^{2+}/GO=4/1, (e) Co^{2+}/GO=6/1, and (f) blank Co-B.

Because the cobalt element exists in the samples, the X-ray energy from Cu-Kα radiation is almost comparable to the absorption edge of the cobalt element. Thus, fluorescent X-ray would be enhanced significantly, and a large background signal probably hides or superimpose the main Bragg signals. In contrast, X-ray energies are less compared to absorption edges in Co for the Cr-Kα case. Therefore, considering the existence of a cobalt element in the as-prepared composite, XRD with Cr-Ka radiation was preferred in this work to investigate the crystalline information of the composites. In addition, a comparison was carried out by using the Cu-Ka radiation as shown in Figure 3-9(a), peak location and 2 theta range are different with the result measured by Cr-Ka radiation due to the different X-ray wavelengths.

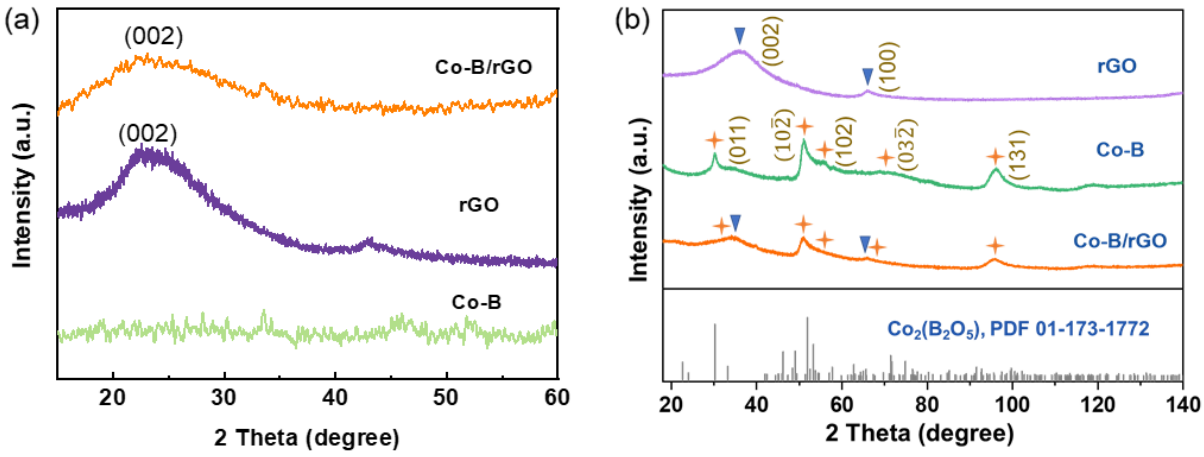

Figure 3-9 (a) XRD patterns of Co-B/rGO, blank rGO, and Co-B in Cu-Kα radiation. (b) XRD of rGO, Co-B, and Co-B/rGO in Cr-Kα radiation.

Figure 3-9(b) presented the XRD results (in Cr-Kα radiation) of rGO, Co-B, along with the Co-B/rGO composite, respectively. Several peaks could be measured in blank Co-B and Co-B/rGO composite. These peaks are well-indexed to the crystalline phase of $Co_2(B_2O_5)$, (PDF 01-173-1772). It is in good agreement with the lattice spacing that was examined in the HRTEM image as discussed. As a result of the above analyses, it was demonstrated that crystallized cobalt borate nanoparticles were successfully introduced on the rGO nanosheets. Raman spectra of the Co-B/rGO composite was shown in Figure 3-10, with a comparison of rGO and pure cobalt borate. The peaking position at 1590 cm^{-1} in the Co-B/rGO composite can be ascribed to the vibration of sp^2 carbons. The peaking position under 1350 cm^{-1} can be ascribed to some defects induced vibrations. These result in Co-B/rGO composite are consistent with that of rGO.

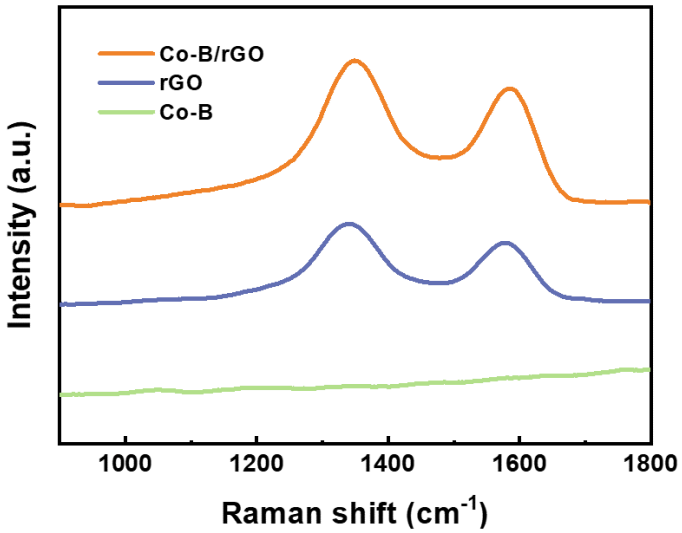

Figure 3-10 Raman spectra of the Co-B/rGO composite, rGO, and Co-B, respectively.

Then XPS spectra were measured to reveal the elemental compositions and bonding modes in the Co-B/rGO composite and blank Co-B, respectively. The XPS spectrum demonstrated that the elements of Co, B, C, and O were co-existent in the Co-B/rGO composite as shown in Figure 3-11(a), The same peak position could be observed in the blank Co-B sample except for the carbon element presented at Figure 3-11(b). Specifically, obtained Co 2p spectra in high-resolution of the Co-B/rGO composite and blank Co-B were presented in Figure 3-11(c), respectively. The peaks at 802.55 eV and 785.93 eV correspond to satellite Co^{2+} [40]. Another peaking positions under 781.48 eV as well as 797.26 eV can be ascribed from Co 2P3/2, Co 2P1/2 in respective. The result means that the element Co exists in a highly oxidized state in the composite [41]. Besides, these two peaks in the Co-B/rGO composite exhibit a positive shift compared to that of blank Co-B (≈1.14 and 1.26 eV, respectively). These positive shifts probably stem from the impacts of the electron density of carbon atoms, implying the interactions from rGO [42]. As core spectrum for B1s presented at Figure 3-11(d), a typical peak at 191.83 eV was found in Co-B/rGO composite and blank Co-B, which could be attributed to the 1s core levels of B^{3+} that is commonly existent in the borate composites [43, 44]. Furthermore, Figure 3-11(e) in the supplementary information presented the C 1s spectrum of Co-B/rGO. These peaking positions under 284.66, 286.12, as well as 288.42 eV displayed in respective, corresponding to the chemical bonding of C=C, C-O, O-C=O as reported on literature [45]. Discussing for oxygen, two main peaks at 531.4 and 533.3 eV in Figure 3-11(f) can be observed, which corresponds with chemical bonding for C=O as well as B-O in respective [46]. At this point, XPS analyses also demonstrated that cobalt borate was introduced on the rGO nanosheets.

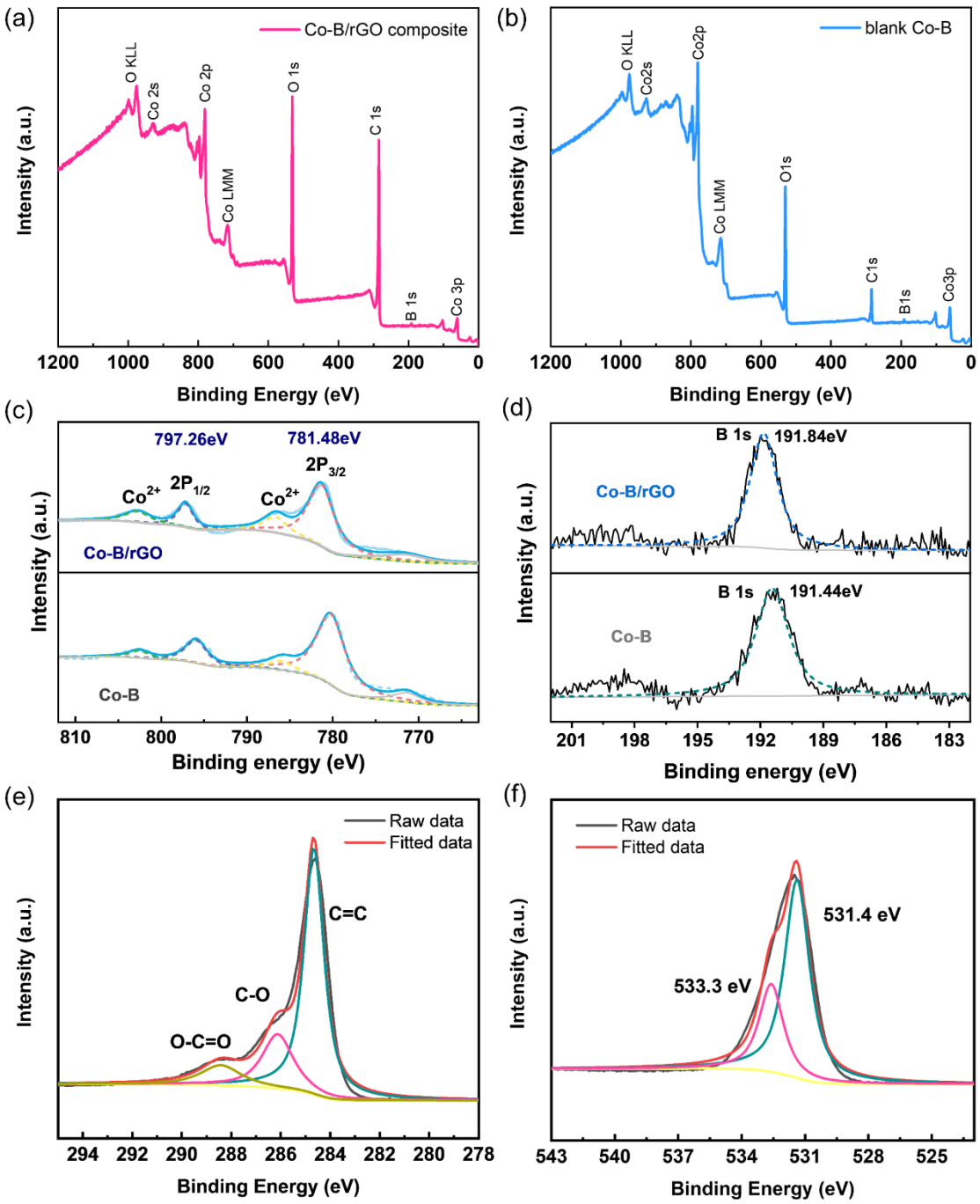

Figure 3-11 XPS survey spectral curves for (a) Co-B/rGO composite, (b) blank Co-B, respectively. The spectra contain characteristic peaks for Co, B, C, and O. XPS spectra of (c) Co 2P and (d) B 1s in Co-B/rGO and blank Co-B. Obtained specific XPS spectral patterns for (e) C 1s of the Co-B/rGO composite. (f) O 1s in the Co-B/rGO composite.

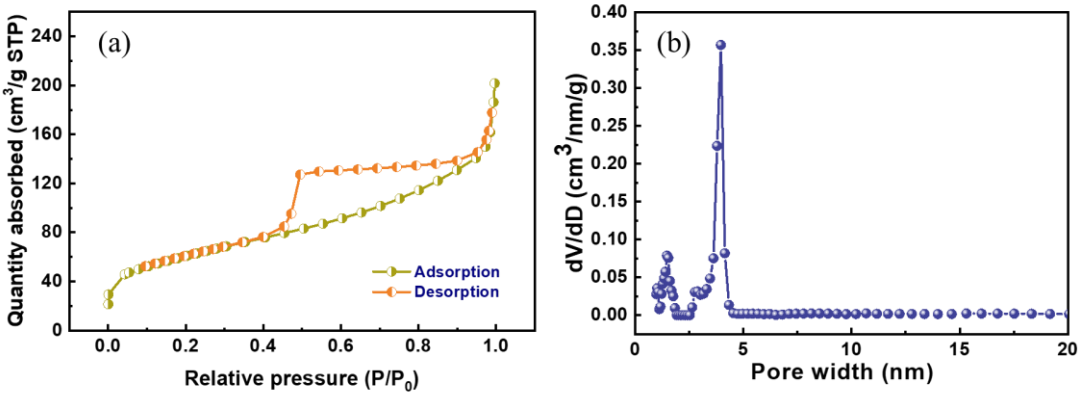

Figure 3-12 (a) Nitrogen adsorption/desorption isotherm, (b) pore size distributions curve for Co-B/rGO composite.

Furthermore, obtained nitrogen adsorption and desorption isotherms for Co-B/rGO composites was presented in Figure 3-12(a), along with the distribution of pore size in Figure 3-12(b). In the medium pressure region, a hysteresis loop could be observed. It means that there are large amounts of small intra-pores in the Co-B/rGO composite. Besides, the pore size distribution curves demonstrated that these mesopores located in majority under the size ranging 2 - 5 nm. Meanwhile, compared to prepared blank cobalt borate (63.2 $m^2 g^{-1}$), evaluated specific surface areas for synthesized Co-B/rGO composites were improved to be 212 $m^2 g^{-1}$. The well-obtained surface area and pore structure provide exposed active sites and favored ions transport. This efficient network structure is beneficial to improve the lithium storage properties when employed as an anode in LICs. The TGA curves of the Co-B and Co-B/rGO composite were shown in Figure 3-13, respectively.

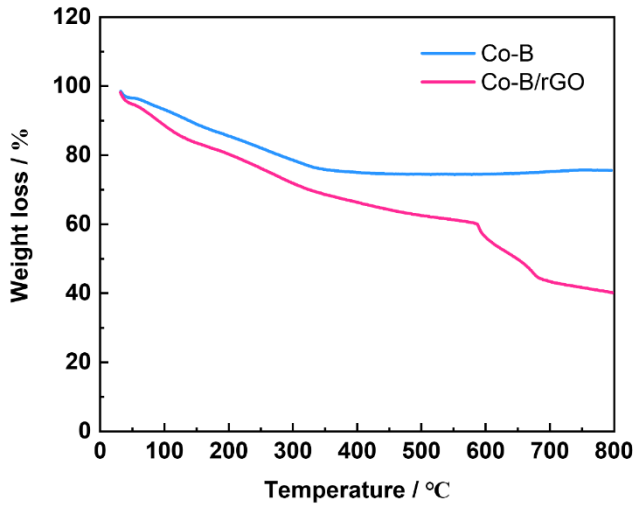

Figure 3-13 Thermogravimetric analysis (TGA) curves of the Co-B and Co-B/rGO composite.

3.3.2 Electrochemical Properties Measured in LIBs Half-cell

To make a comparison between the performance of the materials and devices prepared in this work with traditional ones more clearly, the characterizations along with electrochemical performance for Co-B/rGO composites were conducted firstly being negative electrode for lithium-ion batteries half-cell. Then, LIC full cell was assembled and investigated to discuss electrochemical performance.

At first, lithium storage properties of the blank cobalt borate, rGO, and the Co-B/rGO composite electrodes were studied using cyclic voltammetry (CV). Figure 3-14 presents obtained CV curves for (a) Co-B/rGO composite, (b) blank Co-B, and (c) rGO electrode at the same scan rate under 0.1 mV s^{-1}, respectively. As presented, cathodic peaking positions located under 0.76 as well as 0.08 V for Co-B/rGO composite. The peak at 0.76 V was a joint result from Co-B and rGO, while the peak at 0.08 V originated from rGO. Compared to that of rGO, two new peaking locations (under 1.3, 2.2 V in respectively) appeared in anodic processes. They were ascribed to the redox reactions with cobalt borate nanoparticles, well corresponding to the CV of blank cobalt borate electrode.

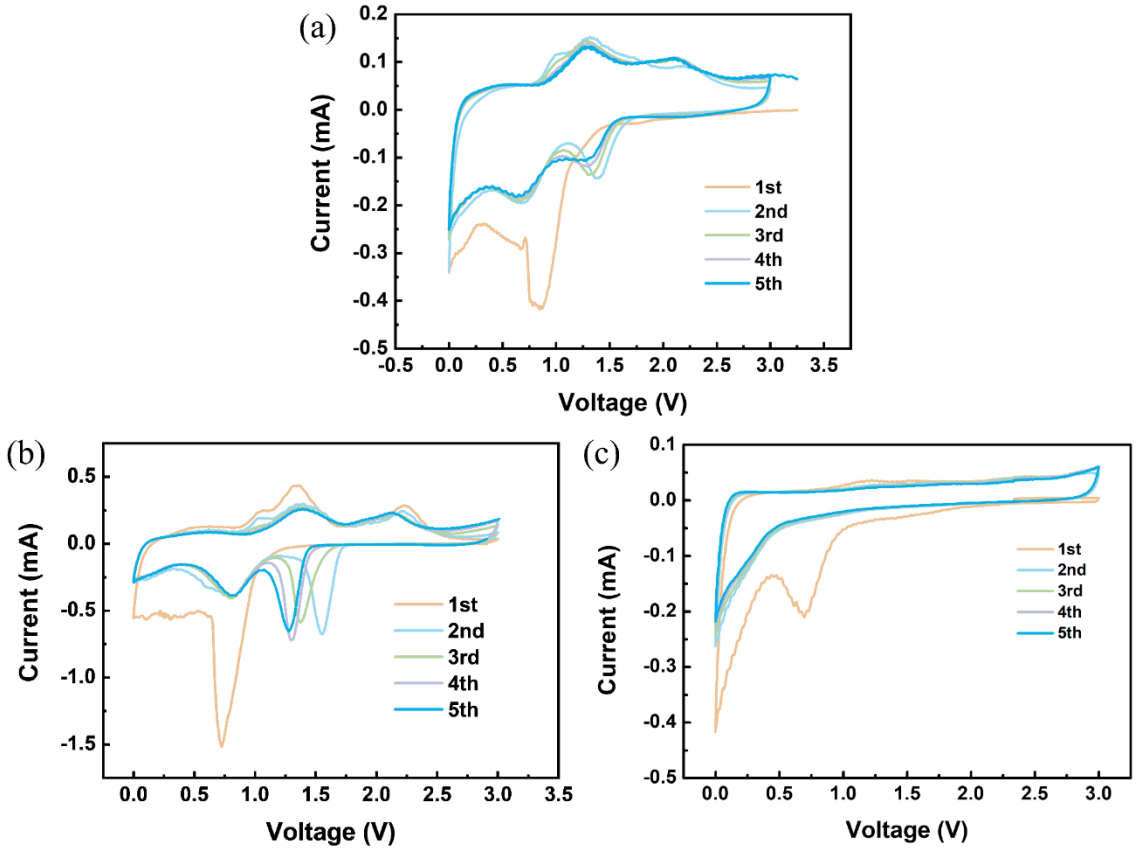

Figure 3-14 CV curves of (a) Co-B/rGO composite, (b) blank Co-B, and (c) rGO electrode at 0.1 mV s^{-1}.

Furthermore, the galvanostatic discharging/charging was measured under 50 mA g^{-1}. For the blank rGO electrode in Figure 3-15(a), the first discharge capacity 1643 mAh g^{-1}, along with charging capacities around 630.0 mAh g^{-1}. The low Coulombic efficiency (CE) for rGO mainly owes to the capacity loss that occurred in the forming process of solid electrolyte interphase (SEI). In contrast, the CE was improved to 70% in the Co-B/rGO composite, with the discharging as well as charging capacities being 1477, 1035 mAh g^{-1} given as Figure 3-15(b).

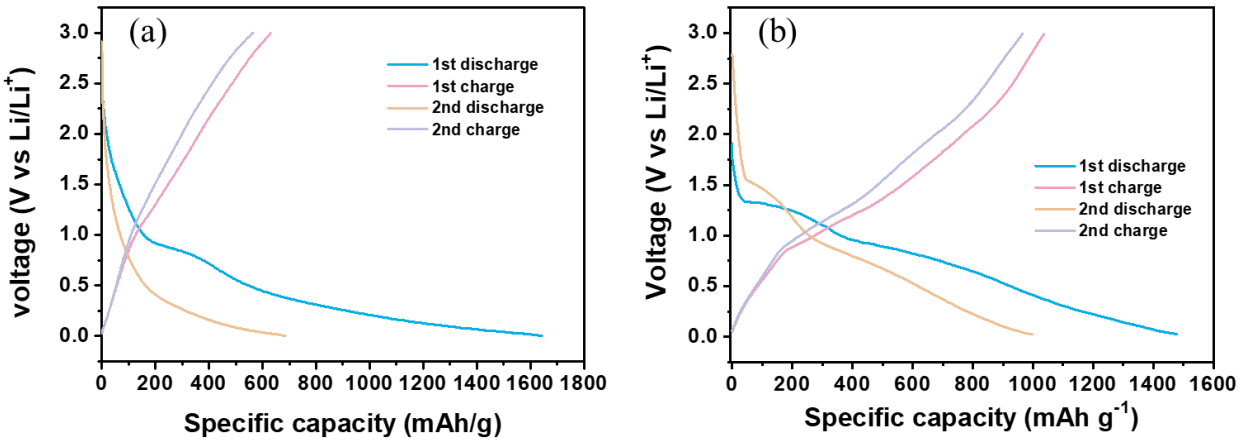

Figure 3-15 Obtained charging-discharging curves for (a) blank rGO, and (b) Co-B/rGO at 50 mA g^{-1}.

In order to investigate more electrochemical performance for as-prepared Co-B/rGO composite, blank Co-B, as well as rGO, we show the rate capabilities in Figure 3-16(a). The Co-B/rGO composite delivers specific capacities with a maximum value of 970 mAh g^{-1} under 50 mA g^{-1}, whereas in comparison corresponding value of blank Co-B and rGO is 610 mAh g^{-1} and 490 mAh g^{-1}, respectively. Furthermore, when the operating current density increased to 5000 mA g^{-1}, the capacities with value of 310 mAh g^{-1} was achieved in Co-B/rGO, approximately 3.5 times higher than that of rGO. The EIS curves of Co-B/rGO, blank Co-B, and rGO were performed as Figure 3-16(b). The semicircle diameter of the Co-B/rGO composites locating within large frequential regions was significantly lower compared to that for blank rGO, indicating the Co-B/rGO electrode possesses a lower charge transfer resistance due to decoration with cobalt borate nanoparticles. This can be explained that cobalt borate nanoparticles act as an effective electron transfer bridge between rGO nanosheets, which endows the Co-B/rGO composite with increased electronic conductivity. Figure 3-16(c) depicted the discharge-charge cycling stability of the Co-B/rGO composite, compared to blank Co-B and rGO. The Co-

B/rGO composite delivers 600 mAh g^{-1} with completion of cycling 600 times under the operating current density around 1000 mA g^{-1}, which is 1.5 magnification larger in comparison with that for blank rGO.

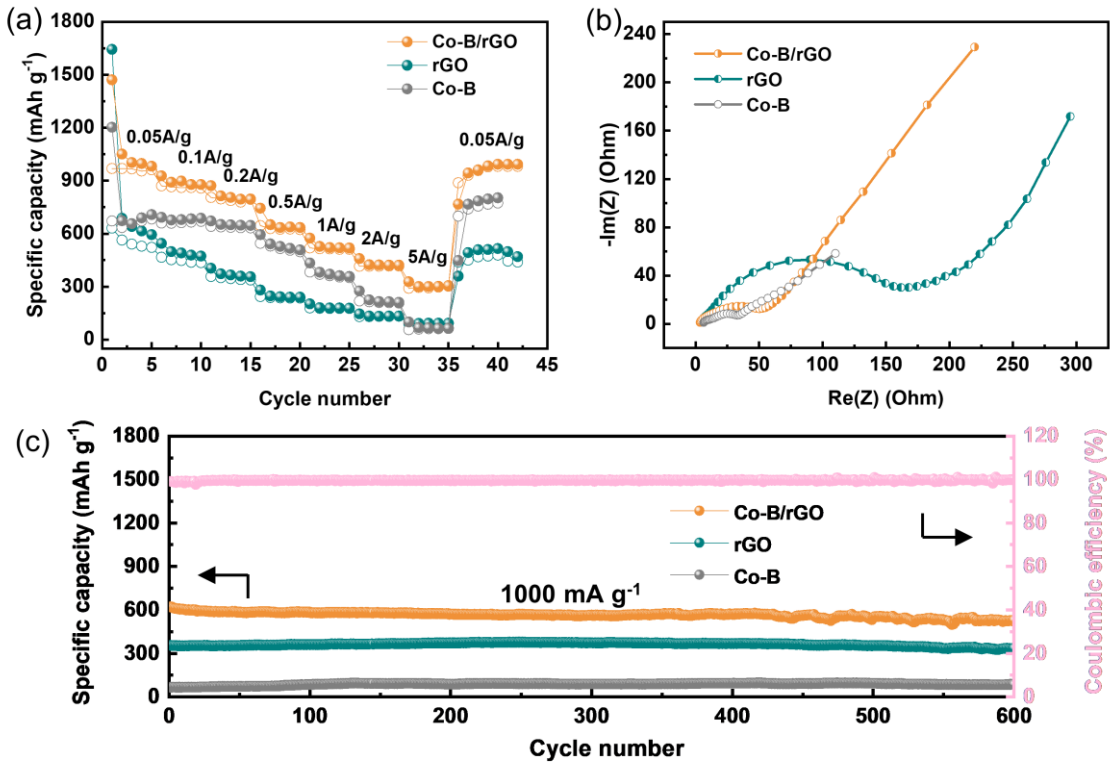

Figure 3-16 (a) Rate performance, (b) Nyquist plots, and (c) cycling performance of cells with Co-B/rGO, blank rGO, and Co-B electrodes, respectively.

When the LIBs half-cell worked for 900 cycling numbers under 500 mA g^{-1}, observed reversible capacities for Co-B/rGO composites still retained 85% of the initial capacities presented at Figure 3-17. In contrast to the amorphous state, crystallized cobalt borate nanoparticles in the composite with the size of 5-20 nm provided a large charge transfer interfacial areas amid active materials in electrodes and electrolyte. Secondly, the crystallized nanoparticles along with the mesoporous architecture in the composite are beneficial for fast Li^+ transport when served as the anode. Moreover, fewer disorders and defects with a smaller particle size are also beneficial for fast electron transport and structural stability of the electrode in cycling.

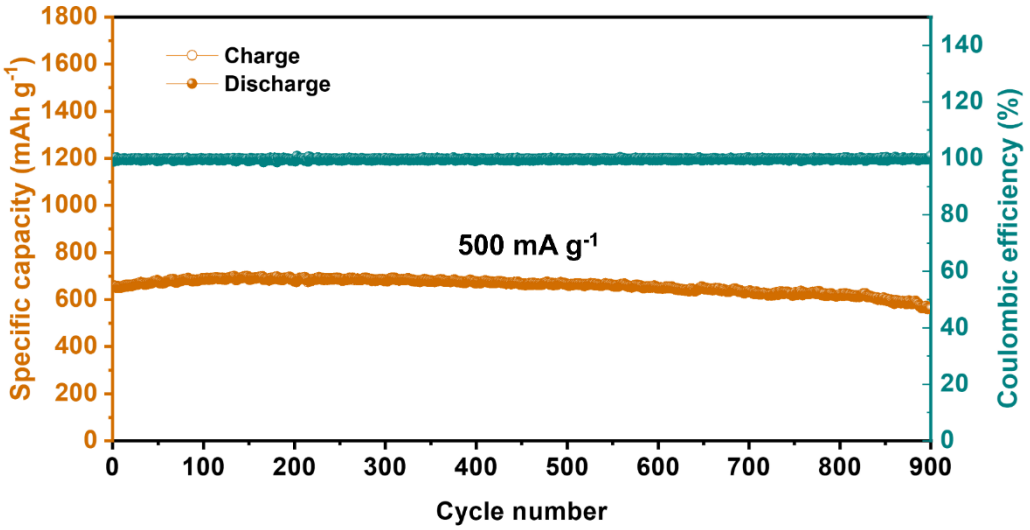

Figure 3-17 Long-term cycling stabilities of Co-B/rGO electrode in LIBs half-cell when operating current density set as 500 mA g^{-1}.

Kinetics analysis for Co-B/rGO for Li^+ storage was conducted via CV measurements using different scan rates, details were given in Figure 3-18(a). The relationship between current *i* along with scan rate *v* conform below formula 3-3:

$$i = av^b \qquad (3\text{-}3)$$

In which, *a* is a constant while *b* varies from 0.5 to 1.0. The capacitive behavior contributes most to the current when numerical quantity of b tends closely towards 1.0. Otherwise, these whole processes are controlled by diffusion [47]. As presented in Figure 3-18(b), the b values in reduction and oxidation were calculated from the slope as 0.799 and 0.815, respectively, indicating the charge-discharge process was controlled by capacitive contribution. In detail, the capacitive-controlled and diffusion-controlled parts can be explored based on the following equation 3-4 [48, 49].

$$i(V) = k_1 v + k_2 v^{1/2} \qquad (3\text{-}4)$$

In which, k_1 along with k_2 represent invariable values. When operating scan rate was 2 mV s^{-1}, evaluated detailed percentage of component controlled by capacitance in the electrode of Co-B/rGO composite was calculated as high as 78.4% shown in Figure 3-18(c).

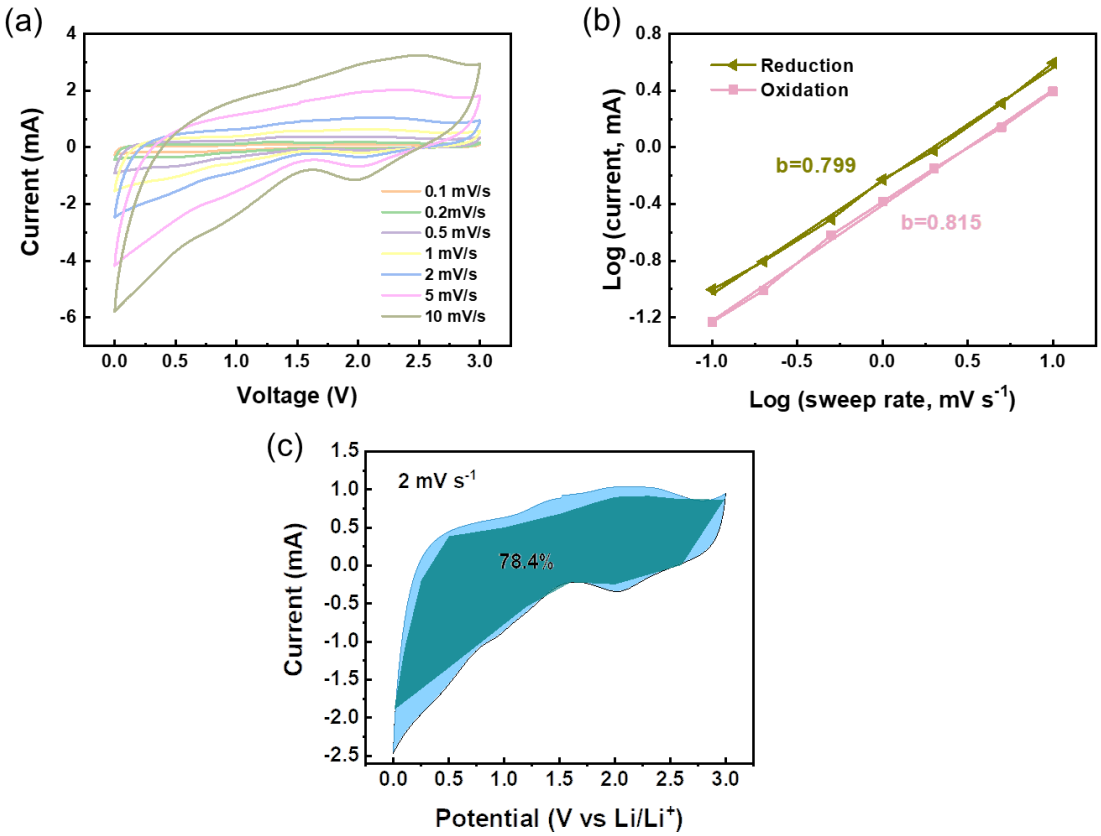

Figure 3-18 (a) CV patterns for Co-B/rGO anode in LIBs half-cell under different sweep rate ranging 0.1 - 10 mV s^{-1}. (b) The b numerical quantities evaluation for peaking positions under scan rate ranging 0.1 - 10 mV s^{-1}. (c) Separating evaluation for component dominated by capacitance under 2 mV s^{-1}.

3.3.3 Co-B/rGO Composite as the Anode in LIC Full cell

Considering the structural and electrochemical merits of the Co-B/rGO composite compared to blank rGO, LIC full cell was fabricated by conjoining the pre-lithiated Co-B/rGO composite as anode and rGO as a cathode that illustrated in Figure 3-19(a). The CV of the Co-B/rGO LIC was measured from 0 to 4.3 V, indicating a large operating voltage window shown in Figure 3-19(b). The CV curve of Co-B/rGO LIC still shows quasi-rectangular characteristics without obvious distortion under large sweep rate with 200 mV s^{-1}. It implies that the Co-B/rGO LIC possesses an excellent capacitive performance. The galvanostatic charging-discharging patterns along with rate behaviors of Co-B/rGO LIC were presented at Figure 3-19(c) as well as (d), respectively. Obtained specific capacitance exhibited a decreasing trend at higher current densities. This is explained that only the boundary layer on electrode materials participated during electrochemical reactions under large operating currents. Maximum specific capacitance reached 202 F g^{-1} under 50 mA g^{-1}, in contrast the capacitance can only reach 145 F g^{-1} when blank rGO was used as the anode in LIC as a reference.

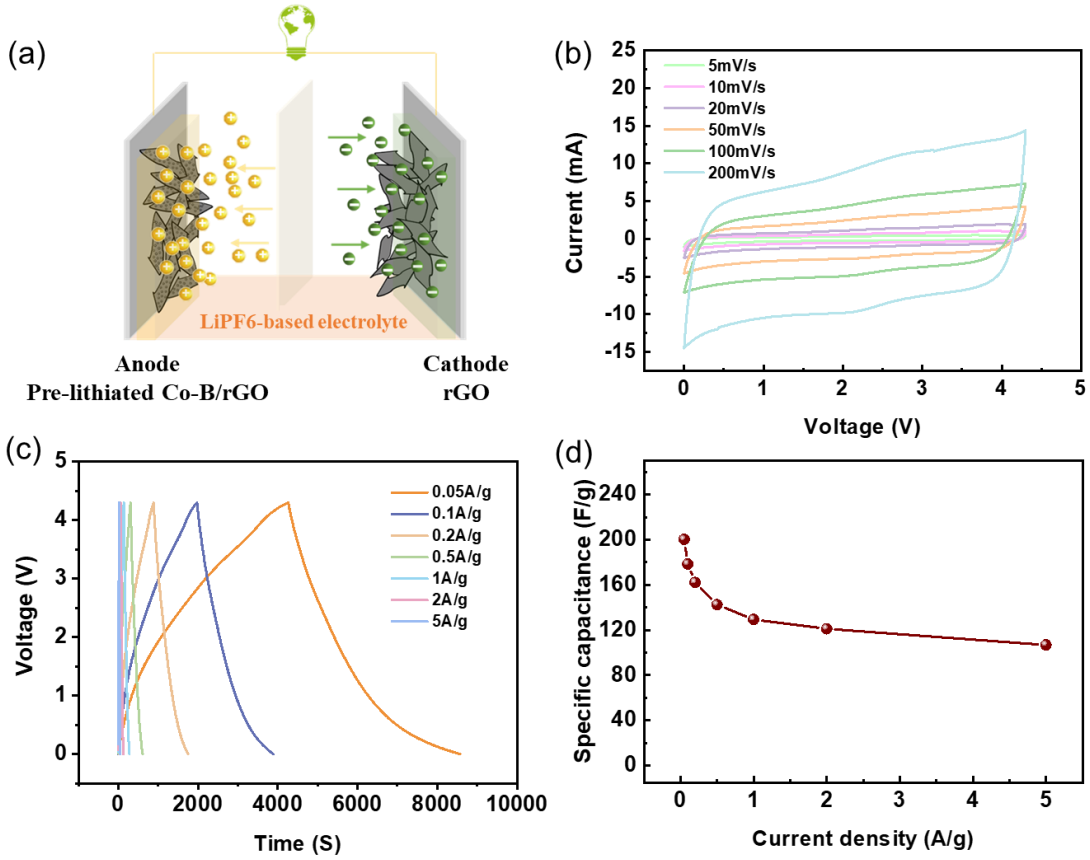

Figure 3-19 (a) Diagram of the Co-B/rGO LIC full cell. (b) CV of the Co-B/rGO LICs under various sweep rates. (c) Galvanostatic charging/discharging. (d) Rate performance for the Co-B/rGO LIC.

Obtained energy-power densities for Co-B/rGO LIC full cells were evaluated as the Ragone plot in Figure 3-20(a). The LIC full-cell based on the Co-B/rGO composite as an anode exhibited an energy density around 128.6 Wh kg^{-1} under the power density in 107.5 W kg^{-1}. When the power densities increased to be 10300 W kg^{-1}, an energy density around 63 Wh kg^{-1} was achieved. Furthermore, the Co-B/rGO LIC full-cell exhibited remarkable cycling stabilities exhibiting a capacitance possession of 75% with completion of 2000 cycling numbers under operating currents in 2000 mA g^{-1}. Furthermore, the full cells show excellent Coulombic efficiencies around 100% as displayed in Figure 3-20(b), implying good electrochemical performance.

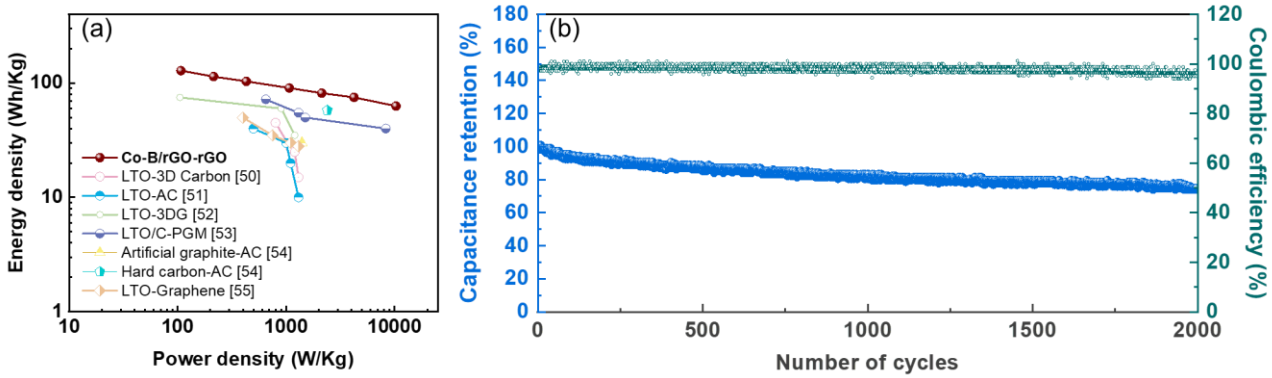

Figure 3-20 (a) Ragone plot of the Co-B/rGO LIC full-cell and reference [50-55]. (b) Cycling performance of the Co-B/rGO LIC full-cell at 2000 mA g^{-1}.

In the Co-B/rGO composite we designed, crystallized cobalt borate nanoparticles not only work as the spacer to alleviate the aggregation of rGO nanosheets but also function as an effective electron transfer bridge in the cross-plane direction to improve the electrical conductivity. As a result, electron transport kinetics can be improved. Meanwhile, these crystallized cobalt borate nanoparticles can act as the substance to make more active sites available for lithium storage. Besides, the sandwich-like structure can constitute a short path for the diffusion of Li^+, along with a large charge transfer interface between the active materials and electrolyte. Benefiting from the synergetic effects, the as-designed Co-B/rGO composite displays excellent electrochemical performance as an anode material in LICs.

3.4 Conclusions

To summarize, this part introduced an efficient in-situ grow mode to prepare the reduced graphene oxide compositing with crystallized cobalt borate nanoparticles. The crystallized cobalt borate nanoparticles with the size of 5 to 20 nm distributed on the surface of rGO nanosheets uniformly, which alleviates rGO sheets from aggregation and forms a network structure. Thanks to the unique sandwich-like structure and efficiently conducting network, the Co-B/rGO composite shows a good rate behavior (970 mAh g^{-1} under the current density around 50 mA g^{-1}, along with 310 mAh g^{-1} when operating current density increased to be 5000 mA g^{-1}), as well as good cycling stabilities (600 mAh g^{-1} under 1000 mA g^{-1} completing 600 cycling numbers) when measured as the anode in the LIBs half-cell. Considering the structural and electrochemical merits of the Co-B/rGO composite, a lithium-ion capacitor full-cell device was assembled based on the Co-B/rGO composite being anode electrode along with rGO being cathode. The obtained LICs devices shows steady cycling behavior exhibiting capacitance possession in 75% completing 2000 cycling numbers under 2000 mA g^{-1}, as

well as high energy densities of 128.6 Wh kg^{-1} under power densities around 107.5 W kg^{-1}, as well as 63 Wh kg^{-1} under a power density around 10300 W kg^{-1}. It demonstrates that the Co-B/rGO composite could be employed being competitive anodes for the lithium-ion capacitor, which propels the realization of energy-storage systems with high-performance.

References

[1] J. Li, J. Tang, J. Yuan, K. Zhang, Q. Shao, Y. Sun, L.-C. Qin, Interactions between graphene and ionic liquid electrolyte in supercapacitors, Electrochimica Acta, 197 (2016) 84-91.

[2] F. Zhang, J. Tang, N. Shinya, L.-C. Qin, Hybrid graphene electrodes for supercapacitors of high energy density, Chemical Physics Letters, 584 (2013) 124-129.

[3] Q. Shao, J. Tang, Y. Lin, F. Zhang, J. Yuan, H. Zhang, N. Shinya, L.-C. Qin, Synthesis and characterization of graphene hollow spheres for application in supercapacitors, Journal of Materials Chemistry A, 1 (2013) 15423-15428.

[4] J. Li, J. Tang, J. Yuan, K. Zhang, X. Yu, Y. Sun, H. Zhang, L.-C. Qin, Porous carbon nanotube/graphene composites for high-performance supercapacitors, Chemical Physics Letters, 693 (2018) 60-65.

[5] X.L. Yu, J. Tang, K. Terabe, T. Sasaki, R.S. Gao, Y. Ito, K. Nakura, K. Asano, M.A. Suzuki, Fabrication of graphene/MoS_2 alternately stacked structure for enhanced lithium storage, Mater Chem Phys, 239 (2020) 121987.

[6] V. Aravindan, Y.S. Lee, S. Madhavi, Research progress on negative electrodes for practical Li-ion batteries: beyond carbonaceous anodes, Advanced Energy Materials, 5 (2015) 1402225.

[7] P. Simon, Y. Gogotsi, B. Dunn, Where do batteries end and supercapacitors begin?, Science, 343 (2014) 1210-1211.

[8] H. Wang, C. Zhu, D. Chao, Q. Yan, H.J. Fan, Nonaqueous hybrid lithium-ion and sodium-ion capacitors, Advanced materials, 29 (2017) 1702093.

[9] A. Jagadale, X. Zhou, R. Xiong, D.P. Dubal, J. Xu, S. Yang, Lithium ion capacitors (LICs): Development of the materials, Energy Storage Mater, 19 (2019) 314-329.

[10] G. Zhu, L. Ma, H. Lin, P. Zhao, L. Wang, Y. Hu, R. Chen, T. Chen, Y. Wang, Z. Tie, Z. Jin, High-performance Li-ion capacitor based on black-TiO_{2-x}/graphene aerogel anode and biomass-derived microporous carbon cathode, Nano Research, 12 (2019) 1713-1719.

[11] F. Sun, X. Liu, H.B. Wu, L. Wang, J. Gao, H. Li, Y. Lu, In situ high-level nitrogen doping into carbon nanospheres and boosting of capacitive charge storage in both anode and cathode for a high-energy 4.5 V full-carbon lithium-ion capacitor, Nano letters, 18 (2018) 3368-3376.

[12] X. Yu, C. Zhan, R. Lv, Y. Bai, Y. Lin, Z.-H. Huang, W. Shen, X. Qiu, F. Kang, Ultrahigh-rate and high-density lithium-ion capacitors through hybriding nitrogen-enriched hierarchical porous carbon cathode with prelithiated microcrystalline graphite anode, Nano Energy, 15 (2015) 43-53.

[13] C. Han, H. Li, R. Shi, L. Xu, J. Li, F. Kang, B. Li, Nanostructured Anode Materials for Non-aqueous Lithium Ion Hybrid Capacitors, Energy & Environmental Materials, 1 (2018) 75-87.

[14] S.R. Sivakkumar, J. Nerkar, A. Pandolfo, Rate capability of graphite materials as negative electrodes in lithium-ion capacitors, Electrochimica Acta, 55 (2010) 3330-3335.

[15] H. Wang, Z. Xu, Z. Li, K. Cui, J. Ding, A. Kohandehghan, X. Tan, B. Zahiri, B.C. Olsen, C.M. Holt, Hybrid device employing three-dimensional arrays of MnO in carbon nanosheets bridges battery–supercapacitor divide, Nano letters, 14 (2014) 1987-1994.

[16] L.F. Que, F.D. Yu, Z.B. Wang, D.M. Gu, Pseudocapacitance of TiO_{2-x}/CNT Anodes for High-Performance Quasi-Solid-State Li-Ion and Na-Ion Capacitors, Small, 14 (2018) e1704508.

[17] R. Wang, J. Lang, P. Zhang, Z. Lin, X. Yan, Fast and large lithium storage in 3D porous VN nanowires–Graphene composite as a superior anode toward high-performance hybrid Supercapacitors, Advanced Functional Materials, 25 (2015) 2270-2278.

[18] J. Zhu, A. Liu, D. Wang, Study on the synergistic lithium storage performance of Sn/graphene nanocomposites via quantum chemical calculations and experiments, Applied Surface Science, 416 (2017) 751-756.

[19] J. Zhu, X. Ding, A facile one–pot synthesis of Sn/graphite/graphene nanocomposites as anode materials for lithium–ion batteries, Journal of Alloys and Compounds, 809 (2019) 151870.

[20] J. Zhu, Z. Zhang, X. Ding, G. Hu, Preparation of SnS/reduced graphene oxide@ Cu nanocomposite with high reversible lithium storage, Materials Letters, 264 (2020) 127378.

[21] Y. Ma, H. Chang, M. Zhang, Y. Chen, Graphene-based materials for lithium-ion hybrid supercapacitors, Advanced Materials, 27 (2015) 5296-5308.

[22] H. Wang, Y. Zhang, H. Ang, Y. Zhang, H.T. Tan, Y. Zhang, Y. Guo, J.B. Franklin, X.L. Wu, M. Srinivasan, A high-energy lithium-ion capacitor by integration of a 3D interconnected titanium carbide nanoparticle chain anode with a pyridine-derived porous nitrogen-doped carbon cathode, Advanced Functional Materials, 26 (2016) 3082-3093.

[23] Y. Sun, J. Tang, K. Zhang, J. Yuan, J. Li, D.-M. Zhu, K. Ozawa, L.-C. Qin, Comparison of reduction products from graphite oxide and graphene oxide for anode applications in lithium-ion batteries and sodium-ion batteries, Nanoscale, 9 (2017) 2585-2595.

[24] X. Jin, K. Adpakpang, I.Y. Kim, S.M. Oh, N.-S. Lee, S.-J. Hwang, An effective way to optimize the functionality of graphene-based nanocomposite: Use of the colloidal mixture of graphene and inorganic nanosheets, Scientific reports, 5 (2015) 11057.

[25] W. Tu, Y. Zhou, Q. Liu, S. Yan, S. Bao, X. Wang, M. Xiao, Z. Zou, An In Situ Simultaneous Reduction-Hydrolysis Technique for Fabrication of TiO_2-Graphene 2D Sandwich-Like Hybrid Nanosheets: Graphene-Promoted Selectivity of Photocatalytic-Driven Hydrogenation and Coupling of CO_2 into Methane and Ethane, Advanced Functional Materials, 23 (2013) 1743-1749.

[26] X.J. Zhu, Y.W. Zhu, S. Murali, M.D. Stollers, R.S. Ruoff, Nanostructured Reduced Graphene Oxide/Fe_2O_3 Composite As a High-Performance Anode Material for Lithium Ion Batteries, Acs Nano, 5 (2011) 3333-3338.

[27] J. Zang, H. Qian, Z. Wei, Y. Cao, M. Zheng, Q. Dong, Reduced graphene oxide supported MnO nanoparticles with excellent lithium storage performance, Electrochimica Acta, 118 (2014) 112-117.

[28] Q. Cheng, J. Tang, J. Ma, H. Zhang, N. Shinya, L.C. Qin, Graphene and nanostructured MnO_2 composite electrodes for supercapacitors, Carbon, 49 (2011) 2917-2925.

[29] Y. Sun, J. Tang, F. Qin, J. Yuan, K. Zhang, J. Li, D.-M. Zhu, L.-C. Qin, Hybrid lithium-ion capacitors with asymmetric graphene electrodes, Journal of Materials Chemistry A, 5 (2017) 13601-13609.

[30] Q. Cheng, J. Tang, J. Ma, H. Zhang, N. Shinya, L.-C. Qin, Graphene and carbon nanotube composite electrodes for supercapacitors with ultra-high energy density, Physical Chemistry Chemical Physics, 13 (2011) 17615-17624.

[31] Q. Shao, J. Tang, Y. Lin, J. Li, F. Qin, J. Yuan, L.-C. Qin, Carbon nanotube spaced graphene aerogels with enhanced capacitance in aqueous and ionic liquid electrolytes, Journal of Power Sources, 278 (2015) 751-759.

[32] Q. Shao, J. Tang, Y. Sun, J. Li, K. Zhang, J. Yuan, D.M. Zhu, L.C. Qin, Unique interconnected graphene/SnO_2 nanoparticle spherical multilayers for lithium-ion battery applications, Nanoscale, 9 (2017) 4439-4444.

[33] X.X. Shi, X.J. Liu, L.J. Yuan, The electrochemical property of cobalt borate as a novel anode material for lithium-ion battery, Advanced Materials Research, Trans Tech Publ, 236 (2011) 876-879.

[34] D. Wang, J. Zhou, J. Li, X. Jiang, Y. Wang, F. Gao, Cobalt-boron nanoparticles anchored on graphene as anode of lithium ion batteries, Chemical Engineering Journal, 360 (2019) 271-279.

[35] P. Chen, K. Xu, T. Zhou, Y. Tong, J. Wu, H. Cheng, X. Lu, H. Ding, C. Wu, Y. Xie, Strong-coupled cobalt borate nanosheets/graphene hybrid as electrocatalyst for water oxidation under both alkaline and neutral conditions, Angewandte Chemie International Edition, 55 (2016) 2488-2492.

[36] J. Ma, X. Zhang, K. Chen, G. Li, X. Han, Morphology-controlled synthesis of hematite hierarchical structures and their lithium storage performances, Journal of Materials Chemistry A, 1 (2013) 5545-5553.

[37] W. Dong, Y. Zhao, X. Wang, X. Yuan, K. Bu, C. Dong, R. Wang, F. Huang, Boron embedded in metal iron matrix as a novel anode material of excellent performance, Advanced Materials, 30 (2018) 1801409.

[38] W.S. Hummers Jr, R.E. Offeman, Preparation of graphitic oxide, Journal of the american chemical society, 80 (1958) 1339-1339.

[39] K. Krishnamoorthy, M. Veerapandian, K. Yun, S.J. Kim, The chemical and structural analysis of graphene oxide with different degrees of oxidation, Carbon, 53 (2013) 38-49.

[40] X. Ren, R. Ge, Y. Zhang, D. Liu, D. Wu, X. Sun, B. Du, Q. Wei, Cobalt–borate nanowire array as a high-performance catalyst for oxygen evolution reaction in near-neutral media, Journal of Materials Chemistry A, 5 (2017) 7291-7294.

[41] M.W. Kanan, D.G. Nocera, In situ formation of an oxygen-evolving catalyst in neutral water containing phosphate and Co^{2+}, Science, 321 (2008) 1072-1075.

[42] E.A. Turhan, S.V.K. Nune, E. Ülker, U. Şahin, Y. Dede, F. Karadas, Water Oxidation Electrocatalysis with a Cobalt-Borate-Based Hybrid System under Neutral Conditions, Chemistry–A European Journal, 24 (2018) 10372-10382.

[43] X. Ji, L. Cui, D. Liu, S. Hao, J. Liu, F. Qu, Y. Ma, G. Du, A.M. Asiri, X. Sun, A nickel-borate nanoarray: a highly active 3D oxygen-evolving catalyst electrode operating in near-neutral water, Chemical Communications, 53 (2017) 3070-3073.

[44] C. He, X. Wu, Z. He, Amorphous nickel-based thin film as a Janus electrocatalyst for water splitting, The Journal of Physical Chemistry C, 118 (2014) 4578-4584.

[45] J. Gao, X. Wang, Y. Zhang, J. Liu, Q. Lu, M. Liu, Boron-doped ordered mesoporous carbons for the application of supercapacitors, Electrochimica Acta, 207 (2016) 266-274.

[46] Z.-H. Sheng, H.-L. Gao, W.-J. Bao, F.-B. Wang, X.-H. Xia, Synthesis of boron doped graphene for oxygen reduction reaction in fuel cells, Journal of Materials Chemistry, 22 (2012) 390-395.

[47] V. Augustyn, J. Come, M.A. Lowe, J.W. Kim, P.L. Taberna, S.H. Tolbert, H.D. Abruna, P. Simon, B. Dunn, High-rate electrochemical energy storage through Li^+ intercalation pseudocapacitance, Nature Materials, 12 (2013) 518-522.

[48] C. Yang, J. Feng, F. Lv, J. Zhou, C. Lin, K. Wang, Y. Zhang, Y. Yang, W. Wang, J. Li, S. Guo, Metallic Graphene-Like VSe_2 Ultrathin Nanosheets: Superior Potassium-Ion Storage and Their Working Mechanism, Adv Mater, 30 (2018) e1800036.

[49] H.S. Kim, J.B. Cook, H. Lin, J.S. Ko, S.H. Tolbert, V. Ozolins, B. Dunn, Oxygen vacancies enhance pseudocapacitive charge storage properties of MoO_{3-x}, Nat Mater, 16 (2017) 454-460.

[50] A. Banerjee, K.K. Upadhyay, D. Puthusseri, V. Aravindan, S. Madhavi, S. Ogale, MOF-derived crumpled-sheet-assembled perforated carbon cuboids as highly effective cathode active materials for ultra-high energy

density Li-ion hybrid electrochemical capacitors (Li-HECs), Nanoscale, 6 (2014) 4387-4394.

[51] J.H. Lee, W.H. Shin, M.-H. Ryou, J.K. Jin, J. Kim, J.W. Choi, Functionalized graphene for high performance lithium ion capacitors, ChemSusChem, 5 (2012) 2328-2333.

[52] S. Dsoke, B. Fuchs, E. Gucciardi, M. Wohlfahrt-Mehrens, The importance of the electrode mass ratio in a Li-ion capacitor based on activated carbon and $Li_4Ti_5O_{12}$, J Power Sources, 282 (2015) 385-393.

[53] K. Leng, F. Zhang, L. Zhang, T. Zhang, Y. Wu, Y. Lu, Y. Huang, Y. Chen, Graphene-based Li-ion hybrid supercapacitors with ultrahigh performance, Nano Research, 6 (2013) 581-592.

[54] L. Ye, Q.H. Liang, Y. Lei, X.L. Yu, C.P. Han, W.C. Shen, Z.H. Huang, F.Y. Kang, Q.H. Yang, A high performance Li-ion capacitor constructed with $Li_4Ti_5O_{12}$/C hybrid and porous graphene macroform, J Power Sources, 282 (2015) 174-178.

[55] J.-H. Kim, J.-S. Kim, Y.-G. Lim, J.-G. Lee, Y.-J. Kim, Effect of carbon types on the electrochemical properties of negative electrodes for Li-ion capacitors, Journal of Power Sources, 196 (2011) 10490-10495.

Chapter 4

Experimental Dispersion of the Third-order Optical Susceptibility of Graphene Oxide

4.1 Introduction

The utilization of laser technologies has greatly boosted the development of precise materials processing [1], medicine and biology [2], security detection [3], and other fields. However, the ubiquitous applications bring on some undesired laser-induced damages to the detectors, imaging devices, and sensors, even worse some irreversible physical damages to human eyes. Therefore, the use of high-intensity laser beams makes safety devices greatly necessary and challenging to avoid potential damages from accidental exposures to laser radiation [4]. Consequently, optical limiters, which are used to protect sensitive photonic instruments and human eyes from harmful effects induced by laser, have attracted enormous attention in the past few decades. The efficient optical limiting (OL) materials are based on high linear transmittance, large nonlinearities, and broadband spectral response [5]. For the sake of above, many OL materials have been explored considerably to meet these demands, such as fullerenes derivatives [6, 7], metallic nanomaterials (zinc ferrites nanoparticles [8], gold clusters [9]). However, these materials exhibit OL behaviors only at certain wavelengths, which remains a serious obstacle to provide reliable protection over a wide spectral range in practical applications. To address these challenges, graphene oxide (GO), with broadband nonlinear optical (NLO) properties over visible regions, emerges as a promising material for the OL devices [10]. In addition, GO is hydrophilic with good dissolvent capability in the water, ethanol, and other solvents [11], leading to good workability in the manufacturing process. Moreover, because of the introduction of hydroxyl or epoxy groups in the oxidization process, GO can interact with various organic and inorganic substances and is highly compatible with a variety of additives [12]. These advantageous properties make GO a study focus in the filed of third-order nonlinear

optics.

In recent years, the NLO properties of GO have been extensively studied. For instance, the OL actions of few-layered GO dispersed in an organic solvent were observed by Z-scan at 532 nm [13]. GO nanosheets dispersed in the de-ionized water were also reported to show broadband NLO and OL properties at 1064 nm [14]. In addition, tunable OL properties of GO in ethanol solution were studied at 1550 nm [15]. However, these efforts have focused on the dispersions in certain solvents, and the OL properties of GO measured by the laser at 532, 1064, and 1550 nm. To broaden the applicability of GO in practical applications, it is necessary to investigate solid films and extend the operating wavelength to a wider range. In moving towards the application of GO in optical limiters over visible regions, the third-order optical susceptibilities $\chi^{(3)}$ are crucial parameter that needs to be evaluated. Since the complex $\chi^{(3)}$ of GO has a strong relationship with its nonlinear refraction and absorption, the imaginary part directly verbalizes the information about the saturable absorption (SA) along with reverse saturable absorption (RSA), which are important bases for the OL applications. Meanwhile, owing to the electronic transitions, the NLO properties of GO show wavelength-dependent characteristics [16]. Unfortunately, previous literature on $\chi^{(3)}$ for GO have been carried out only at some discrete wavelengths, such as at 532 nm reported by Khanzadeh et al. [17] and Biswas et al. [18], or at 1064 nm investigated by Liaros et al. [19]. In consequence, the dispersion of $\chi^{(3)}$ in GO is deserved to be determined experimentally in the continuous visible region.

In the present work, femtosecond pump and probe spectroscopy was used to investigate the nonlinear transmission changes of the GO/PVA composite film over the continuous wavelengths ranging from 450 to 750 nm, and the $\chi^{(3)}$ dispersion of GO was experimentally determined by combining with the spectroscopic ellipsometry (SE). We identified that the linear optical properties of GO show a flat dispersion over visible regions. In contrast, the nonlinear optical response in GO exhibits saturable absorption (SA) in the range of short wavelength and RSA at long wavelength. These results propel the application of GO in the broadband OL devices based on the RSA. Furthermore, it allows us to make a comparison with the graphene fabricated by the chemical vapor deposition (CVD) method, where the electronic structure is mainly established by sp^2 hybridizations. Physical identification of carrier dynamics that origin from sp^2 domains and sp^3 carbons provides us opportunities to tailor the NLO properties and OL performance of GO.

4.2 Experimental Section

4.2.1 Synthesis of Graphene Oxide (GO)

GO samples were synthesized as discussed in modified Hummers methods in previously reported [20]. All chemicals were purchased and used without further purification. In synthesis process, graphite flake powders (500 mg) and $NaNO_3$ (250 mg) were mixed firstly in a cold and concentrated H_2SO_4 (50 mL) under magnetic stirring. Then, 1500 mg $KMnO_4$ powders were put to the mixture with an ice-water protection under stirring. After stirring for 48 h, de-ionized (DI) water (100 mL) followed by H_2O_2 (30 mL) solution was gradually dropped into above beaker until a yellow suspension was obtained. Finally, the solution was washed several times through centrifugation using 1 M HCl solution followed by DI respectively before PH in 7.

4.2.2 Fabrication of the GO/PVA Composite Thin Film

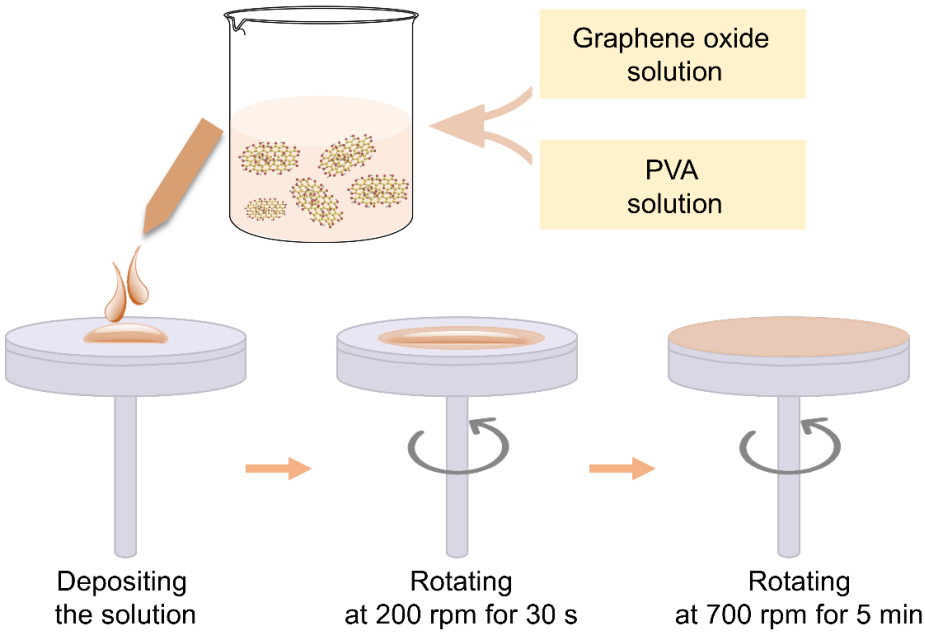

Figure 4-1 Diagram about the preparation procedures of the GO/PVA thin film.

To examine the linear and NLO properties, the prepared GO was mixed with polyvinyl alcohol (PVA) solution under magnetic stirring at 353 K to form a homogenous suspension. Then, the GO/PVA thin film was deposited on a transparent SiO_2 substrate through spin coating. Typically, the suspension of the GO/PVA

composite on the substrate was treated at a spin speed of 200 rpm for the 30 s firstly. Then the film was formed at a spin speed of 700 rpm for 5 min. The schematic diagram of the fabrication process of the GO/PVA thin film was shown in Figure 4-1. Note that the SiO_2 substrate was precleaned with aqua regia and rinsed several times with DI water before use. So that the hydrophobic substances on the substrate were removed clearly, and substrates were modified to hydrophilic. This is a key point to fabricate good film through spin coating with DI water as the solvent.

4.2.3 Structural Characterizations

The crystalline phases and compositions were characterized by using the powder X-ray diffraction (XRD). The XRD patterns were collected using Rigaku Mini Flex over the range of 5 - 50°. Fourier transform infrared spectroscopy (FTIR) measurements were carried out aiming at detecting chemical bonding of as-prepared samples. The TEM images can be recorded on a JEOL, JEM-2100 F1 instrument.

4.2.4 Linear Optical Characterizations

The linear transmission, complex dielectric function as well as refractive index and absorption coefficient of GO were determined using variable angle spectroscopic ellipsometers. Ellipsometric spectra were measured at incidence angles of 70°, 75°, and 80°, respectively. The thickness of GO/PVA thin films were evaluated according to the spectroscopic ellipsometry (SE) results.

4.2.5 Nonlinear Optical Characterizations

The nonlinear transmission changes ($\Delta T/T$), which represent the different transmittance of incident light through samples in the ground state and excited state, were collected by the pump-probe spectroscopies in a femtosecond regime. In measurements, the fundamental laser source was supplied using regenerative amplifiers (Spectra-Physics, Spitfire) with Ti: sapphire (Mai Tai, Spectra-physics) along with Nd: YLF (Empower, Spectra-physics). The laser source has output pulses about 130 fs in wavelength of 800 nm as well as 1 kHz repetitions. Then fundamental laser beams were separated to different portions: pump and probe beams. The wavelength in pump beams is 400 nm, which was converted by a BBO crystal through second harmonic generation. In addition, the repetition of the pump beam was converted to 0.5 kHz through optical choppers. Then pump maximum power density was 1.36 GW/cm^2 and the focal size was 168.2 μm. The probe

beam is a white light continuum with a wavelength range from 450 to 750 nm, which was generated using a sapphire crystal. Note that The chirping effects can be excluded through Kerr gate methods as reported previously [21].

4.3 Results and Discussion

4.3.1 Structural Characterizations of GO

XRD results of GO and graphite can be seen as Figure 4-2(a). The typical peak (002) at 26.6° of graphite disappeared after the liquid oxidation reaction, while a new peak (001) at 10.7° can be observed in GO, implying that GO was successfully obtained. It should be noted that the interlayer spacings in GO (0.84 nm) are much higher compared to the value of original graphite (0.34 nm), indicating the oxygen-containing functional groups were introduced into the GO. In addition, the distinctive degree of oxidization of GO was verified by the FTIR spectroscopy as detailed in Figure 4-2(b). The peaks of O-H, C=O, C-OH, C-O, as well as C-O-C can be seen in FTIR spectrum of GO, respectively. Thus, the strong oxidation of GO has been achieved in the liquid reaction process.

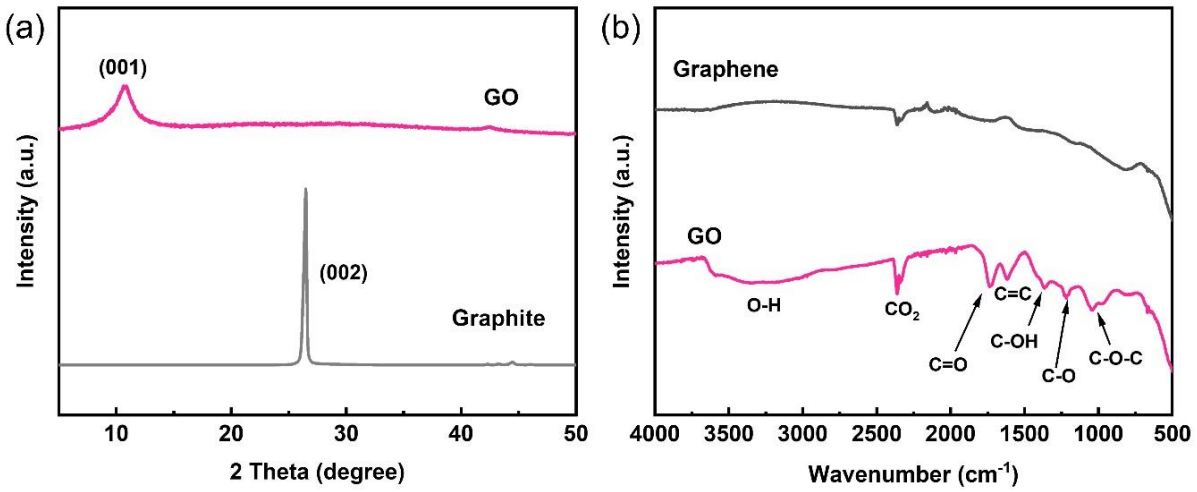

Figure 4-2 (a) XRD results for GO, graphite. (b) FTIR spectra measuring in GO, graphene.

Figure 4-3 provides the TEM images of GO that the thin sheet structures with wrinkled texture were observed. Moreover, because of the interaction of oxygen-containing functions existing at the basal plane, GO tends to form a multilayer structure and low crystallinity.

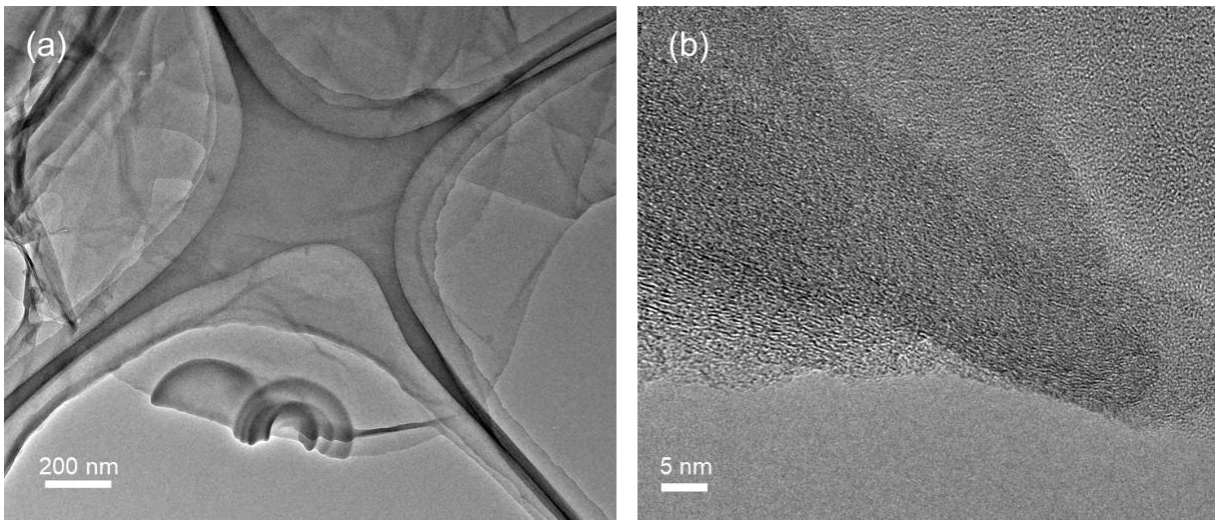

Figure 4-3 (a) Small-magnification, (b) large- magnification TEM of graphene oxide (GO) nanosheets.

4.3.2 Linear Optical Properties of GO

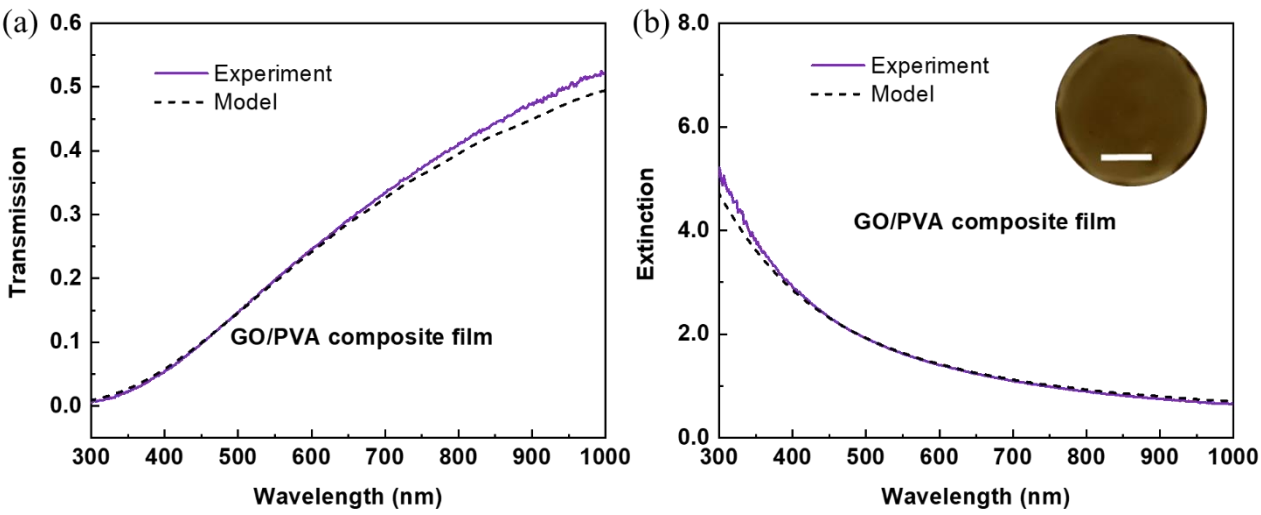

Figure 4-4 (a) Experimental and SE fitted linear transmission spectra of the GO/PVA composite film. (b) Experimental and fitted extinction spectra of the GO/PVA composite film. Inset: photograph of the GO/PVA film on a silica substrate (scale bar, 5 mm).

The experimental and SE model fitted T spectra were given in Figure 4-4(a). The experimental and fitted linear extinction spectrum of the GO/PVA composite are presented in Figure 4-4(b). The extinction was extracted according to $-\ln(T/T_0)$, in which T, T_0 represent linear transmissions of the substrate coating samples, uncoating samples [22]. In recent years, PVA arises as an excellent host polymer matrix for filling

nanomaterials to investigate their optical properties. Because PVA is a water-soluble synthetic polymer and has excellent emulsifying, thin film-forming, and adhesive properties [23]. Most importantly, it does not influence the optical properties of materials that we intend to study. As demonstrated in the previous literature, Hassan A. S. et al. reported that pure PVA is a colorless polymer without obvious absorption and its linear transmission is nearly 100% in the visible range [24]. In addition, previously in our group, Sato et al. fabricated and reported the Au nanorods composite film with PVA, and the extinction was demonstrated to result from the absorption and scattering of the Au nanorods. No obvious absorption of PVA was observed in the visible spectrum [22]. Thus, we suggest that the extinction in Figure 4-4(b) mainly stems from the absorption and scattering of the graphene oxide nanosheets owing to the transparent characteristics of PVA in the visible region [25]. The results show that the linear extinction strength of GO at 450 - 750 nm exhibits a flat dispersion characteristic. The results were consistent with the absorption spectrum measured in the dimethylformamide (DMF) solution [26], indicating that GO nanosheets dispersed well in the PVA matrix seen as the inset photograph presented in Figure 4-4(b). In fitting process, the description of GO/PVA films were obtained using the effective medium approximation (EMA) with a linear dispersion of a concentration of about 72.7%, and a thickness of 1895 nm.

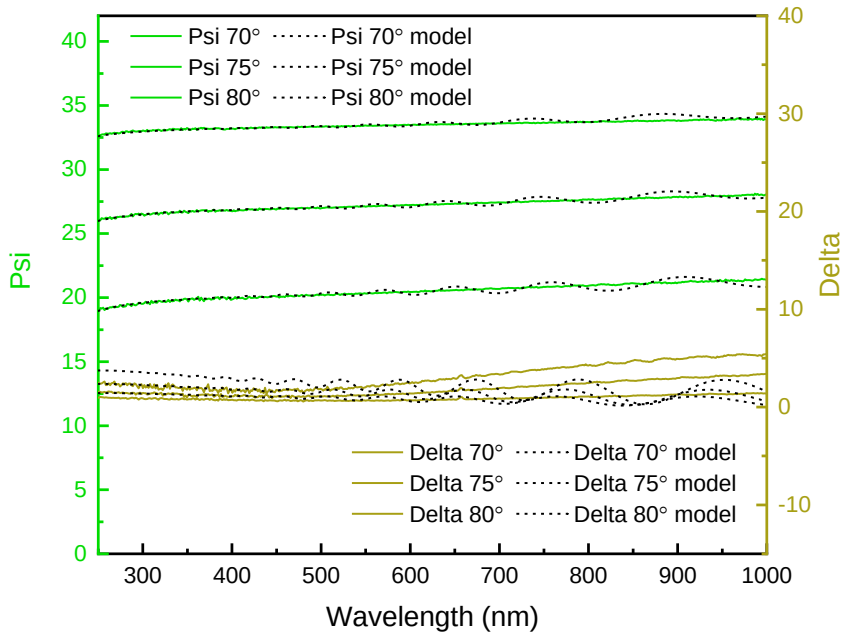

Figure 4-5 Ellipsometry results of the GO/PVA composite. Experimental, fitted ellipsometry for psi (green), delta (yellow) spectra.

The experimental, fitted ellipsometric patterns of the GO/PVA composite can be seen in Figure 4-5. In the SE model, Lorentz oscillators were used to characterize the band-gap structure of GO was characterized by using Lorentz oscillators. The information of oscillators for GO/PVA composite in the ground state was listed in Table 4-1. GO has a larger energy gap compared to graphene, which is ascribed to the introduction of σ state in sp^3-bonded carbon atoms arising from the formation of oxygen-containing functions during the synthesis process [27]. It has been demonstrated by theoretical studies that the energy gap varies with the different coverage of oxygen-containing functional groups in GO [28]. The mean square error (MSE) between the experimental results and the SE model is used to evaluate the fitting quality [29]. Its accuracy is sufficient to provide good fitting qualities with experimental data when the value of MSE is less than 10 [30]; the MSE of the GO/PVA composite was 9.386.

Table 4-1 Information of oscillators for GO/PVA composite in the ground state.

Linear	Oscillator	En (eV)	Amp	Br (eV)
MSE=9.386	Lorentz1	1.764	0.076	93.083
	Lorentz2	6.290	84.450	0.028
	Lorentz3	6.642	0.639	8.109

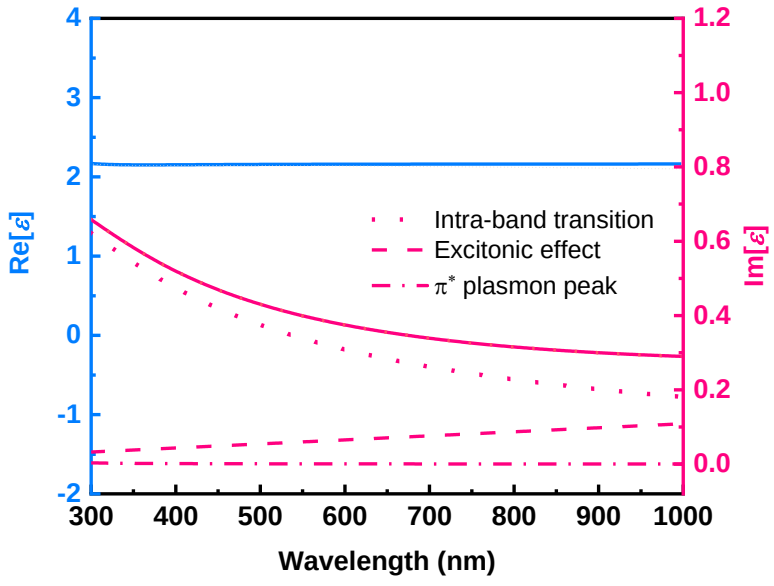

Figure 4-6 Linear dielectric function ε of GO nanosheets.

As shown in Figure 4-6, the linear complex dielectric function ε of GO was evaluated through the SE analyses, where real (Re[ε]), imaginary (Im[ε]) components were marked in blue, red, respectively. The dot,

dash, and dash-dot lines represent the individual contributions of the intra-band transition, excitonic effect, and π* plasmon peak to the imaginary component, respectively. In contrast to the complex ε of graphene, Im[ε] of GO is much lower due to the large band-gap value resulted from the high oxygen content [31].

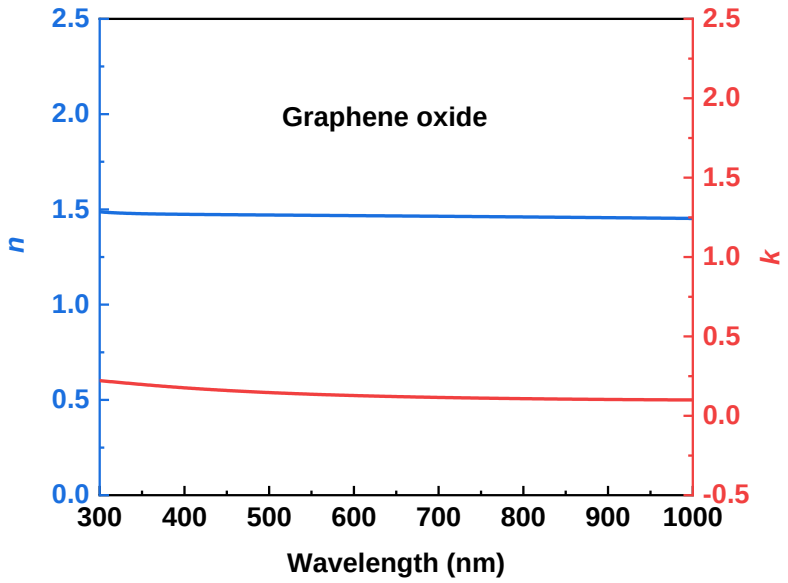

Figure 4-7 Linear refractive index as well as extinction coefficient of GO.

At same time, linear refractive index *n* of GO, as well as absorption coefficient *k*, were also obtained by the SE analyses as in Figure 4-7, which is in good agreement with previous literature [32]. Thus, the obtained ε in the above experiment can be used to analyze the NLO properties through the combination with pump and probe measurement.

4.3.3 Nonlinear Optical Properties of GO

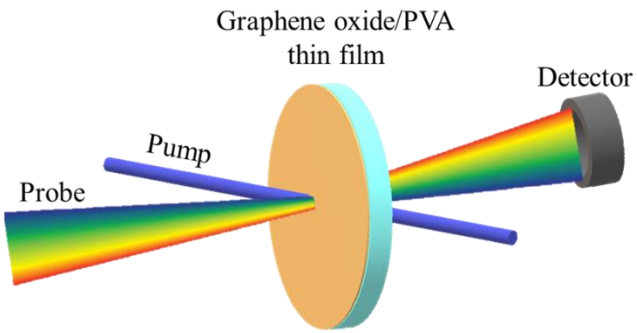

Figure 4-8 Schematic illustration of nonlinear transmission changes measurement in GO/PVA composite.

To investigate the NLO properties of GO, the transmission changes ΔT/T in the GO/PVA composite films were evaluated by the femtosecond pump-probe spectroscopy illustrated as Figure 4-8. As for nonlinear optical properties, Zheng et al. measured the pure PVA film using Z-scan at 1600 GW/cm^2 and no obvious nonlinear response was observed [33]. In addition, many other reports (for instance, Ye and co-workers [34], Wang and coworkers [35]) also reported that pure PVA coated on SiO_2 substrate do not show obvious nonlinear optical response. Moreover, previous research in our group has reported that PVA does not contribute on the nonlinearities of composite thin films [25]. And it has been demonstrated by Zhang et al. [36], PVA has no effect on measured nonlinearities of target composites. Therefore, we consider that transmission changes ΔT/T in the measurement mainly come from graphene oxide nanosheets in the composite thin film.

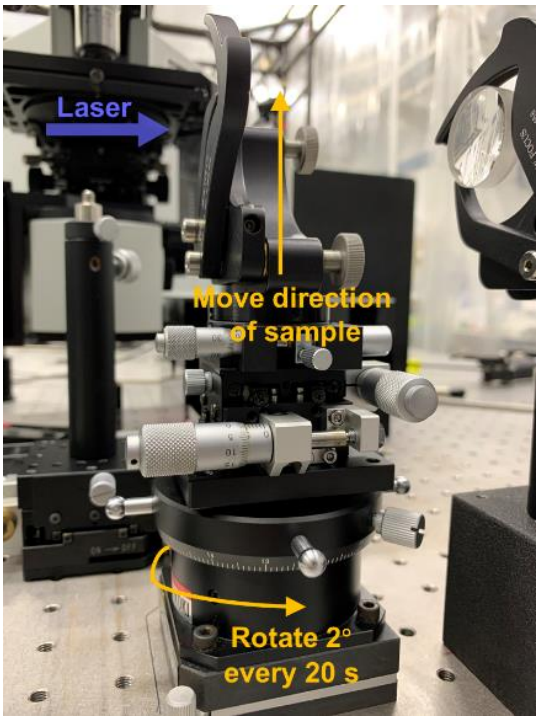

Figure 4-9 The schematic illumination of operating procedures in pump and probe measurement for GO.

It is a standard procedure to check the laser damage of samples in pump and probe measurements. For graphene oxide, we observed photoinduced reduction in our standard two hours' measurement. It implies that the long-term exposure of the GO/PVA composite in the laser beam with a wavelength of 400 nm leads to an unexpected reduction of GO in the pump and probe measurement process. In consideration of that, the laser's spot position was shifted for each data collection in the measurement. It is also a standard procedure to average the single shots of the data collection to avoid the laser-induced reduction effects. It is also a standard procedure to average the single shots of the data collection. The reason is to improve the ratio of signal to noise. In our

experiments, we found that averaging 10000 data points provided us a suitable result. In this case, the data collection takes about 20 seconds. Thus, the laser position on the sample was moved every 20 s to avoid the laser-induced reduction effects. The schematic illumination of the operating procedures was shown in Figure 4-9.

To check the validity of the experimental set-up, we measured sequential data collections. In Figure 4-10, we provided two sequential acquisitions showing no evident changes. Identical measured results were obtained by multiple scans of the sample, which confirmed that no laser-induced damage occurred in the GO/PVA composite film during the measurement.

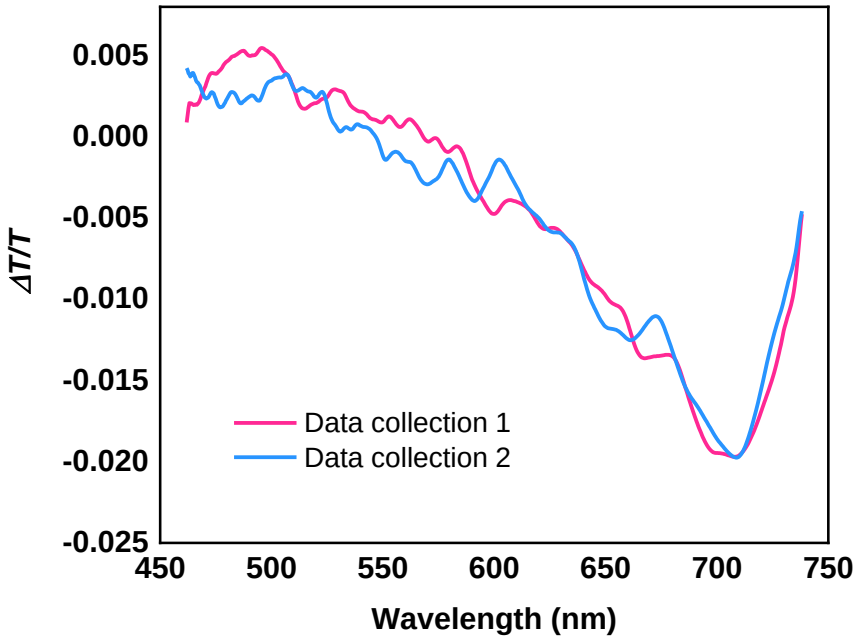

Figure 4-10 Transmission changes ΔT/T of graphene oxide in two sequential data collections.

The ΔT/T pattern measured in GO/PVA composites were presented as Figure 4-11(a), with a wavelength range from 450 to 750 nm. In contrast, previous reports have focused on measurements at discrete wavelengths [37-39], where the fragmental results have led to some conflicting identification of the NLO properties of GO. Some of them may be caused by partial reduction of GO induced by the high-intensity laser beams during the measurement. Because different characteristics could be observed in the ΔT/T pattern of GO if the sample was exposed to the laser without changing the interaction position with the beam (implying that the sample was partially damaged by the laser), which was illustrated as Figure 4-11(b).

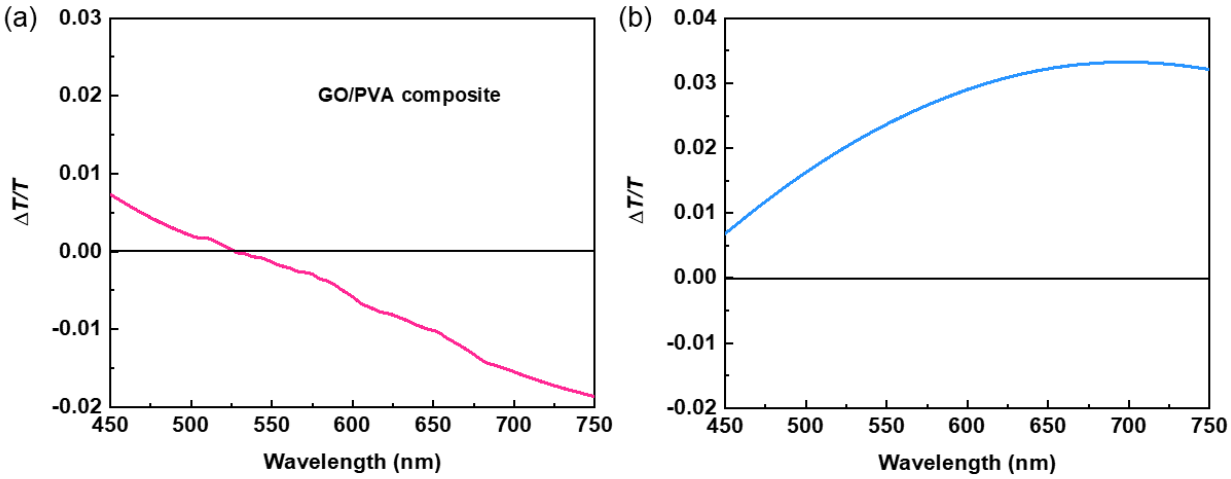

Figure 4-11 (a) Spectral dependence of nonlinear transmission changes of the GO/PVA composite. Wavelength range: 450 to 750 nm. (b) The ΔT/T pattern of GO exposed in the laser without changing the interaction position with the beam.

Our measurement was performed at a continuous spectral region and in a special operating procedure as mentioned above. The coherent spectral transient response enables us to fully understand the photoinduced absorption and transparency of GO. Note that the ΔT/T spectrum of GO in Figure 4-11(a) includes regions of positive and negative signs. A positive region of ΔT/T was observed from 450 to 513 nm, while a negative region of ΔT/T was at the wavelengths from 513 to 750 nm. Negative ΔT/T value is a clear indication of the OL ability of GO, which corresponds to the RSA behavior that absorption across the section at excited state is higher compared to that at ground state. In contrast, the ΔT/T pattern of GO exposed in the laser without changing the interaction position with the beam was shown in Figure 4-11(b). It implies that graphene exhibits positive and monotonic increasing ΔT/T dispersion in the visible region, which represents the strong SA [40, 41]. These results can be explained that GO has unique heterogeneous chemical as well as electronic features arising from co-existence of the sp^2 hybridizations along with sp^3 bonded carbons [42]. The sp^2 hybridizations yield a positive contribution to the transmission changes ΔT/T, while the negative photoinduced sign is ascribable to the sp^3 domains [43, 44]. The result implies that the confined sp^2 hybridization dominates the nonlinear response in GO at the short wavelength, whereas the contributions of sp^2 are overwhelmed under sp^3 effects in long wavelength. By contrast, a significant higher ratio of sp^2 hybridizations dominate the structure in graphene.

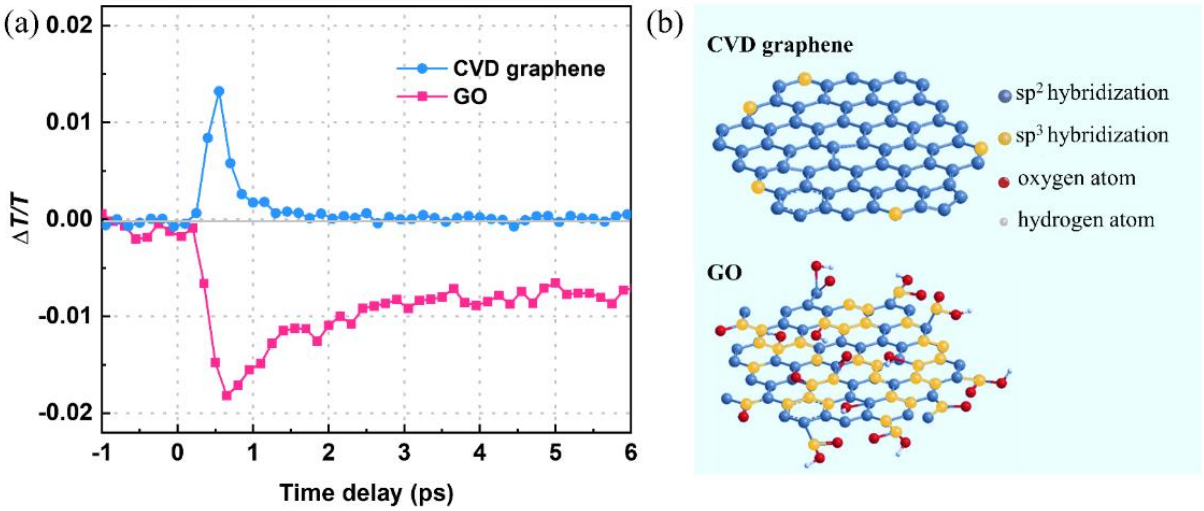

Figure 4-12 (a) Carrier dynamics of GO and CVD graphene at 735 nm excited by a laser pulse with a wavelength of 400 nm. (b) Structural illustrations of GO and CVD graphene.

To further identify the origin of the ultrafast carrier dynamics of GO, the time delay was measured using the GO/PVA composite film at 735 nm with a femtosecond pulse laser, compared it with the graphene fabricated by the CVD method. The differential transmittance of GO and CVD graphene is presented in Figure 4-12(a). It was observed that the carrier dynamics of CVD graphene here are consistent with that in previous reports [45, 46]. By comparison with graphene, a longer time delay was observed in GO, which is fundamentally different from that of graphene. The longer time delay in GO is composed of two parts, which respectively reflect the carrier intraband relaxation process and interband carrier recombination [47]. The difference in the time delay between GO and graphene verified that the sp^2 and sp^3 structures also have an important impact on the relaxation process. Figure 4-12(b) shows the structural illustrations of GO and CVD graphene, respectively. The longer time delay could be ascribed to the confined sp^2 hybridizations, where the π electrons were confined because of the presence of a large fraction of sp^3 bonded carbons. The energy gap of sp^3 bonded carbons is larger than that of sp^2 carbons, resulting in a larger carrier transport gap in GO.

Table 4-2. Information of oscillators for GO/PVA composite in the nonlinear state.

Linear	Oscillator	En (eV)	Amp	Br (eV)
MSE=0.263	Lorentz1	1.789	0.136	5.737
	Lorentz2	6.287	84.370	0.026
	Lorentz3	6.638	0.642	8.089

Finally, the dispersion of $\chi^{(3)}$ of GO was extracted by combining the SE with pump-probe spectroscopies. In the beginning, the linear ε and T has already been evaluated from the SE results. Subsequently, the ε+Δε values (the dielectric function under excitation) were obtained through fitting the T + ΔT and the SE model used in the linear optical analysis; then the dielectric function changes Δε can be calculated [48]. In the fitting process, only the parameters of oscillators were regarded as the variable values; the oscillators' parameters in the excited state were given in Table 4-2. Eventually, the $\chi^{(3)}$ was extracted according to the equation (4-1):

$$\Delta\varepsilon\left(\omega_{probe}\right) = \frac{3}{4}\,\chi^{(3)}\left(\omega_{probe}\right)I \qquad (4\text{-}1)$$

3/4 represents refractive index that dependent on intensities in the equation, and *I* represent pump lasers intensities, respectively [49]. Figure 4-13 present real, imaginary parts for $\chi^{(3)}$ of GO, respectively. The dispersion in Re[$\chi^{(3)}$] as well as Im[$\chi^{(3)}$] show wavelength-dependent characteristics in the visible region. As mentioned in the introduction, they cannot be understood well using single wavelength measurements. In particular, the Im[$\chi^{(3)}$] of GO shows different distributions locating in positive and negative in different wavelength range, which is consistent with the aforementioned ΔT/T. The Im[$\chi^{(3)}$] value of GO reported by M. Ebrahimi et al. at 532 nm was 2.17 × 10-14 m^2/V^2 [50]. Liaros et al. reported that the Im[$\chi^{(3)}$] of GO dispersed in different solvents at 532 nm varied from 1.0 × 10-19 to 5.1 × 10-19 m^2/V^2 [13]. In addition, the Re[$\chi^{(3)}$] and Im[$\chi^{(3)}$] of GO were reported by Khanzadeh et al. to be -3.2 × 10-16 and 4.0 × 10-16 at 532 nm, respectively [17]. At the same wavelength, the Re[$\chi^{(3)}$] as well as Im[$\chi^{(3)}$] obtained in our results are -8.97 × 10-18 and 1.5 × 10-19 m^2/V^2, respectively. The different magnitude of $\chi^{(3)}$ probably stems from the different oxygen content in the sample or the different test methods. Noticeably, unlike the previous reports measured at a single wavelength, where the $\chi^{(3)}$ of GO has huge variations. Our results obtained the dispersion of $\chi^{(3)}$ in a continuous wavelength range from 450 to 750 nm. The positive sign of Im[$\chi^{(3)}$] was observed from 513 to 750 nm, which indicates that the imaginary component of dielectric function increases in the excited state. In consequence, the absorption under excitations exhibits higher compared to that without excitations condition, and GO exhibits RSA behavior [51], which are effective when employed in the optical limiters. In addition, nonlinear response with SA features can be identified over short wavelength range.

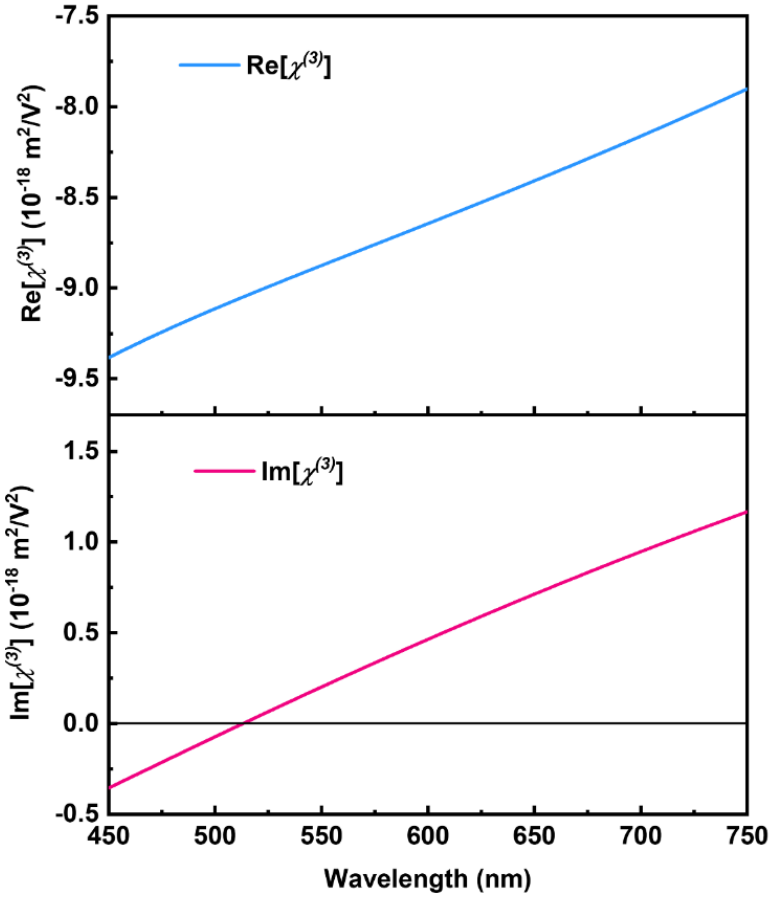

Figure 4-13 Real along with imaginary parts in third-order optical susceptibilities $\chi^{(3)}$ for GO, wavelength range: 450 to 750 nm.

For graphene, it is mainly constituted by a lot of sp^2 hybridizations. The energy gaps from valence bands to conduction bands in the π states of sp^2 hybrid carbons are reported to be approximately 0.5 eV [52]. As a result, electrons in sp^2 hybridizations exhibited saturated absorption because of the valence depletions as well as conduction band fillings [53]. These sp^2 hybridizations dominate the nonlinear optical response of graphene under laser excitation. From our measurements, GO shows SA and RSA behaviors at different wavelength ranges. Most probably the wavelength-dependent characteristics could be explained by the heterogeneous electronic structure in GO, which are dominated through δ states with sp^3 hybridizations in addition to the π states of sp^2 hybrid carbons arising from the introduction of oxygen functions to the basal sheets [54]. Bound electrons and free carriers were involved in the δ states of sp^3 bonded carbons [55], which brought on reverse saturable absorption. Furthermore, the cross-point can be altered through changing the fraction of sp^2 and sp^3 hybridizations in GO. This provides us opportunities to tailor the NLO properties and OL performance of GO by tuning its oxidization degree.

4.4 Conclusions

To be summary, in this chapter we experimentally determined third-order optical susceptibility for graphene oxide by combinations of spectroscopic ellipsometry with pump-probe spectroscopies. It was identified that linear optical response of GO presents a flat dispersion over visible regions. While nonlinear response in GO exhibits saturable absorption (SA) ranging in short wavelength and reverse saturable absorption (RSA) at long wavelength. Compared to the graphene that the structure is dominated by sp^2 hybridized carbons, GO can be utilized in the optical limiter based on RSA behavior located using the wavelengths from 513 to 750 nm. These results propel the application of GO in broadband OL devices. In addition, the physical identification of carrier dynamics that origin from sp^2 domains and sp^3 carbons provides us opportunities to tailor the NLO properties as well as OL performance for GO by controlling the oxidization degree.

References

[1] C. Momma, B.N. Chichkov, S. Nolte, F. von Alvensleben, A. Tünnermann, H. Welling, B. Wellegehausen, Short-pulse laser ablation of solid targets, Optics Communications, 129 (1996) 134-142.

[2] Y. Qiao, F. Ma, C. Liu, B. Zhou, Q. Wei, W. Li, D. Zhong, Y. Li, M. Zhou, Near-Infrared Laser-Excited Nanoparticles To Eradicate Multidrug-Resistant Bacteria and Promote Wound Healing, ACS Appl Mater Interfaces, 10 (2018) 193-206.

[3] D. Heflinger, T. Arusi-Parpar, Y. Ron, R.J.O.c. Lavi, Application of a unique scheme for remote detection of explosives, 204 (2002) 327-331.

[4] A. Howes, Z. Zhu, D. Curie, J.R. Avila, V.D. Wheeler, R.F. Haglund, J.G. Valentine, Optical Limiting Based on Huygens' Metasurfaces, Nano Lett, 20 (2020) 4638-4644.

[5] M.O. Senge, M. Fazekas, E.G.A. Notaras, W.J. Blau, M. Zawadzka, O.B. Locos, E.M. Ni Mhuircheartaigh, Nonlinear Optical Properties of Porphyrins, Advanced Materials, 19 (2007) 2737-2774.

[6] R. Signorini, M. Meneghetti, R. Bozio, M. Maggini, G. Scorrano, M. Prato, G. Brusatin, P. Innocenzi, M.J.C. Guglielmi, Optical limiting and non linear optical properties of fullerene derivatives embedded in hybrid sol–gel glasses, 38 (2000) 1653-1662.

[7] P. Zhu, P. Wang, W. Qiu, Y. Liu, C. Ye, G. Fang, Y.J.A.P.L. Song, Optical limiting properties of phthalocyanine-fullerene derivatives, 78 (2001) 1319-1321.

[8] P. Chantharasupawong, R. Philip, T. Endo, J. Thomas, Enhanced optical limiting in nanosized mixed zinc ferrites, Applied Physics Letters, 100 (2012).

[9] R. Philip, P. Chantharasupawong, H. Qian, R. Jin, J. Thomas, Evolution of nonlinear optical properties: from gold atomic clusters to plasmonic nanocrystals, Nano Lett, 12 (2012) 4661-4667.

[10] J. Zhu, Y. Li, Y. Chen, J. Wang, B. Zhang, J. Zhang, W.J. Blau, Graphene oxide covalently functionalized with zinc phthalocyanine for broadband optical limiting, Carbon, 49 (2011) 1900-1905.

[11] S.M. Jilani, T.D. Gamot, P. Banerji, S. Chakraborty, Studies on resistive switching characteristics of aluminum/graphene oxide/semiconductor nonvolatile memory cells, Carbon, 64 (2013) 187-196.

[12] M. Seredych, O. Mabayoje, T.J. Bandosz, Visible-light-enhanced interactions of hydrogen sulfide with composites of zinc (oxy)hydroxide with graphite oxide and graphene, Langmuir, 28 (2012) 1337-1346.

[13] N. Liaros, K. Iliopoulos, M.M. Stylianakis, E. Koudoumas, S. Couris, Optical limiting action of few layered graphene oxide dispersed in different solvents, Optical Materials, 36 (2013) 112-117.

[14] M. Feng, H. Zhan, Y. Chen, Nonlinear optical and optical limiting properties of graphene families, Applied

Physics Letters, 96 (2010).

[15] C. Fang, B. Dai, R. Hong, C. Tao, Q. Wang, X. Wang, D. Zhang, S. Zhuang, Tunable optical limiting optofluidic device filled with graphene oxide dispersion in ethanol, Sci Rep, 5 (2015) 15362.

[16] U. Kürüm, O.Ö. Ekiz, H.G. Yaglioglu, A. Elmali, M. Ürel, H. Güner, A.K. Mızrak, B. Ortaç, A. Dâna, Electrochemically tunable ultrafast optical response of graphene oxide, Applied Physics Letters, 98 (2011).

[17] M. Khanzadeh, M. Dehghanipour, M. Karimipour, M. Molaei, Improvement of nonlinear optical properties of graphene oxide in mixed with Ag_2S@ZnS core-shells, Optical Materials, 66 (2017) 664-670.

[18] S. Biswas, A.K. Kole, C.S. Tiwary, P. Kumbhakar, Enhanced nonlinear optical properties of graphene oxide–silver nanocomposites measured by Z-scan technique, RSC Advances, 6 (2016) 10319-10325.

[19] N. Liaros, P. Aloukos, A. Kolokithas-Ntoukas, A. Bakandritsos, T. Szabo, R. Zboril, S. Couris, Nonlinear Optical Properties and Broadband Optical Power Limiting Action of Graphene Oxide Colloids, The Journal of Physical Chemistry C, 117 (2013) 6842-6850.

[20] Y. Sun, J. Tang, K. Zhang, J. Yuan, J. Li, D.M. Zhu, K. Ozawa, L.C. Qin, Comparison of reduction products from graphite oxide and graphene oxide for anode applications in lithium-ion batteries and sodium-ion batteries, Nanoscale, 9 (2017) 2585-2595.

[21] W.J. Tan, H. Liu, J.H. Si, X. Hou, Control of the gated spectra with narrow bandwidth from a supercontinuum using ultrafast optical Kerr gate of bismuth glass, Applied Physics Letters, 93 (2008) 051109.

[22] R. Sato, J. Henzie, H. Rong, M. Naito, Y. Takeda, Enhancement of the complex third-order nonlinear optical susceptibility in Au nanorods, Opt Express, 27 (2019) 19168-19176.

[23] M.H.M. Ahmed, N.M. Ali, Z.S. Salleh, A.A. Rahman, S.W. Harun, M. Manaf, H. Arof, All fiber mode-locked Erbium-doped fiber laser using single-walled carbon nanotubes embedded into polyvinyl alcohol film as saturable absorber, Opt Laser Technol, 62 (2014) 40-43.

[24] N.J. Mohammed, Z.S. Rasheed, A.S. Hassan, Improvement Optical Properties of PVA/ TiO_2 and PVA/ ZnO Nanocomposites, Al-Mustansiriyah Journal of Science, 29 (2019) 118-123.

[25] R. Sato, S. Ishii, T. Nagao, M. Naito, Y. Takeda, Broadband Plasmon Resonance Enhanced Third-Order Optical Nonlinearity in Refractory Titanium Nitride Nanostructures, ACS Photonics, 5 (2018) 3452-3458.

[26] X.L. Zhang, Z.B. Liu, X.C. Li, Q. Ma, X.D. Chen, J.G. Tian, Y.F. Xu, Y.S. Chen, Transient thermal effect, nonlinear refraction and nonlinear absorption properties of graphene oxide sheets in dispersion, Opt Express, 21 (2013) 7511-7520.

[27] D.W. Lee, J.W. Seo, sp^2/sp^3 Carbon Ratio in Graphite Oxide with Different Preparation Times, The Journal of Physical Chemistry C, 115 (2011) 2705-2708.

[28] D.W. Boukhvalov, M.I. Katsnelson, Modeling of graphite oxide, J Am Chem Soc, 130 (2008) 10697-10701.

[29] Y. Yang, N. Akozbek, T.-H. Kim, J.M. Sanz, F. Moreno, M. Losurdo, A.S. Brown, H.O. Everitt, Ultraviolet–Visible Plasmonic Properties of Gallium Nanoparticles Investigated by Variable-Angle Spectroscopic and Mueller Matrix Ellipsometry, ACS Photonics, 1 (2014) 582-589.

[30] Z. Song, B.R. Rogers, N.D. Theodore, Spectroscopic ellipsometry characterization of ZrO_2 films on Si(100) deposited by high-vacuum-metalorganic chemical vapor deposition, Journal of Vacuum Science & Technology A: Vacuum, Surfaces, and Films, 22 (2004) 711-718.

[31] F. Nasehnia, S.M. Lima, M. Seifi, E. Mehran, First principles study on optical response of graphene oxides: From reduced graphene oxide to the fully oxidized surface, Comp Mater Sci, 114 (2016) 112-120.

[32] Y. Shen, P. Zhou, Q.Q. Sun, L. Wan, J. Li, L.Y. Chen, D.W. Zhang, X.B. Wang, Optical investigation of reduced graphene oxide by spectroscopic ellipsometry and the band-gap tuning, Applied Physics Letters, 99 (2011) 141911.

[33] X. Zheng, R. Chen, G. Shi, J. Zhang, Z. Xu, X. Cheng, T. Jiang, Characterization of nonlinear properties of black phosphorus nanoplatelets with femtosecond pulsed Z-scan measurements, Opt Lett, 40 (2015) 3480-3483.

[34] Y. Ye, Y. Xian, J. Cai, K. Lu, Z. Liu, T. Shi, J. Du, Y. Leng, R. Wei, W. Wang, X. Liu, G. Bi, J. Qiu, Linear and Nonlinear Optical Properties of Few-Layer Exfoliated SnSe Nanosheets, Advanced Optical Materials, 7 (2019) 1800579.

[35] G. Wang, A.A. Baker-Murray, X. Zhang, D. Bennett, J.J. Wang, J. Wang, K. Wang, W.J. Blau, Broadband saturable absorption and exciton-exciton annihilation in $MoSe_2$ composite thin films, Optical Materials Express, 9 (2019) 483-496.

[36] B. Zhang, R. Sato, H. Momida, T. Ohno, M. Chundak, M. Naito, M. Yoshitake, Y. Takeda, Spectral dependence of the third-order optical susceptibility of Au nanostructures: Experiments and first-principles calculations, Physical Review B, 100 (2019) 035446.

[37] V. Nalla, L. Polavarapu, K.K. Manga, B.M. Goh, K.P. Loh, Q.H. Xu, W. Ji, Transient photoconductivity and femtosecond nonlinear optical properties of a conjugated polymer-graphene oxide composite, Nanotechnology, 21 (2010) 415203.

[38] J. Ren, X.R. Zheng, Z.M. Tian, D. Li, P. Wang, B.H. Jia, Giant third-order nonlinearity from low-loss electrochemical graphene oxide film with a high power stability, Applied Physics Letters, 109 (2016) 221105.

[39] J. Shang, L. Ma, J. Li, W. Ai, T. Yu, G.G. Gurzadyan, Femtosecond pump–probe spectroscopy of graphene

oxide in water, Journal of Physics D: Applied Physics, 47 (2014) 094008.
[40] B.A. Ruzicka, S. Wang, J.W. Liu, K.P. Loh, J.Z. Wu, H. Zhao, Spatially resolved pump-probe study of single-layer graphene produced by chemical vapor deposition, Optical Materials Express, 2 (2012) 708-716.
[41] J.Z. Shang, Z.Q. Luo, C.X. Cong, J.Y. Lin, T. Yu, G.G. Gurzadyan, Femtosecond UV-pump/visible-probe measurements of carrier dynamics in stacked graphene films, Applied Physics Letters, 97 (2010) 163103.
[42] H.K. Jeong, M.H. Jin, K.P. So, S.C. Lim, Y.H. Lee, Tailoring the characteristics of graphite oxides by different oxidation times, J Phys D Appl Phys, 42 (2009) 065418.
[43] Z.-B. Liu, X. Zhao, X.-L. Zhang, X.-Q. Yan, Y.-P. Wu, Y.-S. Chen, J.-G. Tian, Ultrafast Dynamics and Nonlinear Optical Responses from sp^2 and sp^3 Hybridized Domains in Graphene Oxide, The Journal of Physical Chemistry Letters, 2 (2011) 1972-1977.
[44] B.A. Ruzicka, L.K. Werake, H. Zhao, S. Wang, K.P. Loh, Femtosecond pump-probe studies of reduced graphene oxide thin films, Applied Physics Letters, 96 (2010) 173106.
[45] D. Sun, Z.K. Wu, C. Divin, X.B. Li, C. Berger, W.A. de Heer, P.N. First, T.B. Norris, Ultrafast Relaxation of Excited Dirac Fermions in Epitaxial Graphene Using Optical Differential Transmission Spectroscopy, Phys Rev Lett, 101 (2008) 157402.
[46] E. Rajackaitė, D. Peckus, R. Gudaitis, M. Andrulevičius, T. Tamulevičius, D. Volyniuk, Š. Meškinis, S. Tamulevičius, Transient absorption spectroscopy as a promising optical tool for the quality evaluation of graphene layers deposited by microwave plasma, Surface and Coatings Technology, 395 (2020) 125887.
[47] X. Zhao, Z.B. Liu, W.B. Yan, Y.P. Wu, X.L. Zhang, Y.S. Chen, J.G. Tian, Ultrafast carrier dynamics and saturable absorption of solution-processable few-layered graphene oxide, Applied Physics Letters, 98 (2011) 121905.
[48] R. Sato, M. Ohnuma, K. Oyoshi, Y. Takeda, Spectral investigation of nonlinear local field effects in Ag nanoparticles, J Appl Phys, 117 (2015) 113101.
[49] R. Sato, M. Ohnuma, K. Oyoshi, Y. Takeda, Experimental investigation of nonlinear optical properties of Ag nanoparticles: Effects of size quantization, Physical Review B, 90 (2014) 125417.
[50] M. Ebrahimi, A. Zakery, M. Karimipour, M. Molaei, Nonlinear optical properties and optical limiting measurements of graphene oxide – Ag@TiO_2 compounds, Optical Materials, 57 (2016) 146-152.
[51] A. Santhi, V.V. Namboodiri, P. Radhakrishnan, V.P.N. Nampoori, Spectral dependence of third order nonlinear optical susceptibility of zinc phthalocyanine, J Appl Phys, 100 (2006) 053109.
[52] G. Eda, Y.Y. Lin, C. Mattevi, H. Yamaguchi, H.A. Chen, I.S. Chen, C.W. Chen, M. Chhowalla, Blue photoluminescence from chemically derived graphene oxide, Adv Mater, 22 (2010) 505-509.

[53] S. Wang, Y.L. Dong, C.Y. He, Y.C. Gao, N. Jia, Z.M. Chen, W.N. Song, The role of sp^2/sp^3 hybrid carbon regulation in the nonlinear optical properties of graphene oxide materials, Rsc Advances, 7 (2017) 53643-53652.

[54] S. Perumbilavil, P. Sankar, T. Priya Rose, R.J.A.P.L. Philip, White light Z-scan measurements of ultrafast optical nonlinearity in reduced graphene oxide nanosheets in the 400–700 nm region, 107 (2015) 051104.

[55] H. Shi, C. Wang, Z. Sun, Y. Zhou, K. Jin, S.A. Redfern, G. Yang, Tuning the nonlinear optical absorption of reduced graphene oxide by chemical reduction, Opt Express, 22 (2014) 19375-19385.

Chapter 5

Broadband and Comparative Third-order Nonlinearities in Reduced Graphene Oxide with CVD Graphene

5.1 Introduction

The trend towards ultimate miniaturization [1], and applicable over broad wavelength region [2], is expected for the applications in various nanophotonic technologies, such as all-optical signal processing [3], optical information storage, and communication [4, 5]. The enhancement of optical nonlinearity achieved by surface plasmon, a collective form of electron excitation, enable noble metal nanostructures to attain the concentration and manipulation of light at the nanoscale [6, 7]. This functionality has stimulated their use in several devices including optical nanoantenna and resonators [7]. However, noble metal materials with fixed geometry suffer from insurmountable obstacles that their tunability is limited in external electronic fields [8]. Consequently, the applications of noble metallic nanostructures in optical processing devices are severely restricted, and alternative materials are being sought to address these technical limitations. Superior to noble metals, the optical nonlinearity of graphene is highly tunable by controlling the chemical potential. The chemical potential could be realized efficiently through method of doping or electrical gating [9]. In addition to addressing these limitations, graphene can offer extremely spatial confinement of light and favorably low optical loss for nanophotonic applications [10, 11]. The graphene utilized in these nanophotonic devices is usually fabricated by the chemical vapor deposition (CVD) method [12, 13]. However, CVD graphene suffered high-temperature requirements, complicated and high-cost techniques in the fabrication process [14], and difficult transfer procedures off the substrate [15], which hampered their scalable application.

Reduced graphene oxide emerges to be possible alternative instead of CVD graphene to be employed in

nanophotonic devices, with relatively simple and low-cost preparation methods, despite some defects induced in the synthesis process [16]. Also, reduced graphene oxide possesses remarkable flexible compatibility, chemical, and thermal stabilities [17, 18]. In moving towards the application of reduced graphene oxide in nanophotonic devices, comparable nonlinear optical response and tunability to CVD graphene are essentially required. Because the third-order nonlinear susceptibilities $\chi^{(3)}$ are complex quantities. It contains the real and imaginary parts and has relation to nonlinear optical parameters. The $\chi^{(3)}$ describe the distribution of refraction and absorption in excited state [19, 20]. In addition, because of electronic transitions, nonlinear optical (NLO) property in reduced graphene oxide is wavelength-dependent [21]. So, the well-studied $\chi^{(3)}$, which reflects the substantial response of materials to wavelength and pulse width of light in a nonlinear state, is an important step aiming control on light in nanometer scales in all applications [22]. Although the $\chi^{(3)}$ of reduced graphene oxide has been so far investigated [23-26], mainly focus on 532 or 1064 nm. There is no report concerning the experimental determination of $\chi^{(3)}$ in the continuous visible region, which is important to the extent of its nanophotonic functionalities toward broad wavelength range.

Enlightened by the above consideration, we experimentally investigated the wavelength-dependent nonlinearity of reduced graphene oxide in the visible spectrum, as well as CVD graphene thin film as a comparison. Via the combination of spectroscopic ellipsometry with femtosecond pump-probe spectroscopies [27], we obtained $\chi^{(3)}$ dispersion of reduced graphene oxide and CVD graphene from 450 to 750 nm. The underlying physical mechanisms involved in their nonlinearities were discussed as well, that π conjugation electronic transitions plays a dominant role in imparting the momentum for their nonlinear optical transitions. Also, these analyses allow us to make a comparison on the nonlinearities of reduced graphene oxide with that of CVD graphene. The results indicate that reduced graphene oxide possesses broadband and comparable nonlinearity achieved by CVD graphene thin film. These availabilities, in addition to their relatively easy and low-cost fabrication process [28], validate reduced graphene oxide to be a promising alternative approach toward the light propagation, concentration, conversion, and manipulation at the nanoscale in the visible region.

5.2 Experimental Section

5.2.1 Preparations of Graphene Oxide

Graphene oxide has been made using graphite flake using modified Hummers' methods. The synthesis method has been reported in previous work [29]. In detail, 0.5 g graphite flake and 0.25 g $NaNO_3$ were mixed

firstly in a 500 mL beaker filled with 50 mL H_2SO_4 (98%) in an ice-water bath under stirrings. The stirrings of above mixed solution were then kept at 25 ℃ for 24 hours after adding 1.5 g $KMnO_4$. A yellow suspension was obtained after adding 100 mL water and 30 mL H_2O_2 until reactions completed. The graphene oxide solution was obtained after washed several times through centrifugation using HCl and deionized water until the PH reached 7.

5.2.2 Fabrication of Reduced Graphene Oxide/PVA Composite Thin Films

To measure optical characterizations of reduced graphene oxide, composite films containing polyvinyl alcohol (PVA) and reduced graphene oxide were made uniformly using silica glass substrates as the following procedure. Firstly, 5 g of PVA (Sigma-Aldrich, molecular weight around 6000) powders were dissolved to 30 mL deionized water (DI) using stirrings, a transparent PVA mixture could be obtained after heated over 24 hours at 95 ℃, then the mixture was cooled to 25 ℃. Afterward, 5 mL as-prepared PVA solution was simply mixed with aqueous graphene oxide solution (3 mL, 9.5 mg/mL) under sonication for 2 h. To convert graphene oxide in the composite into reduced graphene oxide, 0.285 mL hydrazine monohydrate (Alfa Aesar, 99+%) aqueous solution was dropped into the resulting mixture and reduced reaction was in proceed at 80 ℃ for 24 h in a water bath under stirring. Finally, the well-dispersed reduced graphene oxide solution with PVA were spin-coated using silica glass substrates. Note that glass substrate was precleaned with aqua regia and rinsed several times with DI water before use. For comparison, CVD graphene thin film on silica substrate was purchased from the graphene platform corporation.

5.2.3 Structural Characterizations

The phase information was investigated by the X-ray diffraction (XRD) method. The XRD patterns were collected by measuring Rigaku MiniFlex 600. Cu Kα radiation was used in the equipment with wavelength of 0.154 nm. The morphologies, microstructures of reduced graphene oxide can be measured in SEM, TEM.

5.2.4 Linear Optical Measurements and Evaluation

The linear transmission and other characterizations on CVD graphene as well as reduced graphene oxide can be explored using variable angle spectroscopic ellipsometry. The dielectric function of CVD graphene and reduced graphene oxide were evaluated according to SE result.

5.2.5 Nonlinear Optical Characterizations

NLO properties for CVD graphene, reduced graphene oxide can be investigated using customer designed pump-probe spectroscopies in fs regime. The basic lasers source has wavelength ~ 800 nm. The source was supplied using regenerative amplifiers (Spectra-Physics, Spitfire). A laser beam with pulse width ~ 130 fs and repetition rate ~ 1 kHz was then divided to different components: one is pump beam; another is probe beam. For the pump beam: a 400 nm laser beam was obtained through converted by BBO crystals. Then, output repetition rates were obtained with a decrease through optical choppers, as 0.5 kHz in the end. For probe beam: white light supercontinuum ranging from 400 to 800 nm could be generated through converted by sapphire crystal. The Kerr gate technique was applied to correct the chirping effect of raw data, which was reported in previous literature [30].

5.3 Results and Discussion

5.3.1 Structural Characterizations

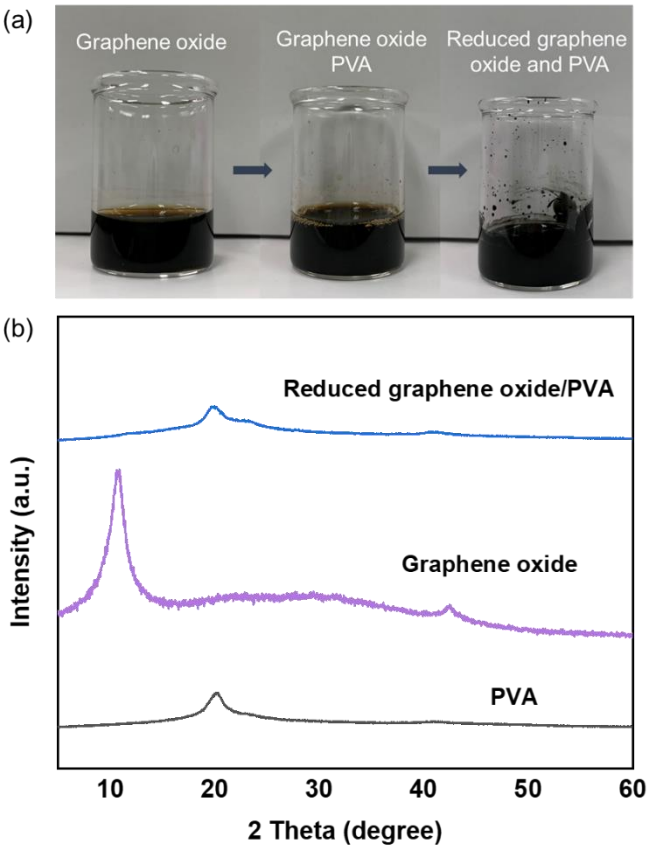

Figure 5-1 (a) Digital photos and (b) XRD: graphene oxide, PVA, reduced graphene oxide/PVA, respectively.

The digital photos and XRD patterns of graphene oxide, PVA, graphene oxide/PVA, as well as reduced graphene oxide/PVA can be seen as above. Figure 5-1(b) illustrates that graphene oxide appeared a featured diffraction peak at 2 Theta =12.1° can be corresponded with (001) lattice plane [31]. Graphene oxide/PVA composite shows only the diffraction peak of PVA but no graphene oxide characteristic peak. It could be explained as that the ratio of graphene oxide to PVA is very low and graphene oxide nanosheets are dispersed homogeneously in the PVA [32]. After reacting with hydrazine monohydrate, graphene oxide was reduced into graphene and functional groups were removed effectively. As shown in Figure 5-1(a), bright brown graphene oxide/PVA solution transformed to a clear black reduced graphene oxide/PVA solution without obvious aggregation or precipitation.

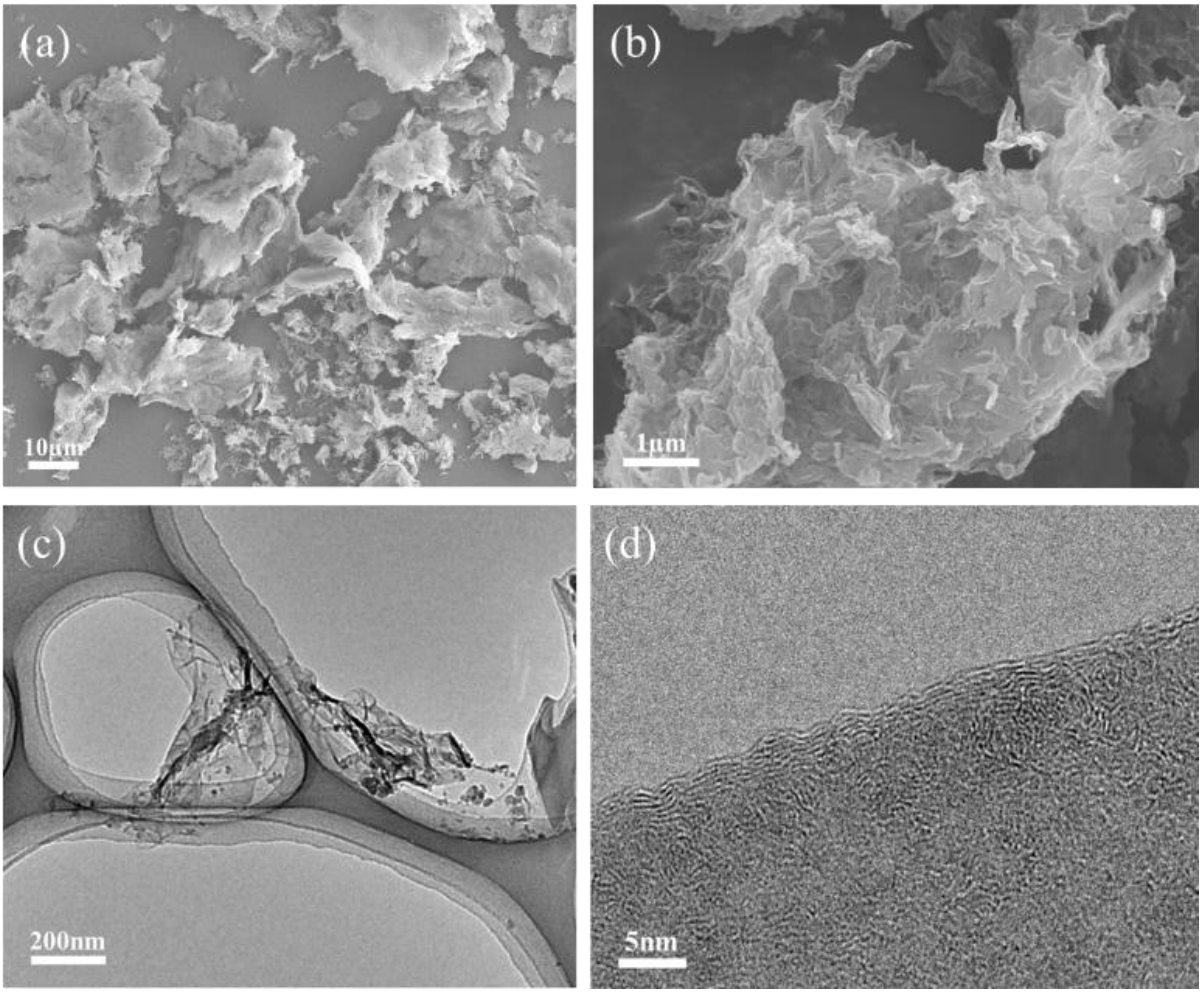

Figure 5-2 (a, b) SEM characterization for reduced graphene oxide. (c, d) TEM for reduced graphene oxide.

The morphologies and microstructures for rGO can be studied using field emission scanning electron microscopy (SEM) and transmission electron microscopy (TEM), which were provided as Figure 5-2, correspondingly. Figure 5-2(a) along with (b) present that obtained reduced graphene

oxide exhibits typical wrinkle morphology and nanosheets structure with dimension in micrometers. After effectively ultrasonication, reduced graphene oxide nanosheets with size around a few hundred nanometers were observed on the top of the copper grid as shown in Figure 5-2(c). From observed TEM images with large magnification in Figure 5-2(d), the few layers stacking structure and the individual layers in reduced graphene oxide could be observed.

5.3.2 Linear Optical Properties of Reduced Graphene Oxide and CVD Graphene

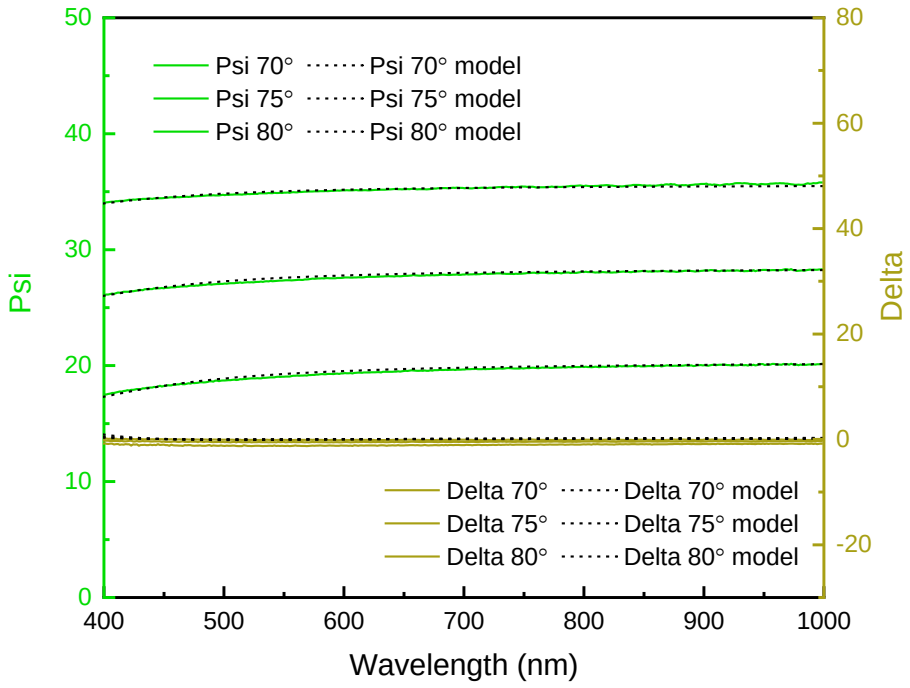

Figure 5-3 Ellipsometric results of CVD graphene thin film. Experimental and fitted ellipsometric for psi (green) and delta (yellow) spectra.

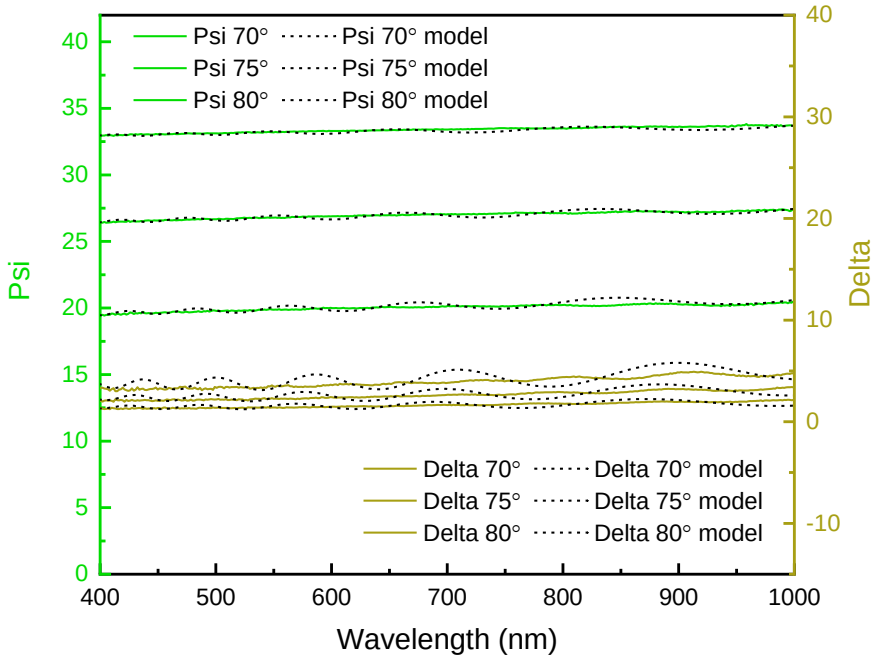

Figure 5-4 Ellipsometric results of reduced graphene oxide/PVA composite. Experimental and fitted ellipsometry for psi (green) and delta (yellow) spectra.

Spectroscopic ellipsometry (SE) is a useful technique to investigate the linear optical properties [33]. We measured the SE over incidence angles from 70° to 80° by 5° steps for CVD graphene thin film along with reduced graphene oxide/PVA composite, respectively seen as Figure 5-3 and Figure 5-4. It was demonstrated that Lorentz oscillators could be adopted to analyze the ellipsometry of graphene [34, 35]. Three Lorentz oscillators were used to characterize the bandgap in CVD graphene and reduced graphene oxide [36]. The fitting quality can be described by minimized mean squared error (MSE) of experimental data compared with SE models. The description is regarded as accurate enough when MSE is less than 10 [37]. In our work, the obtained SE model fitted well with MSE of 6.335 and 4.856 for CVD graphene and reduced graphene oxide/PVA composite, respectively. The corresponding fitting oscillators' parameters were provided in Table 5-1 and 5-2.

Table 5-1 Information of oscillators for CVD graphene thin film in ground-state.

Linear	Oscillator	En (eV)	Amp	Br (eV)
MSE=6.335	Lorentz1	0.237	68.717	6.720
	Lorentz2	3.715	4.260	2.505

	Lorentz3	4.389	5.189	0.866

Table 5-2 Information of oscillators for reduced graphene oxide/PVA composite in ground-state.

Linear	Oscillator	En (eV)	Amp	Br (eV)
MSE=4.856	Lorentz1	0.208	18.676	9.250
	Lorentz2	4.664	1.750	2.228
	Lorentz3	5.276	0.825	10.857

The thickness and linear dielectric function ε were analyzed by variable angle spectroscopic ellipsometry (VASE). The reduced graphene oxide/PVA composite was assumed homogeneous with a thickness of 1364 nm. An effective medium approximation (EMA) was adopted to describe the composite, with reduced graphene oxide in a concentration factor of 5.6%.

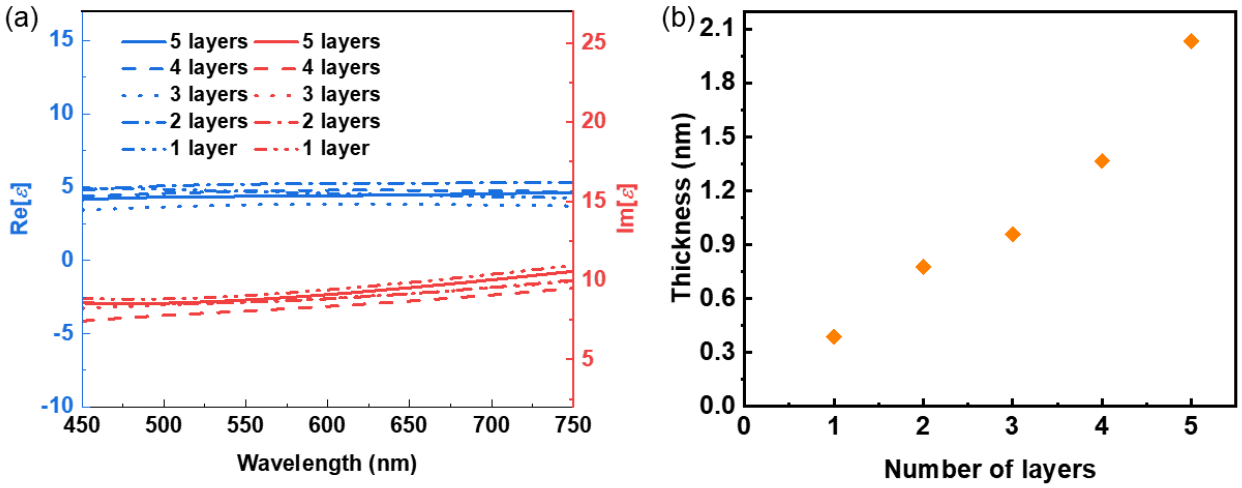

Figure 5-5 (a) R[ε], and Im[ε] parts in complex linear ε for CVD graphene thin film from 1 layer to 5 layers, wavelength range: 450 - 750 nm. (b) Nominal thickness of CVD graphene thin film from 1 layer to 5 layers, evaluated from spectroscopy ellipsometry.

As for CVD graphene, ε patterns from a single layer to five layers were plotted in Figure 5-5(a). Note that there is no difference of ε in CVD graphene from a single layer to five layers. The nominal thickness evaluated from SE for 1 layer to 5 layers were presented as Figure 5-5(b). It was demonstrated that signals of CVD graphene less than four layers in pump and probe measurement were too weak to analyze, so we take five layers of CVD graphene as the investigate target, with a thickness of 2.0 nm.

The extinction spectra can be examined by the expression of -ln(T/T$_0$). In the expression, T represents transmittance of substrate and with CVD graphene or reduced graphene oxide/PVA together, while T$_0$ represents transmittance of the substrates without samples. Figure 5-6(a) along with (b) present experimental and SE fitted extinction pattern for CVD graphene films and reduced graphene oxide/PVA films in respective. The curves exhibit similar, monotonic, and increasing extinction towards shorter wavelengths. Figure 5-6(c) and (d) show linear ε for CVD graphene as well as reduced graphene oxide, respectively. The blue line represents the real part of ε, while the red line is the imaginary part. Reduced graphene oxide exhibits the same dispersion characteristic of ε with CVD graphene. Note that compared to CVD graphene, the intensities of Re[ε] and Im[ε] of reduced graphene oxide is slightly lower. The explanation can be described that existence of oxygen containing group leads in lower carrier concentration and mobility. Agreement of the measured ellipsometric results of reduced graphene oxide, together with CVD graphene with literature, demonstrated linear optical properties of reduced graphene oxide show comparable characteristics to CVD graphene [38].

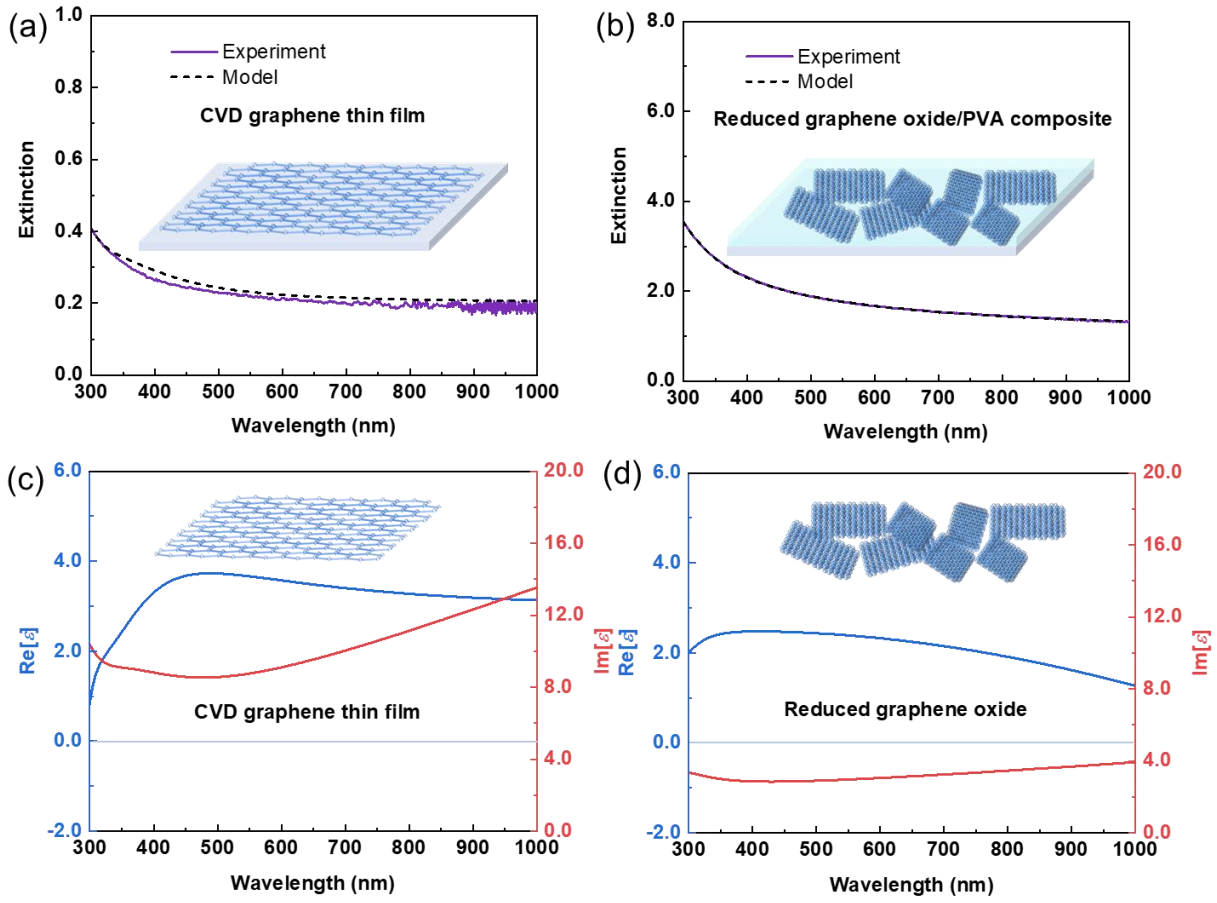

Figure 5-6 Experimental, fitted extinction spectra of (a) CVD graphene, (b) rGO/PVA. Linear dielectric function of (c) CVD graphene, and (d) rGO. Insets show the corresponding schematic.

Linear refractive index, extinction coefficient for CVD graphene, rGO were presented as Figure 5-7(a) as well as (b), in respective. Considering above results, the evaluated ε is reasonable to be employed to calculate the nonlinear complex quantities $\chi^{(3)}$.

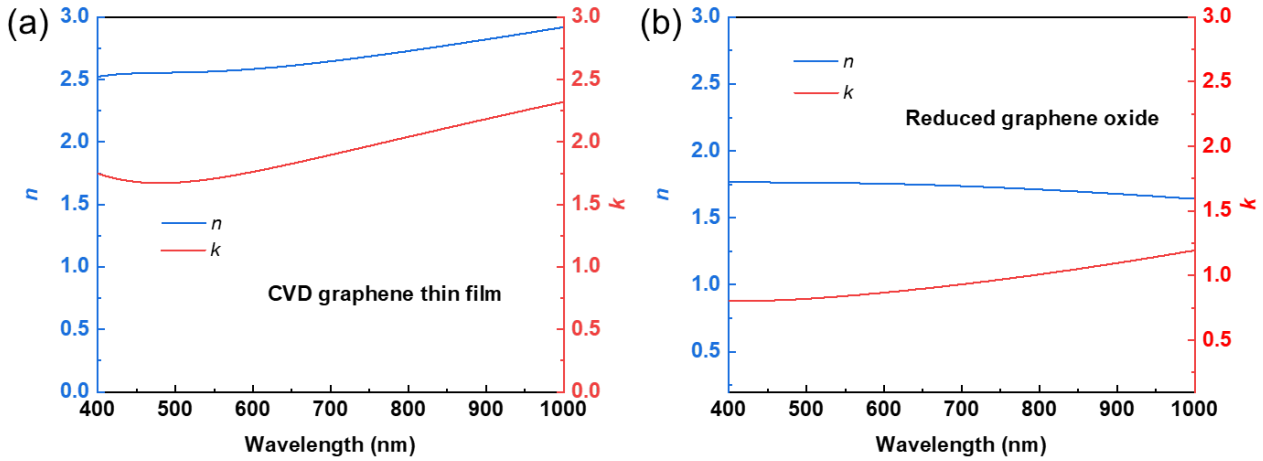

Figure 5-7 (a) Complex refractive index n along with extinction coefficient k for CVD graphene obtained from Lorentz model fitting. (b) Complex n and k of reduced graphene oxide obtained from Lorentz model fitting.

5.3.3 NLO Properties of Reduced Graphene Oxide and CVD Graphene

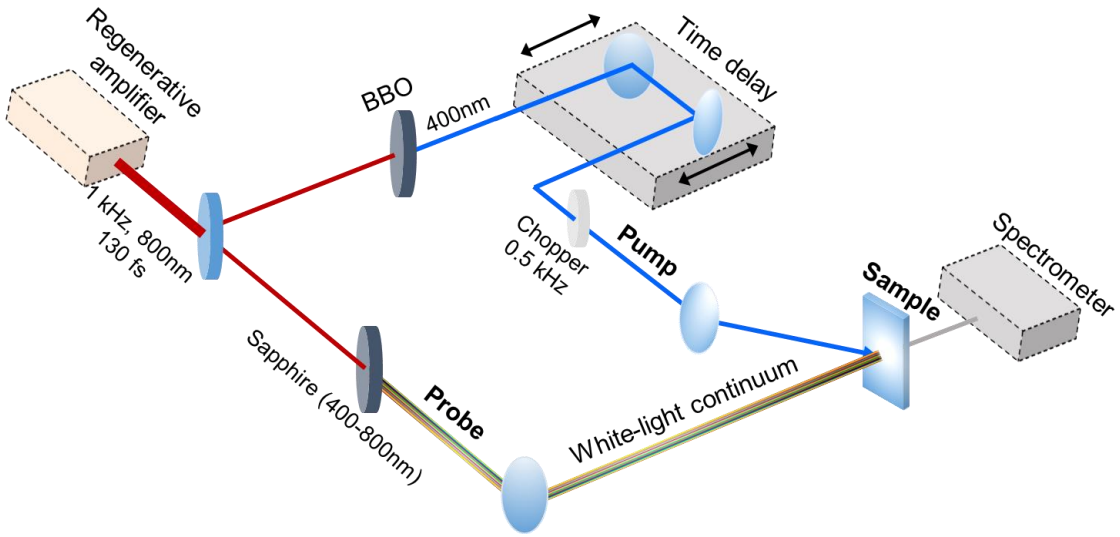

Figure 5-8 Schematic of pump-probe spectroscopy measurement.

Then NLO properties for CVD graphene and reduced graphene oxide were investigated utilizing pump-

probe spectroscopies. Measuring processes in pump and probe spectroscopies were illustrated as above schematic in Figure 5-8. ΔT/T represents the transient transmission changes of incident light in excited state and ground state [27, 39].

To evaluate third-order optical nonlinearities which has proportional relations with power intensity, measurement should be conducted in the linear region of the pump peak intensity. In addition, the pump peak intensity should be maintained in the linear region to protect the samples from damages by the laser beam. The pump power dependence of transient transmission changes in the pump-probe measurement was investigated firstly. Figure 5-9 shows the ΔT/T of reduced graphene oxide/PVA composite thin film coated on the silica substrate as a function of excitation intensity. As can be seen in the ΔT/T at 690 nm, the optical nonlinearity has proportional relations with excitation intensities with low excitation power until the intensity increases up to 2.11 GW/cm^2. At higher excitation intensity after 2.11 GW/cm^2, the ΔT/T then saturates. Thus, the pump peak power density used in this work was 1.70 GW/cm^2 with a focal size of 168.2 μm.

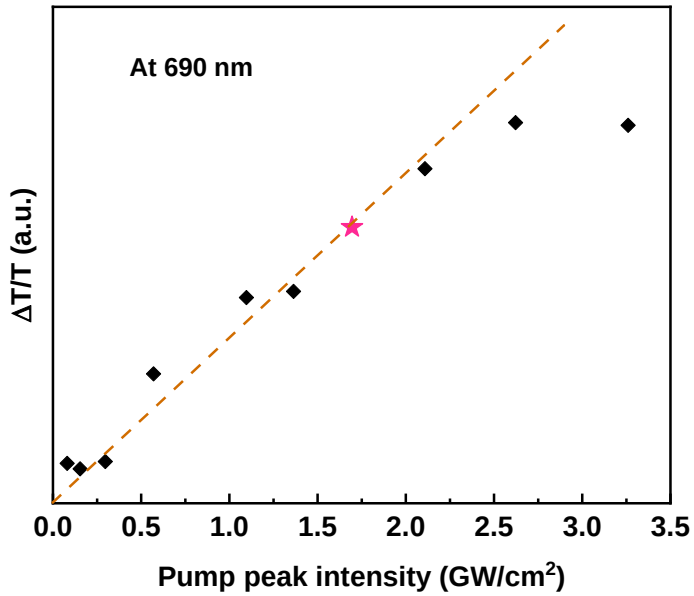

Figure 5-9 The pump power dependence of transient transmission changes in the pump and probe measurement. The pump peak power density used in this work was 1.70 GW/cm^2 with a focal size of 168.2 μm.

In addition, a strong chip effect occurred in the probe white-light continuum because of the group velocity dispersion induced by the utilized nonlinear crystals. To correct the course of experimental raw data properly, the group velocities were studied through measurement of nonlinearity in $LiNbO_3$. All the raw data in the

experiment was corrected by group velocity dispersion.

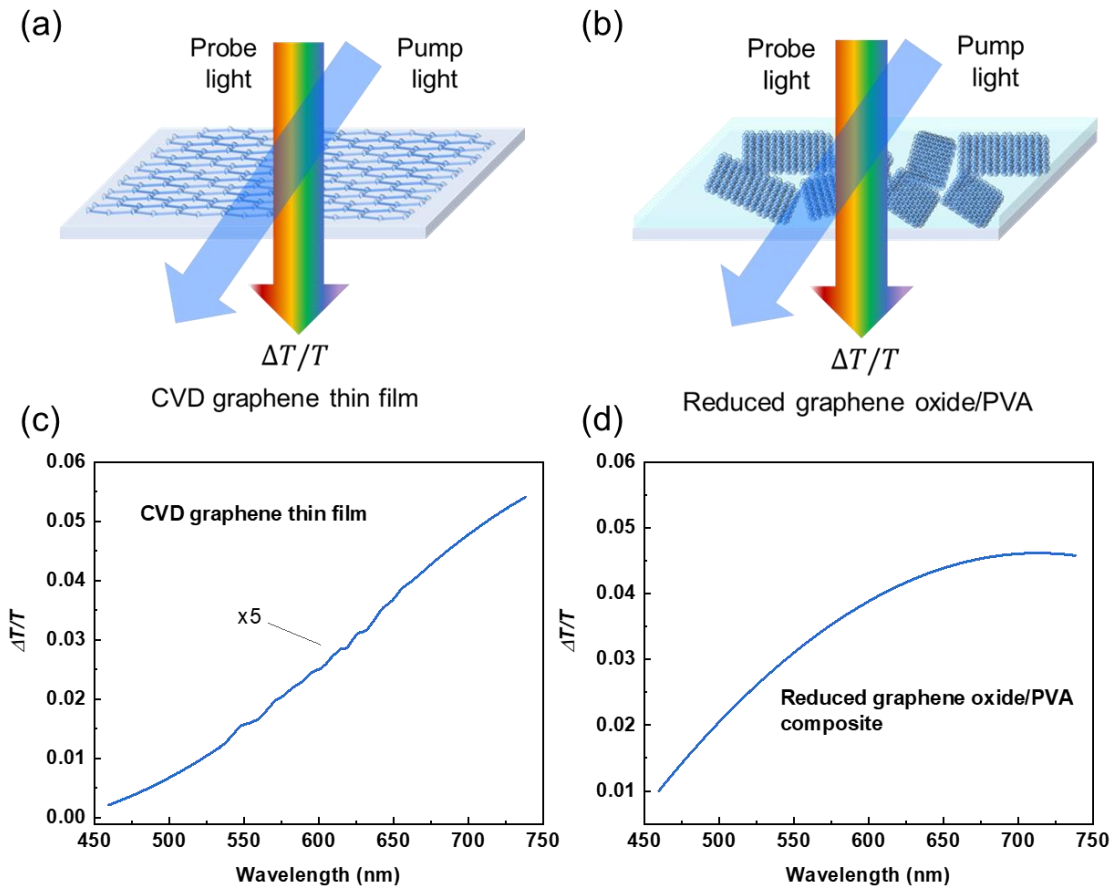

Figure 5-10 Schematics for the pump-probe measuring in (a) CVD graphene, and (b) reduced graphene oxide/PVA on silica substrates, respectively. ΔT/T patterns for (c) CVD graphene, and (d) reduced graphene oxide/PVA.

For CVD graphene thin film and reduced graphene oxide/PVA composite, they were measured by pump and probe spectroscopy seen as Figure 5-10(a), (b), along with samples and laser beams. The corresponding ΔT/T curves were calculated and plotted as Figure 5-10(c) along with 5-10(d), respectively. Our measurement techniques allow us to study the spectral information on a wide wavelength range instead of discrete points. Positive ΔT/T values represented saturable absorption (SA) [40] and were observed throughout the visible spectrum from 450 to 750 nm, for reduced graphene oxide/PVA films. ΔT/T results measured in blank PVA were reported by Sato et al. [41], there is no contribution from PVA on the nonlinearity. This strong SA provides possibilities for reduced graphene oxide to be applied in many nanophotonic fields. The same characteristic ΔT/T pattern can be observed in the CVD graphene. These photoinduced features are mainly due to the linear wavelength-dependent energy dispersion near the Dirac point of CVD graphene and reduced graphene oxide

shown in Figure 5-11.

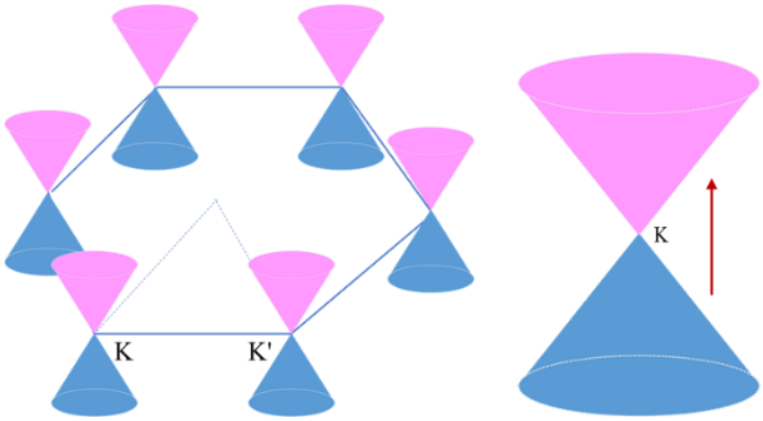

Figure 5-11 Schematic electronic band structure near the Dirac points in graphene.

Next, $\chi^{(3)}$of CVD graphene and reduced graphene oxide were evaluated by combining ellipsometric results and ΔT/T as reported [42]. Linear ε and ground state transmission T were generated in the afore-mention. The nonlinear ε+Δε in the excited state was extracted by fitting T+ΔT with the ellipsometric model. The patterns of T+ΔT and T were shown in Figure 5-12, for CVD graphene thin film and reduced graphene oxide.

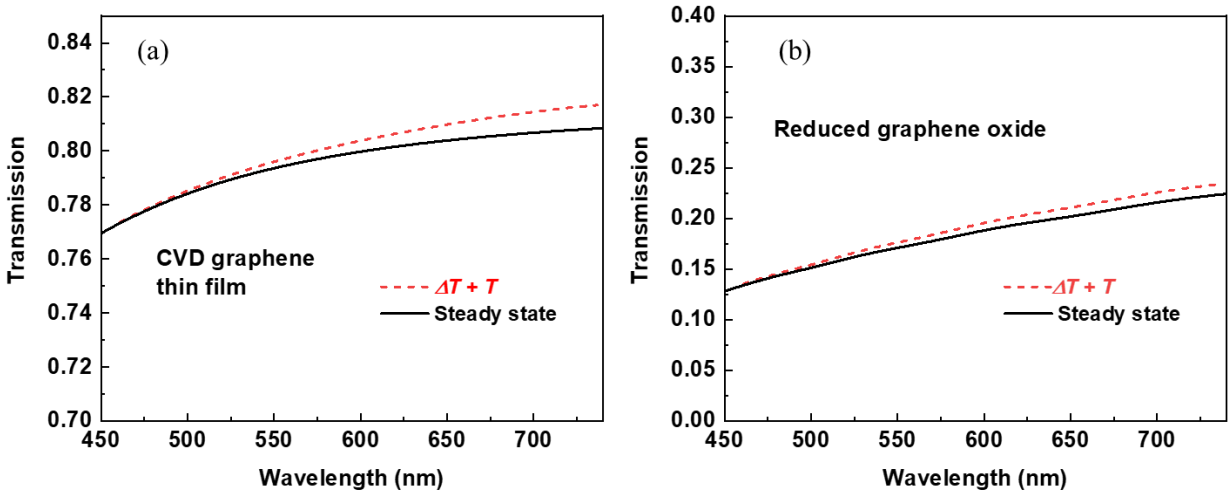

Figure 5-12 $\Delta T + T$ and steady-state T for (a) CVD graphene thin film, as well as (b) Reduced graphene oxide/PVA composite.

In the fitting process, same ellipsometric models were utilized like in linear analysis. We regarded these parameters of the oscillator as the only variable values. The parameters of corresponding oscillators in the excited state varied from the ground state, as shown in Table 5-3 and 5-4.

Table 5-3 Information of oscillator for CVD graphene thin film in excited-state.

Nonlinear	Oscillator	En (eV)	Amp	Br (eV)
MSE=0.274	Lorentz1	0.222	65.725	9.025
	Lorentz2	3.718	4.289	2.548
	Lorentz3	4.384	4.931	0.838

Table 5-4 Information of oscillator for reduced graphene oxide in excited-state.

Nonlinear	Oscillator	En (eV)	Amp	Br (eV)
MSE=0.126	Lorentz1	0.211	15.517	28.993
	Lorentz2	4.786	1.749	2.329
	Lorentz3	5.207	0.824	10.854

The $\chi^{(3)}$ values of CVD graphene and reduced graphene oxide can be calculated from the nonlinear dielectric function change Δε through a simple derivation of the equation (5-1):

$$\Delta\varepsilon\left(\omega_{probe}\right) = \frac{3}{4}\,\chi^{(3)}\left(\omega_{probe}\right)I \qquad (5\text{-}1)$$

3/4 represents refractive index that dependent on intensities in the equation, and *I* represent pump lasers intensities, respectively [43].

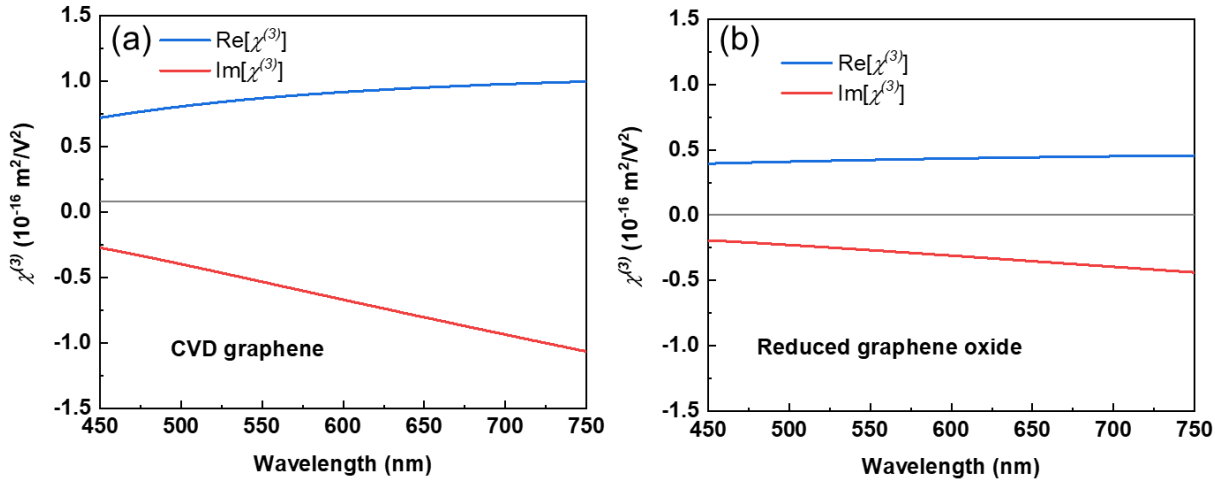

Figure 5-13 The $\chi^{(3)}$ patterns for (a) CVD graphene thin film, and (b) reduced graphene oxide nanosheets evaluated in 450 – 750 nm.

$\chi^{(3)}$ spectrum for reduced graphene oxide is shown as Figure 5-13(b). It is instructive to compare this

nonlinearity with that of single-layer graphene reported by Wu et al. (0.14 × 10-16 m^2/V^2 at 532 nm) [44]. The $\chi^{(3)}$ values of reduced graphene oxide are 0.42 × 10-16 m^2/V^2 at the same wavelength. Besides, graphene shows larger $\chi^{(3)}$ values compared to conventional dielectric materials (on the order of 10^{-18} - 10^{-20}) [45], as presented in Table 5-5. Furthermore, both real (blue pattern) and imaginary (red pattern) parts of $\chi^{(3)}$ show broadband, monotonic, and wavelength-dependent dispersion. These results and corresponding understanding would not be obtained through measuring at discrete wavelengths. The $Im[\chi^{(3)}]$ exhibits values with -0.18 × 10^{-16} in wavelength of 450 nm, while with -0.44 × 10^{-16} m^2/V^2 in wavelength of 750 nm. Meanwhile, the $Re[\chi^{(3)}]$ has values 0.38 × 10^{-16} in the wavelength of 450 and 0.47 × 10^{-16} m^2/V^2 in the wavelength of 750 nm. The $Im[\chi^{(3)}]$ component is negative which represents the strong SA in ΔT/T. At the same time, a comparison of nonlinearity was made between reduced graphene oxide and CVD graphene. Figure 5-13(a) reflects the $\chi^{(3)}$ spectral feature of CVD graphene. It was demonstrated that reduced graphene oxide exhibits comparable $\chi^{(3)}$ characteristics and nonlinearity. Where the values and dispersion of $\chi^{(3)}$ are crucial to nanophotonic applications. Thus, reduced graphene oxide can benefit from practical applications because of its simple and low-cost fabrication process.

Table 5-5 The third-order optical susceptibilities in various samples.

Sample	λ (nm)	$\chi^{(3)}$ (m^2/V^2)	Ref.
Single layer graphene	532	0.14 × 10^{-16} ($Re[\chi^{(3)}]$)	[44]
Conventional dielectric materials	532, 700	~10^{-18} - 10^{-20} (Absolute value)	[45]
Reduced graphene oxide	450 - 750	(0.38 - 0.47) × 10^{-16} ($Re[\chi^{(3)}]$) (-0.18 - -0.44) × 10^{-16} ($Im[\chi^{(3)}]$)	This work

To identify the condition of electronic transitions at nonlinear state in CVD graphene thin film and reduced graphene oxide, the contribution of different Lorentz terms in our model were separated and plotted in Figure 5-14. The π conjugation electrons were represented by one Lorentz oscillator and reflect the electronic transitions from the π bond, which is marked in the dashed line. While the σ bond electrons were represented by two Lorentz oscillators and plotted in the dotted line. As observed in Figure 5-14, the pattern of π conjugation electrons in CVD graphene and reduced graphene oxide exhibit similar broadband and monotonic dispersion with $Re[\chi^{(3)}]$ and $Im[\chi^{(3)}]$ towards higher wavelength. We demonstrated that the π conjugation electronic transitions contribute dominantly to the nonlinearities of rGO at excited state, as well as CVD graphene. The π band is perpendicular to the carbon planar structure in graphene. Its formation is mainly due

to covalent interaction between unaffected p orbital with neighboring carbon atoms. The π band is half-filled because p possesses one free electron [46]. While σ has a filled condition and form a deep valence band due to the Pauli principle. So, the incident laser beams lead to π conjugation electronic transitions and contribute to the wavelength-dependent nonlinearities from 450 to 750 nm.

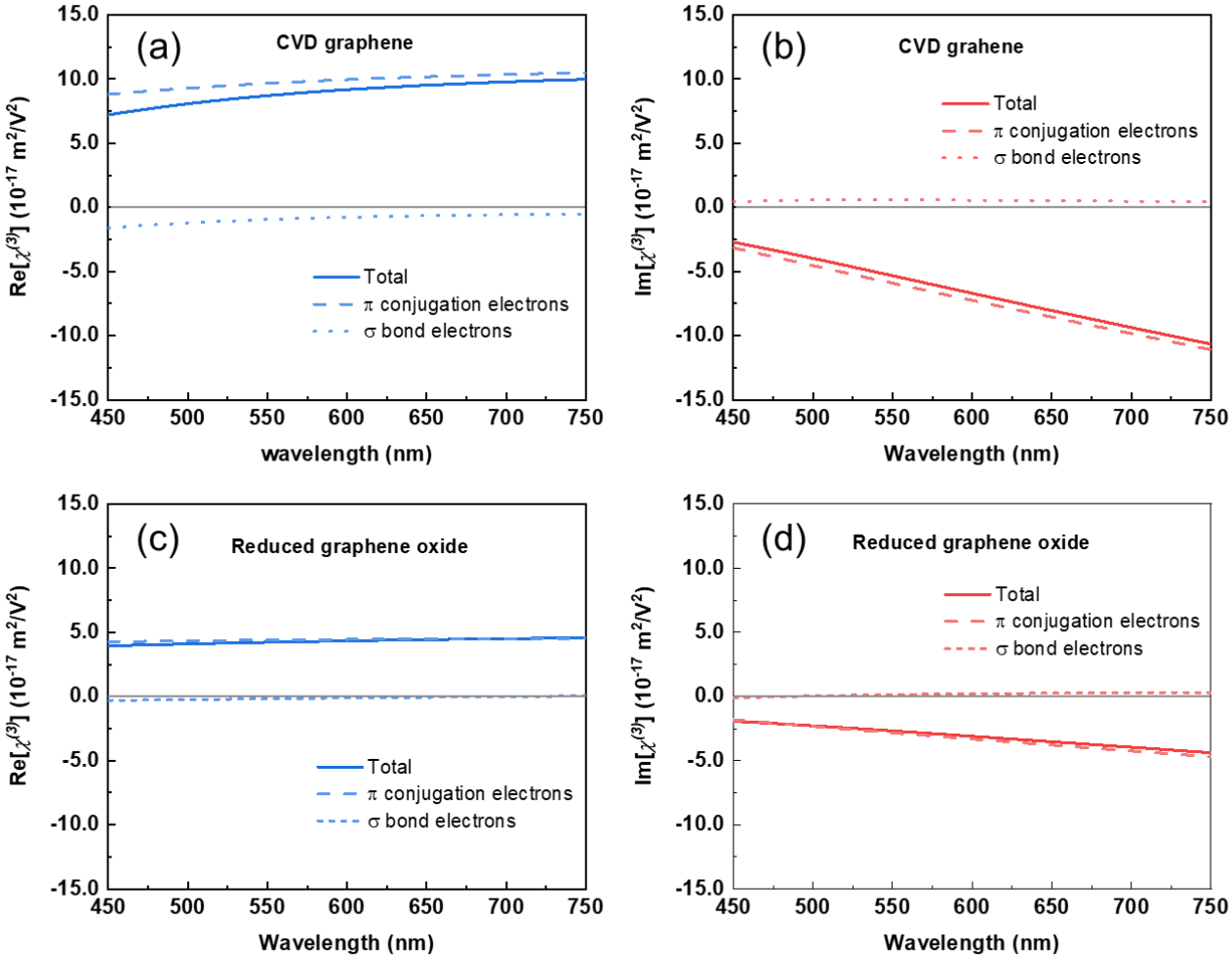

Figure 5-14 Real (a), imaginary (b) parts for $\chi^{(3)}$ in CVD graphene. Real (c), imaginary (d) parts of $\chi^{(3)}$ for reduced graphene oxide. The contribution of π conjugation electrons and σ bond electrons denoted by the dashed line and dotted line, respectively. The solid line represents a total third-order susceptibility.

5.4 Conclusions

In summary, a two-dimensional thin film with reduced graphene oxide dispersed homogeneously in the PVA matrix was prepared in this work. Compared to CVD graphene thin film, the process is simple, low cost, and reproducibility in practical applications. We have conducted comparative experiments and investigated the

NLO properties for reduced graphene oxide as well as CVD graphene over visible spectrum from 450 to 750 nm. The combination of SE and femtosecond pump and probe spectroscopy provide us insight investigation for exploring the dispersion of $\chi^{(3)}$ in continuous wavelength rather than discrete plots. Results show that $\Delta T/T$ and $\chi^{(3)}$ of reduced graphene oxide possesses broadband and monotonic characteristics at different wavelengths. Through above investigations, identification can be achieved successfully that the π conjugation electronic transitions that contribute dominantly to the nonlinearities of reduced graphene oxide, along with CVD graphene. Furthermore, reduced graphene oxide exhibits broader, larger nonlinearities compared to conventional dielectric materials, and a comparable nonlinear response with CVD graphene. Considering the lost-cost and high-throughput fabrication, reduced graphene oxide presents opportunities as an alternative material to be applied for the concentration and modulation of light in nanophotonic.

References

[1] M.T. Hill, M.C. Gather, Advances in small lasers, Nat Photonics, 8 (2014) 908-918.

[2] Y.R. Fang, M.T. Sun, Nanoplasmonic waveguides: towards applications in integrated nanophotonic circuits, Light-Sci Appl, 4 (2015) e294-e294.

[3] C. Koos, P. Vorreau, T. Vallaitis, P. Dumon, W. Bogaerts, R. Baets, B. Esembeson, I. Biaggio, T. Michinobu, F. Diederich, W. Freude, J. Leuthold, All-optical high-speed signal processing with silicon–organic hybrid slot waveguides, Nat Photonics, 3 (2009) 216-219.

[4] L.W. Luo, N. Ophir, C.P. Chen, L.H. Gabrielli, C.B. Poitras, K. Bergmen, M. Lipson, WDM-compatible mode-division multiplexing on a silicon chip, Nat Commun, 5 (2014) 3069.

[5] H. Ren, X. Li, Q. Zhang, M. Gu, On-chip noninterference angular momentum multiplexing of broadband light, Science, 352 (2016) 805-809.

[6] N.J. Halas, S. Lal, W.S. Chang, S. Link, P. Nordlander, Plasmons in strongly coupled metallic nanostructures, Chem Rev, 111 (2011) 3913-3961.

[7] J.A. Schuller, E.S. Barnard, W. Cai, Y.C. Jun, J.S. White, M.L. Brongersma, Plasmonics for extreme light concentration and manipulation, Nat Mater, 9 (2010) 193-204.

[8] Q. Bao, K.P. Loh, Graphene photonics, plasmonics, and broadband optoelectronic devices, ACS Nano, 6 (2012) 3677-3694.

[9] J.L. Cheng, N. Vermeulen, J.E. Sipe, Third order optical nonlinearity of graphene, New J Phys, 16 (2014) 053014.

[10] F.J. Garcia de Abajo, Graphene nanophotonics, Science, 339 (2013) 917-918.

[11] A. Vakil, N. Engheta, Transformation Optics Using Graphene, Science, 332 (2011) 1291-1294.

[12] Q.S. Guo, C. Li, B.C. Deng, S.F. Yuan, F. Guinea, F.N. Xia, Infrared Nanophotonics Based on Graphene Plasmonics, Acs Photonics, 4 (2017) 2989-2999.

[13] L. Yu, J. Zheng, Y. Xu, D. Dai, S.J.A.n. He, Local and nonlocal optically induced transparency effects in graphene–silicon hybrid nanophotonic integrated circuits, 8 (2014) 11386-11393.

[14] D.A. Brownson, C.E. Banks, The electrochemistry of CVD graphene: progress and prospects, Phys Chem Chem Phys, 14 (2012) 8264-8281.

[15] S. Bae, H. Kim, Y. Lee, X. Xu, J.S. Park, Y. Zheng, J. Balakrishnan, T. Lei, H.R. Kim, Y.I. Song, Y.J. Kim, K.S. Kim, B. Ozyilmaz, J.H. Ahn, B.H. Hong, S. Iijima, Roll-to-roll production of 30-inch graphene films for transparent electrodes, Nat Nanotechnol, 5 (2010) 574-578.

[16] A. Nekahi, P.H. Marashi, D. Haghshenas, Transparent conductive thin film of ultra large reduced graphene oxide monolayers, Appl Surf Sci, 295 (2014) 59-65.
[17] D. Lee, H. Lee, Y. Ahn, Y. Jeong, D.Y. Lee, Y. Lee, Highly stable and flexible silver nanowire-graphene hybrid transparent conducting electrodes for emerging optoelectronic devices, Nanoscale, 5 (2013) 7750-7755.
[18] D.H. Youn, Y.J. Yu, H. Choi, S.H. Kim, S.Y. Choi, C.G. Choi, Graphene transparent electrode for enhanced optical power and thermal stability in GaN light-emitting diodes, Nanotechnology, 24 (2013) 075202.
[19] X.D. Liu, S.L. Guo, H.T. Wang, L.T. Hou, Theoretical study on the closed-aperture Z-scan curves in the materials with nonlinear refraction and strong nonlinear absorption, Optics Communications, 197 (2001) 431-437.
[20] M. Yin, H.P. Li, S.H. Tang, W. Ji, Determination of nonlinear absorption and refraction by single Z-scan method, Appl Phys B-Lasers O, 70 (2000) 587-591.
[21] S. Bhattacharya, A. Ghorai, S. Raval, M. Karmakar, A. Midya, S.K. Ray, P.K. Datta, A comprehensive dual beam approach for broadband control of ultrafast optical nonlinearity in reduced graphene oxide, Carbon, 134 (2018) 80-91.
[22] L.L. Miao, Y.Q. Jiang, S.B. Lu, B.X. Shi, C.J. Zhao, H. Zhang, S.C. Wen, Broadband ultrafast nonlinear optical response of few-layers graphene: toward the mid-infrared regime, Photonics Res, 3 (2015) 214-219.
[23] G. Muruganandi, M. Saravanan, G. Vinitha, M.B.J. Raj, T.C.S. Girisun, Effect of reducing agents in tuning the third-order optical nonlinearity and optical limiting behavior of reduced graphene oxide, Chem Phys, 488 (2017) 55-61.
[24] K. Sabira, P. Saheeda, M.C. Divyasree, S. Jayalekshmi, Impressive nonlinear optical response exhibited by Poly(vinylidene fluoride) (PVDF)/reduced graphene oxide (RGO) nanocomposite films, Opt Laser Technol, 97 (2017) 77-83.
[25] X. Zhao, X.Q. Yan, Q. Ma, J. Yao, X.L. Zhang, Z.B. Liu, J.G. Tian, Nonlinear optical and optical limiting properties of graphene hybrids covalently functionalized by phthalocyanine, Chem Phys Lett, 577 (2013) 62-67.
[26] Z. Liu, N. Dong, P. Jiang, K. Wang, J. Wang, Y. Chen, Reduced Graphene Oxide Chemically Modified with Aggregation-Induced Emission Polymer for Solid-State Optical Limiter, Chemistry, 24 (2018) 19317-19322.
[27] R. Sato, M. Ohnuma, K. Oyoshi, Y. Takeda, Experimental investigation of nonlinear optical properties of Ag nanoparticles: Effects of size quantization, Physical Review B, 90 (2014) 125417.
[28] H. Chang, H. Wu, Graphene-Based Nanomaterials: Synthesis, Properties, and Optical and Optoelectronic

Applications, Advanced Functional Materials, 23 (2013) 1984-1997.

[29] S.N. Alam, N. Sharma, L. Kumar, Synthesis of Graphene Oxide (GO) by Modified Hummers Method and Its Thermal Reduction to Obtain Reduced Graphene Oxide (rGO), Graphene, 06 (2017) 1-18.

[30] W.J. Tan, H. Liu, J.H. Si, X. Hou, Control of the gated spectra with narrow bandwidth from a supercontinuum using ultrafast optical Kerr gate of bismuth glass, Applied Physics Letters, 93 (2008) 051109.

[31] W.M. Itano, J.J. Bollinger, J.N. Tan, B. Jelenkovic, X. Huang, D.J. Wineland, Bragg diffraction from crystallized ion plasmas, Science, 279 (1998) 686-689.

[32] J.J. Li, L.S. Shao, L.H. Yuan, Y.H. Wang, A novel strategy for making poly(vinyl alcohol)/reduced graphite oxide nanocomposites by solvothermal reduction, Mater Design, 54 (2014) 520-525.

[33] R. Sato, J. Henzie, H. Rong, M. Naito, Y. Takeda, Enhancement of the complex third-order nonlinear optical susceptibility in Au nanorods, Opt Express, 27 (2019) 19168-19176.

[34] Y. Shen, P. Zhou, Q.Q. Sun, L. Wan, J. Li, L.Y. Chen, D.W. Zhang, X.B. Wang, Optical investigation of reduced graphene oxide by spectroscopic ellipsometry and the band-gap tuning, Applied Physics Letters, 99 (2011).

[35] G.G. Politano, C. Versace, C. Vena, M. Castriota, F. Ciuchi, A. Fasanella, G. Desiderio, E. Cazzanelli, Physical investigation of electrophoretically deposited graphene oxide and reduced graphene oxide thin films, J Appl Phys, 120 (2016) 195307.

[36] Y. Shen, S.B. Yang, P. Zhou, Q.Q. Sun, P.F. Wang, L. Wan, J. Li, L.Y. Chen, X.B. Wang, S.J. Ding, D.W. Zhang, Evolution of the band-gap and optical properties of graphene oxide with controllable reduction level, Carbon, 62 (2013) 157-164.

[37] Y. Yang, N. Akozbek, T.-H. Kim, J.M. Sanz, F. Moreno, M. Losurdo, A.S. Brown, H.O. Everitt, Ultraviolet–Visible Plasmonic Properties of Gallium Nanoparticles Investigated by Variable-Angle Spectroscopic and Mueller Matrix Ellipsometry, ACS Photonics, 1 (2014) 582-589.

[38] S. Schoche, N. Hong, M. Khorasaninejad, A. Ambrosio, E. Orabona, P. Maddalena, F. Capasso, Optical properties of graphene oxide and reduced graphene oxide determined by spectroscopic ellipsometry, Appl Surf Sci, 421 (2017) 778-782.

[39] R. Sato, H. Momida, M. Ohnuma, M. Sasase, T. Ohno, N. Kishimoto, Y. Takeda, Experimental dispersion of the third order optical susceptibility of Ag nanoparticles, J Opt Soc Am B, 29 (2012) 2410-2413.

[40] B.Y. Zhang, R. Sato, K. Oyoshi, H. Mamiya, M. Ohnuma, Y. Takeda, Dispersion of third-order susceptibility of Au nanoparticles fabricated by ion implantation, Nucl Instrum Meth B, 447 (2019) 38-42.

[41] R. Sato, S. Ishii, T. Nagao, M. Naito, Y. Takeda, Broadband Plasmon Resonance Enhanced Third-Order

Optical Nonlinearity in Refractory Titanium Nitride Nanostructures, ACS Photonics, 5 (2018) 3452-3458.

[42] R. Sato, M. Ohnuma, K. Oyoshi, Y. Takeda, Spectral investigation of nonlinear local field effects in Ag nanoparticles, J Appl Phys, 117 (2015) 113101.

[43] J.E. Sipe, R.W. Boyd, Nonlinear susceptibility of composite optical materials in the Maxwell Garnett model, Phys Rev A, 46 (1992) 1614-1629.

[44] R. Wu, Y. Zhang, S. Yan, F. Bian, W. Wang, X. Bai, X. Lu, J. Zhao, E. Wang, Purely coherent nonlinear optical response in solution dispersions of graphene sheets, Nano Lett, 11 (2011) 5159-5164.

[45] Y.X. Zhang, Y.H. Wang, Nonlinear optical properties of metal nanoparticles: a review, Rsc Advances, 7 (2017) 45129-45144.

[46] A.H. Castro Neto, F. Guinea, N.M.R. Peres, K.S. Novoselov, A.K. Geim, The electronic properties of graphene, Reviews of Modern Physics, 81 (2009) 109-162.

Chapter 6

Conclusions and Perspective

6.1 Conclusions

It has been proved that graphene-based materials can exhibit remarkable electrochemical properties after decorated with cobalt borate nanoparticles. The composite shows outstanding supercapacitor behavior when it serves as a negative electrode in the lithium-ion capacitor, which implies that graphene-based materials could be a prospective choice for the application of lithium-ion capacitors as an anode material. In addition, the optical nonlinearities of graphene-based materials including graphene oxide and reduced graphene oxide were investigated over visible range of 450 - 750 nm and show remarkable nonlinear optical response. The dispersion of third-order susceptibilities in the visible region reveals the substantial behavior of graphene-based materials to wavelength and pulse width of light in the nonlinear state, which propels the movement of manipulating light at the nanoscale over broad wavelength. To be specific, the details will be introduced below.

1. **Reduced Graphene Oxide Decorated with Crystallized Cobalt Borate Nanoparticles as an Anode in Lithium-Ion Capacitors.**

    1) The preparation of composite material composing of reduced graphene oxide and crystallized cobalt borate nanoparticles (Co-B/rGO) was achieved via a simple in-situ grow reaction.
    2) The Co-B/rGO composite exhibited large specific capacities, good rate capabilities, along with stable cycling performance when measured using lithium-ion battery half-cell.
    3) The lithium-ion capacitor (LIC) based on the Co-B/rGO composite as an anode material was fabricated with improved specific capacitance, high energy, and power density compared to blank rGO LIC.

4) Crystallized cobalt borate nanoparticles not only work as the spacer to alleviate the aggregation of rGO nanosheets but also function as an effective electron transfer bridge in the cross-plane direction to improve the electrical conductivity.

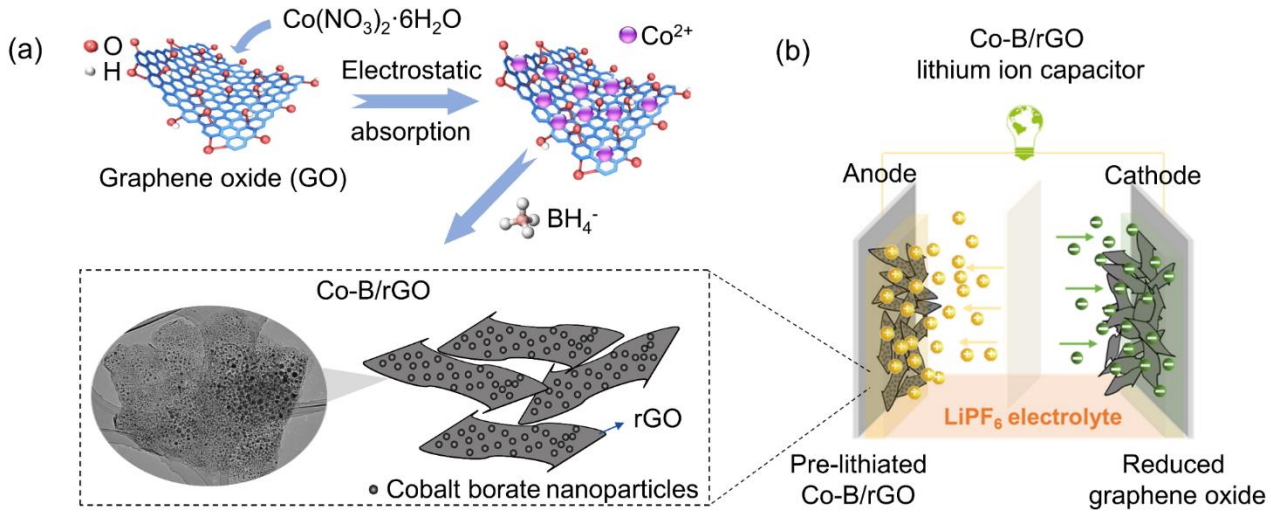

Figure 6-1 (a) Illustration on the preparation method of Co-B/rGO composites. (b) Diagram about LIC full cell based on Co-B/rGO composite anode.

2. Experimental dispersion of the third-order optical susceptibilities of graphene oxide.

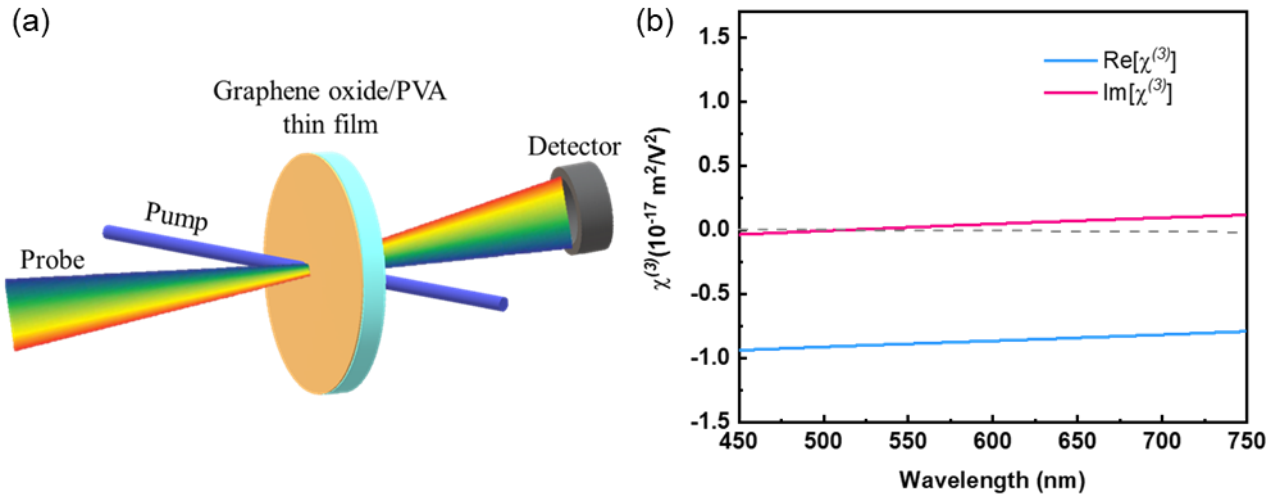

Figure 6-2 (a) Illustrating image of pump-probe measurement for graphene oxide. (b) Third-order susceptibilities $\chi^{(3)}$ of graphene oxide, including real part represented in blue line, imaginary part represented in red line (wavelength range: 450 - 750 nm).

1) The graphene oxide/PVA composite thin films with smooth surface were successfully fabricated through spin coating.
2) The combinations of femtosecond pump-probe spectroscopy and spectroscopic ellipsometry were conducted aiming at investigating optical nonlinearities for graphene oxide.
3) The dispersion of third-order optical susceptibilities $\chi^{(3)}$ of graphene oxide was experimentally determined over visible region (450 - 750 nm).
4) The nonlinearity of graphene oxide shows a wavelength-dependent characteristic with saturable absorption (SA) in region of short wavelengths and reverse saturable absorption (RSA) at long wavelengths.
5) It was figured out the physical identification of carrier dynamic in GO, which provides opportunities aiming at tailoring nonlinear optical properties, as well as optical limiting performance using graphene oxide.

3. Broadband and Comparative Third-order Nonlinearity of Reduced Graphene Oxide with CVD Graphene.

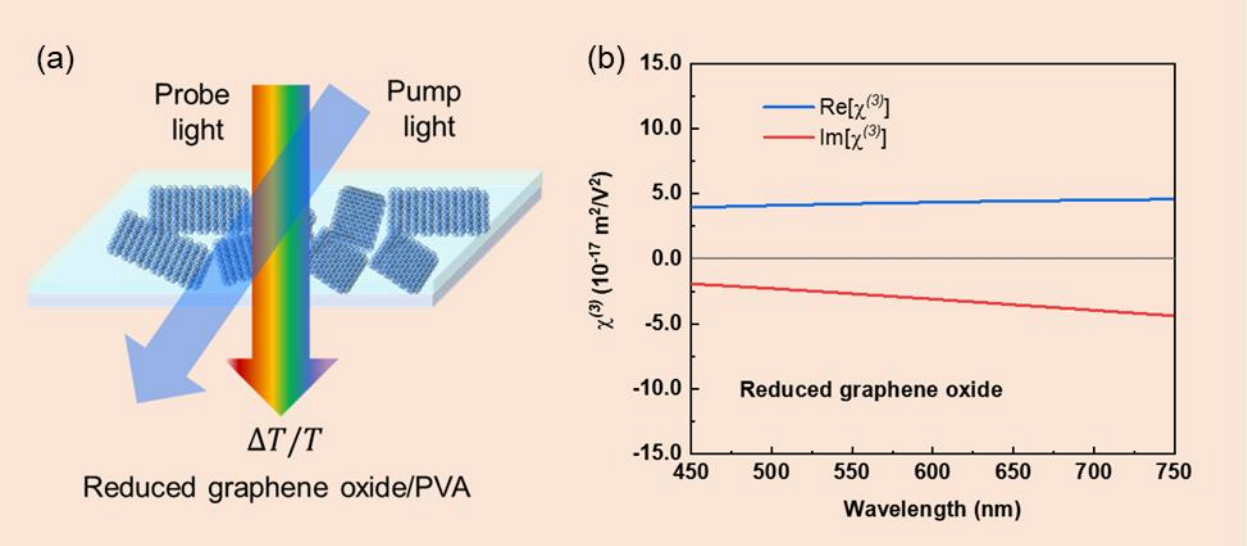

Figure 6-3 (a) Schematic of the pump and probe measurement in reduced graphene oxide/PVA on a silica substrate. (b) The third-order susceptibilities $\chi^{(3)}$ of reduced graphene oxide in the visible region (450 – 750 nm).

1) The two-dimensional thin films of reduced graphene oxide were successfully fabricated through dispersing it into the PVA matrix.

2) Third-order nonlinearity of reduced graphene oxide was experimentally determined in the visible spectrum (450 - 750 nm) through combining spectroscopic ellipsometry and femtosecond pump-probe spectroscopy.
3) It was demonstrated that reduced graphene oxide exhibits broadband and comparable third-order nonlinearity to CVD graphene.
4) It was figured out that identical tunability that π conjugation electronic transitions dominates the nonlinear response, enable reduced graphene oxide to be viable substitutes for CVD graphene.
5) Third-order susceptibility $\chi^{(3)}$ reveals their substantial behavior to wavelength and pulse width of light in a nonlinear state, which propels the movement of manipulating light at the nanoscale over broad wavelength.

6.2 Future Prospects

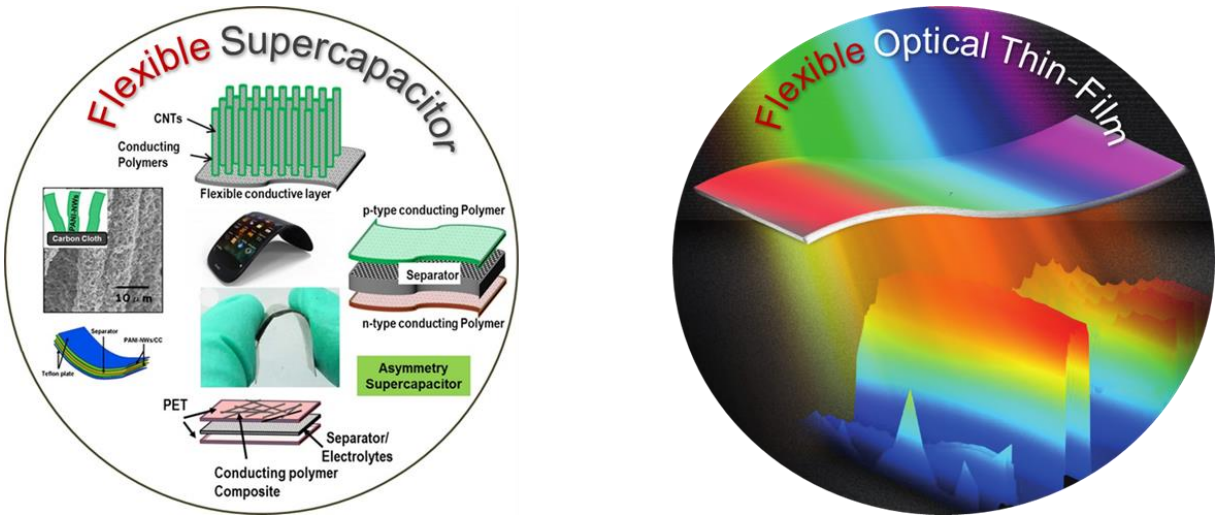

Figure 6-4 The future prospects of flexible supercapacitors and optical thin films [1].

The future generations of supercapacitors and photonic devices are expected to have good flexibility while remaining good electrochemical and nonlinear optical properties as shown in Figure 6-4. However, the electrode films of the graphene-based composite were fabricated by coating on copper foils. And the optical film was made through spin-coating on silica substrates. This is a limitation to achieve the flexibility of supercapacitors and optical devices in this thesis. Therefore, flexible films are expected to be fabricated in future work. The flexible supercapacitors of graphene-based materials probably could be achieved by using a flexible substrate. Then electrode films could be fabricated through the application of graphene-based materials onto the substrate via coating or vacuum filtration. The main problems may be stem from poor electrical

conductivity at the interface between active materials and flexible substrate, as well as the interaction between active materials with polymer electrolytes. These poor electrical conductivities could be improved through the pre-processing of the substrate and direct dipping of the electrode into polymer gel electrolyte. As for the flexible optical thin films, the demonstration was acceptable that graphene oxide and graphene coatings using flexible plastic substrate show considerable flexible properties in mechanical strength. Furthermore, they have transparent characteristics in optical applications as shown in Figure 6-5. In the future, the third-order nonlinearities of flexible thin-film need to be evaluated experimentally and compared with nonlinear optical properties before and after bending.

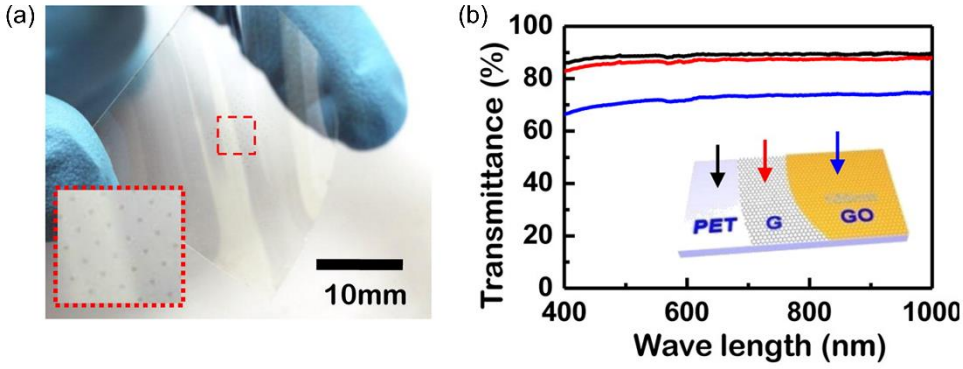

Figure 6-5 (a) Images of graphene transparent thin film fabricated by coating on flexible plastic substrates. (b) Linear transmittance patterns of PET substrates (represent in black color), graphene films coating on PET (represent in red color), and GO films coating on PET (represent in blue color), respectively. [2].

References

[1] I. Shown, A. Ganguly, L.C. Chen, K.H. Chen, Conducting polymer-based flexible supercapacitor, Energy Science & Engineering, 3 (2015) 2-26.

[2] S.-K. Lee, H.Y. Jang, S. Jang, E. Choi, B.H. Hong, J. Lee, S. Park, J.-H. Ahn, All graphene-based thin film transistors on flexible plastic substrates, Nano letters, 12 (2012) 3472-3476.

Chapter 7

Achievements

7.1 List of Publications

[1] **Luhao Kang**, Jie Tang, Shuai Tang, Kun Zhang, Yukinori Hato, Yoshihiko Takeda, Lu-Chang Qin, Reduced Graphene Oxide Decorated with Crystallized Cobalt Borate Nanoparticles as an Anode in Lithium-Ion Capacitors, *Chemical Physics Letters*, 759 (2020) 137964.

[2] **Luhao Kang**, Rodrigo Sato, Boyi Zhang, Yoshihiko Takeda, Jie Tang, Broadband and Comparative Third-order Nonlinearities in Reduced Graphene Oxide with CVD Graphene, *Optical Materials*, 110 (2020) 110463.

[3] **Luhao Kang,** Rodrigo Sato, Boyi Zhang, Yoshihiko Takeda, Jie Tang, Experimental Dispersion of the Third-order Optical Susceptibility of Graphene Oxide, *Optical Materials Express*, 10(12), (2020), 3041.

7.2 Oral Presentation

[1] **Luhao Kang**. Graphene-based Lithium-ion Capacitor and Its Application in Wide Temperature Range. The University of Tsukuba, Materials Science and Engineering, Student Seminar, December 07, 2018.

[2] **Luhao Kang**. Graphene Decorated with Crystallized Cobalt Borate Nanoparticles as an Anode in Lithium-ion Capacitors. The University of Tsukuba, Materials Science and Engineering, Student Seminar, December 03, 2019.

7.3 Conference

[1] **Luhao Kang**, Jie Tang, Youcheng Zhang, Tohru Suzuki, Qingshuo Wei, Masakazu Mukaida, Jing Li, Jinshi Yuan, Hiroaki Mamiya， Kun Zhang, Xiaoliang Yu, Yige Sun, Lu-Chang Qin. Magnetically Aligned Graphene and its Application. Tsukuba Global Science Week (TGSW). September 22, 2018, Tsukuba, Japan. (Poster)

[2] **Luhao Kang**, Jie Tang, Yukinori Hato, Kun Zhang, Xiaoliang Yu, Shuai Tang, Runsheng Gao, Tawei Chiu, Shiqi Lin, Wanli Zhang, Ozawa Kiyoshi, Taizo Sasaki, Lu-Chang Qin. High Energy Density Lithium-ion Capacitor Assembled with Graphene Cathode. Recent progress in graphene & 2D materials research. October 06-10, 2019, Matsue, Japan. (Poster)

Acknowledgments

Throughout the preparation of this doctoral thesis, I have received large amounts of support and assistance. First of all, I would like to appreciate the great help and support from my supervisor Professor Jie Tang. This dissertation was completed under the supervision of Professor Jie Tang. Professor Jie Tang allowed me to take the doctoral courses at the University of Tsukuba, which will be always a great experience in my whole life. Besides, she provided me much guidance and instructions on my research projects during the three yeas Ph.D. program. Her scientific spirit, expertise, and innovation have deeply affected me and will guide the path of my career in the future. I also appreciated her warming care on my life in Japan, especially during my hard time when I was frustrated in research. I am greatly honored to study and work in her group. Thus, I am taking this opportunity to sincerely giving my millions of thanks to her.

Likewise, I wish to express my sincerest gratitude to Professor Takeda Yoshihiko. This dissertation was accomplished also under the help and support of Professor Takeda Yoshihiko. It is my great honor to study and work in his group for about one and half years. In that period, Professor Takeda Yoshihiko gave me invaluable instructions in formulating the research questions as well as methodologies. The perceptive response from Professor Takeda Yoshihiko propelled me to sharpen my thinking and brought my work to a higher level.

I would like to give the sincere thanks to Professor Lu-Chang Qin, Dr. Rodrigo Sato, Dr. Kun Zhang, Dr. Shuai Tang for their support and help to my research. It is my great honor to learn much from them.

I also appreciate the valuable suggestion and assistance from all my colleagues: Mr. Yukinori HATO, Dr. Yige Sun, Mr. Boyi Zhang, Dr. Xiaoliang Yu, Dr. Jiaojiao Deng, Dr. Tawei Chiu, Dr. Runsheng Gao, Mrs. Shiqi Lin, Mr. Wanli Zhang. Besides, I would like to express my acknowledgment to the secretary in our group: Mrs. Hiromi Shirai.

I am highly indebted to my committee members: Professor Hase Muneaki; Professor Hashimoto Ayako; Professor Takeda Yoshihiko; Professor Jie Tang.

Finally, I would like to express my sincere thanks and love to my parents, my girlfriend, and all the friends who are always standing by me in my study abroad. My family gave me a lot of supporting and understanding in my studies, I cannot imagine the life without their love and support.

This work was performed at National Institute for Materials Science, and Graduate School of Pure and Applied Science of the University of Tsukuba.